A COMPREHENSIVE KINETICS MODEL FOR CO OXIDATION DURING CHAR COMBUSTION

Greg Haussmann and Charles Kruger

Department of Mechanical Engineering
Stanford University, Stanford, CA 94305

INTRODUCTION:

The most important parameter in representing energy feedback to a particle during char combustion concerns the oxidation of CO to CO_2. If substantial oxidation of CO occurs near a particle, then the greater heat of combustion for the complete oxidation of carbon to CO_2 (94.1 kcal/mole vs. 26.4 kcal/mole for oxidation to CO) is available for energy feedback mechanisms. "Energy feedback" is here defined as any situation in which an individual particle recieves a significant fraction of its heat of combustion directly, through the localized oxidation of emitted combustible species, i.e. CO. Conversly, if the oxidation of CO does not occur near a particle, then energy feedback will only occur indirectly, through heating of the bulk gas. The primary reaction product at the particle surface during char combustion is generally considered to be CO, and the location of the subsequent CO oxidation zone plays a very important role in determining the particle temperature. Ayling and Smith (1) performed experimental and modeling work which indicates that CO oxidation is not of major importance under the conditions they investigated, although they noted a need for improved accuracy in measuring char reactivities, as well as for better modeling of the gas phase CO oxidation kinetics. The modeling work presented in this paper attempts to develop an improved understanding of the boundary layer oxidation of CO through the use of a comprehensive set of kinetics expressions. It is hoped that the use of a fundamental set of kinetics expressions will more accurately represent the transcient conditions occuring around an oxidizing char particle, when compared to the use of global kinetics expressions. The transport and energy equations are solved, generating both species and temperature profiles surrounding a single particle.

MODEL DEVELOPMENT:

The CO oxidation model developed at Stanford currently employs a number of assumptions, which are listed in Table 1. One critical assumption used is the restriction that the only mass fluxes at the particle surface are CO and O_2. The species mass transport equation used assume convective and diffusive transport only, with source terms calculated from the kinetics expressions. The gas phase reactions are modeled through the use of a subset of a set of expressions developed by Westbrook, et al (2) to study the pyrolysis and oxidation of ethylene. This subset is listed in Table 2. The success of this model in predicting the properties of a laminar ethylene flame suggests that it is also valid for the more simple fuels contained as subsets (i.e. CO).

The basic equation for mass transport in the particle boundary layer is below.

$$\underbrace{\frac{d}{dr}\left[\frac{\rho_i}{\rho}\dot{m}''_c\,4\pi a^2\right]}_{\text{Convection}} - \underbrace{\frac{d}{dr}\left[4\pi r^2 \rho D_i \frac{d}{dr}(\rho_i/\rho)\right]}_{\text{Diffusion}} = \underbrace{4\pi r^2 \dot{\rho}_i}_{\text{Source}} \qquad 1)$$

where

ρ_i = Mass fraction of species i

ρ = Density of local gas mixture, gm/cm^3

$\dot{m}''_c$ = Carbon flux at particle surface, $gm/cm^2/sec$

a = Particle radius, cm

D_i = Diffusion coefficient for species i, cm^2/sec

$\dot{\rho}_i$ = Source term for species i (from kinetics), $gm/cm^3/sec$

Equation 1 is non-dimensionalized through the use of the parameters below.

$y = a/r$	Non-dimensional coordinate
$\chi_i = \frac{(\rho_i/\rho)}{(\rho_i/\rho)_\infty}$	Non-dimensional mass fraction
$\beta_i = (\rho_i/\rho)_\infty \rho D_i/(a\dot{m}''_c)$	Non-dimensional diffusion coefficient
$S_i = a\dot{\rho}_i/(y^4\dot{m}''_c)$	Non-dimensional source term

The resulting form for the transport equation is:

$$F_i = (\rho_i/\rho)_\infty \chi_i + \beta_i \frac{d\chi_i}{dy} \qquad 2a)$$

$$\frac{dF_i}{dy} = -S_i \qquad 2b)$$

In equation 2a, the term F_i represents a non-dimensional flux, for species i. The two equations above are solved, with the boundary conditions being:

$\chi_i(y=1) = 1$

$F_i(y=1) = 0$ except for: $F_{CO}(y=1) = 28/12$

$F_{O_2}(y=1) = -16/12$

For i = $CO, CO_2, O_2, Ar, H_2O, O, H, OH, H_2$

The mass transport equations in the boundary layer are solved along with a simple form of the energy equation, which is similar to the transport equation used.

$$K_g \frac{d}{dr} r^2 \frac{dT}{dr} - C_g \dot{m}''_c a^2 \frac{dT}{dr} = r^2 \dot{q}''' \qquad 3)$$

Conduction Convection Source

where

K_g = The average bulk thermal conductivity, erg/cm sec K

C_g = The average bulk heat capacity, erg/gm K

As with the species transport equation, this equation is transformed into non-dimensional coordinates.

$$\frac{d^2T}{dy^2} + \left[\frac{C_g \dot{m}''_c a}{K_g} \right] \frac{dT}{dy} - \left[\frac{a^2}{K_g y^4} \right] \dot{q}'''(y) = 0 \qquad 4)$$

The solution procedure utilized to solve the mass and energy transport equations is outlined in Table 3. The solution is first broken down into two components. The first part, $\chi_{i,1}(y)$ represents the solution to the homogenous portion of equations 2a and 2b, i.e. with no gas phase reactions occuring ($S_i = 0$). In this case the homogeneous solution takes a particularly simple analytical form.

$$\chi_{i,1}(y) = \frac{F_i}{(\rho_i/\rho)_\infty} + \left[1 - \frac{F_i}{(\rho_i/\rho)_\infty} \right] \exp\left[\frac{-(\rho_i/\rho)_\infty y}{D_i} \right] \qquad 5)$$

The complete solution is then represented as the sum of this homogeneous term and an inhomogeneous term, $\chi'_i(y)$. The boundary conditions on this inhomogeneous term now become particularly simple, being $\chi'_i(y=1) = 0$. One nice feature of this solution technique is that it allows the general character of the solution to be calculated immediately (the homogeneous solution) , while the more difficult inhomogeneous portion can be dealt with seperately. The inhomogeneous portion represents a very stiff equation, and a relaxation technique is applied to reach a solution. The species and energy equations are solved in series, as indicated in Table 3, and this procedure is repeated until a desired convergence criterion has been achieved.

MODEL RESULTS:

The input parameters required for this model, and the typical "base case" values used, are listed in Table 4. The values for the base case have been chosen to match conditions measured experimentally in the Stanford flow-tube reactor, in which the independent variation of many of the important reaction parameters is possible, in particular the bulk gas temperature, the oxygen concentration, and the particle size. For the current modeling results the input parameters have been independently varied around the single base case determined from the flow-tube reactor, without attempting to represent the interdependencies of the parameters. The base case value for the char reactivity at 1800K of 0.03 gm carbon/cm^2/sec agrees very well with typical values measured for char reactivities (Smith (3)), although the free stream species concentrations in the Stanford flow-tube reactor can be significantly different that those found in typical pulverized coal combustion applications. The importance of this will be discussed later.

A typical temperature profile in the particle boundary layer is presented in Figure 1. The lower curve is the solution with no gas phase reactions, while the upper curve shows the effect of CO oxidation in the boundary layer. The case chosen is one in which the greatest effect of boundary layer CO oxidation was observed, although all cases show similar profiles. In both curves the particle temperature is substantially above the bulk gas temperature (by about 500K), with this temperature overshoot increased by about 60K when gas phase CO oxidation was included. Figure 1 indicates that one way to represent the effect of CO oxidation on the particle temperature would be to look at the increase in the particle surface temperature over that with no gas phase CO oxidation. This parameter has been calculated while parametrically varying the variables listed in Table 4, and the results are discussed below.

The dependence of the bulk gas oxygen concentration is seen in Figure 2. The dependence is a reasonably strong one, although for the conditions studied the temperature increase due to CO oxidation in the boundary layer is fairly low. Thus

the energy feedback due to CO oxidation, while not negligible, is not considered to be a dominant mechanism under these conditions. It is important to note that although the base case chosen indicates little CO oxidation in the boundary layer, the trends observed will given the relative importance of the various parameters studied.

The dependence on the bulk gas water concentration is seen in Figure 3. This parameter is important due to the limiting gas phase reaction $CO + OH \rightarrow CO_2 + H$. At low concentrations there is a strong dependence of the temperature increase due to CO oxidation in the boundary layer on the bulk gas water concentration, and this dependence tails off at higher concentrations. One reason that the temperature increase is relatively low for the base case considered in the current study is that the water concentrations present in the Stanford reactor are relatively low. The only source of water in the Stanford flow-tube reactor is the moisture and hydrogen present in the coal fed into the reactor, and the relatively low particle concentrations present (< 10 particles/cm^3) results in low water concentrations. Future work will consider conditions in which the water concentrations are at higher values, since this looks like a crucial parameter in studying gas phase CO oxidation, and many pulverized coal combustion environments involve water concentrations substantially above those seen in the Stanford flow-tube reactor.

The dependence of the temperature increase on the char reactivity is seen in Figure 4. The temperature increase is a relatively strong function of the char reactivity, but eventually becomes less important. This leveling off of the curve is the result of two competing processes. As the char reactivity is increased, the amount of CO present in the particle boundary layer increases, which increases the energy release due to CO oxidation near the particle. A competing effect with this is the resulting increase of the convective term in the heat transfer equation, which tends to reduce the feedback of energy released in the boundary layer back to the particle as the char reactivity increases. The net effect of these two processes is the leveling off the the curve seen in Figure 4.

The dependence on the particle radius is seen in Figure 5. It is important to note that the char reactivity has been held constant in this parametric run, while in reality the char reactivity is a strong function of the particle radius, and this must be taken into consideration in order to better represent the true effect of the particle radius. For a fixed reactivity, however, the temperature increase due to CO oxidation is a strong function of the particle radius, a quadratic type of dependence. This is due primarily to the increased heat transfer from a smaller particle to the surroundings, which tends to lessen the effect of boundary layer CO oxidation. The actual effect of particle size is some combination of this effect with the strong increase in the particle reactivity as the radius is decreased. These two effects result in opposing trends, so the net effect of the particle radius is not clear at this point.

The dependence on the bulk gas temperature is seen in Figure 6. Again there is an interdependence between this parameter and the char reactivity, a very stong influence which is not represented in the current modeling work. As expected, the effect of CO oxidation in the boundary layer is a very strong (exponential) function of the bulk gas temperature. A temperature increase of about 60K is seen at a bulk gas temperature of 2000K. When the accompanying effect of the char reactivity dependence on the temperature is included, an even stronger dependence of the temperature increase due to CO oxidation is expected.

CONCLUSIONS:

For the conditions studied, the effect of CO oxidation in the boundary layer during char combustion does not appear to be of major importance. It is important to note that the model input parameters studied were designed to simulate conditions present in the Stanford flow-tube reactor, and that the importance of boundary layer CO oxidations in typical pulverized coal combustion environments has not yet been studied with this model.

The interdependencies between the model input parameters need to be modeled in order to better represent the actual processes occuring during CO oxidation. In particular, the parameters which indicates the possibility of a strong synergistic interaction are the water concentration, oxygen concentration, and/or the bulk gas temperature with the char reactivity.

The model results indicate the relative importance of the various parameters. The water concentration is considered to be a crucial parameter for two reasons. First, it has a strong influeuce on OH concentration in the particle boundary layer, which in turn plays a dominant role in the oxidation kinetics of CO. Secondly, many pulverized coal combustion environments are expected to have substantially higher water concentrations than that chosen for the base case condition used with this model. Other parameters which appear to be very important are the bulk gas temperature and the oxygen concentration, especially when their influence on the char reactivity is taken into account.

REFERENCES:

1. Ayling, A.B. and I.W. Smith, "Measured Temperatures of Burning Pulverized-Fuel Particles, and the Nature of the Primary Reaction Product", Combustion and Flame, V 18, 1972, pp. 173-184.

2. Westbrook, C.K., Dryer, F.L., and Schug, K.P., "A Comprehensive Mechanism for the Pyrolysis and Oxidation of Ethylene", 19th Symposium (Int'l) on Combustion, The Combustion Institute, 1982, pp. 153-166.

3. I.W. Smith, "The Combustion Rates of Coal Chars: a Review", 19th Symposium (Int'l) on Combustion, The Combustion Institute, 1982, pp. 1045-1065.

TABLE 1. ASSUMPTIONS

- Steady State.
- Diffusive and convective transport only.
- Constant particle radius.
- Spherical symmetry.
- Surface mass flux is given.
- CO and O_2 are the only surface fluxes.
- Quiescent atmosphere.
- HO_2 and H_2O_2 are unimportant at the temperatures studied.
- Convective and Conductive gas phase heat transfer only.

TABLE 2. REACTIONS CONSIDERED

1. $H + O_2 \rightleftharpoons O + OH$
2. $H_2 + O \rightleftharpoons H + OH$
3. $H_2O + O \rightleftharpoons OH + OH$
4. $H_2O + H \rightleftharpoons H_2 + OH$
5. $H_2O + M \rightleftharpoons H + OH + M$
6. $O + H + M \rightleftharpoons OH + M$
7. $O_2 + M \rightleftharpoons O + O + M$
8. $H_2 + M \rightleftharpoons H + H + M$
9. $CO + OH \rightleftharpoons CO_2 + H$
10. $CO + O + M \rightleftharpoons CO_2 + M$
11. $CO_2 + O \rightleftharpoons CO + O_2$

TABLE 3. SOLUTION PROCEDURE

SOLVE FOR A "FIRST CUT" VERSION, $\chi_{i,1}(y)$

$$\beta_i \frac{d\chi_i}{dy} + (\rho_i/\rho)_\infty = F_i \qquad 1)$$

with $F_i = 0$ except $F_{CO} = 28/12$, $F_{O2} = -16/12$

NOW WRITE THE SOLUTION AS $\chi_i = \chi_{i,1} + \chi'_i$

where χ'_i satisfies the equation .....

$$D_i \frac{d\chi'_i}{dy} + (\rho_i/\rho)_\infty = F_i(y) \qquad 2)$$

with all $\chi'_i(y=0) = 0$

Use $\chi_i(y)$ and the current temperature profile to calculate the terms $S_i(y)$ and $\dot{q}'''(y)$ from the kinetics expressions.

Integrate $S_i(y)$ to get a new $F_i(y)$

SOLVE EQUATION 2) USING THIS $F_i(y)$, 4^{th} Order Runge-Kutta Routine Used

THE SOLUTION IS THE NEW VALUE FOR $\chi'_i(y)$

SOLVE THE ENERGY EQUATION, GIVEN $\dot{q}'''(y)$ (See next page)

REPEAT UNTIL THE SYSTEM CONVERGES

TABLE 3. SOLUTION PROCEDURE (cont.)

The Energy Equation:

$$\frac{d^2T}{dy^2} + \left[\frac{C_g \dot{m}''_c a}{K_g} \right] \frac{dT}{dy} - \left[\frac{a^2}{K_g y^4} \right] \dot{q}'''(y) = 0 \qquad 3)$$

Given a particle temperature, the temperature gradient at the particle surface $\left[\frac{dT}{dy} (y=1) \right]$ is calculated from an energy balance.

$$\frac{dT}{dy} (y=1) = \frac{am''_c}{K_g} (\text{factor}) - \frac{a\varepsilon\sigma T_p}{K_g} + \frac{a\sigma}{K_g} T_w^4$$

where
factor = ergs released per gram carbon oxidized to CO
ε = emissivity of the char particle (taken as 0.9)
σ = the Stefan-Boltzman radiation constant

Given these initial conditions, Equation 3 is solved with a 4th order Runge-Kutta routine, marching from y = 1 to y = 0.

The calculated value T(y=0) is compared with the bulk gas temperature, and the procedure is repeated until convergence is obtained. (Shooting method).

TABLE 4. INPUT PARAMETERS

$\dot{m}''_c$ = .01 ,.02 ,<u>.03</u> , .04 ,.05 gm/cm^2/sec

T_g = 1600 ,1700 ,<u>1800</u> ,1900 ,2000 K

a = 10 ,20 ,30 ,<u>40</u> ,50 ,60 microns

Species Mass Fractions at infinity:

O_2 = .0040 ,<u>.0820</u> ,0.124 ,0.167 ,0.211

H_2O = 0.00046 ,<u>0.0023</u> ,0.0046 ,0.0116 ,0.0236

CO_2 = 0.0056

CO,O,H,OH,H_2 = Calculated from chemical equilibrium.

Ar = The balance.

NOTE: The underlined quantities represent the "base case", measured from experimental results with the Stanford reactor.

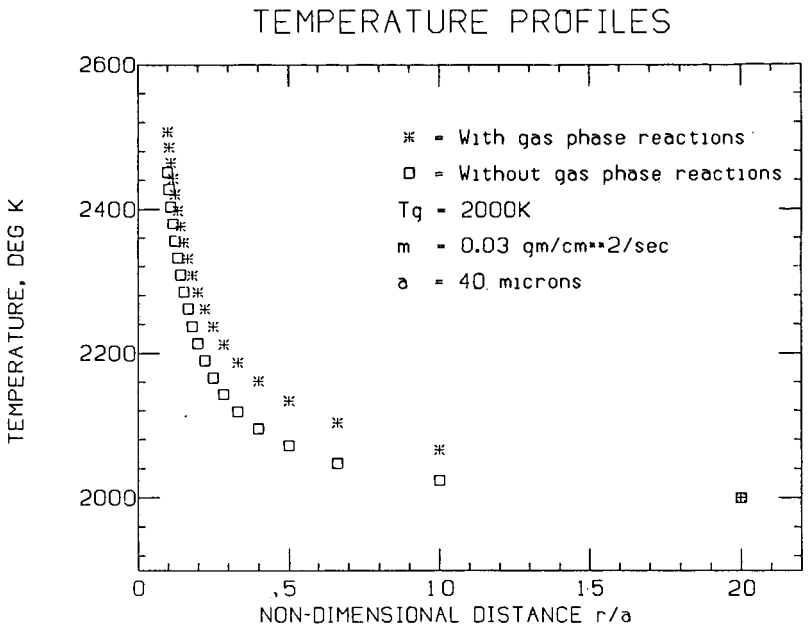

Figure 1. Temperature Profiles.

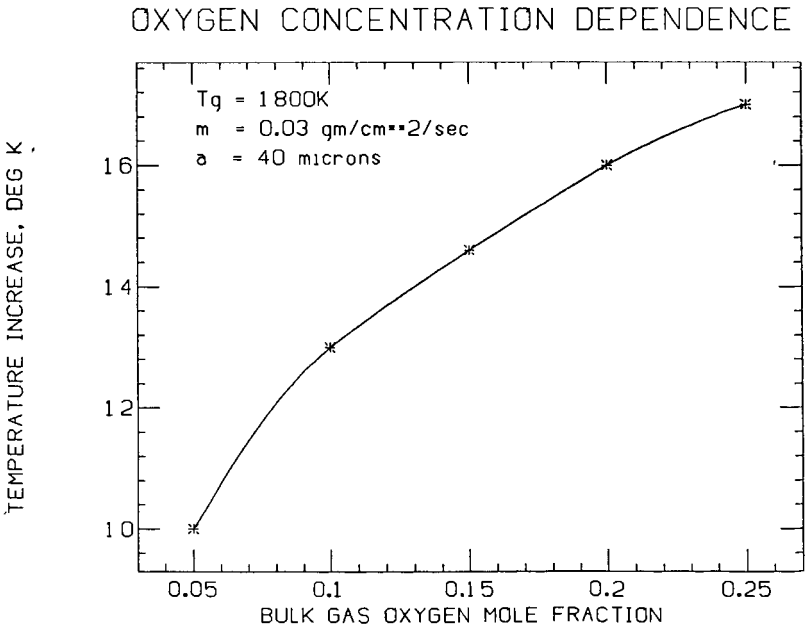

Figure 2. Oxygen Concentration Dependence.

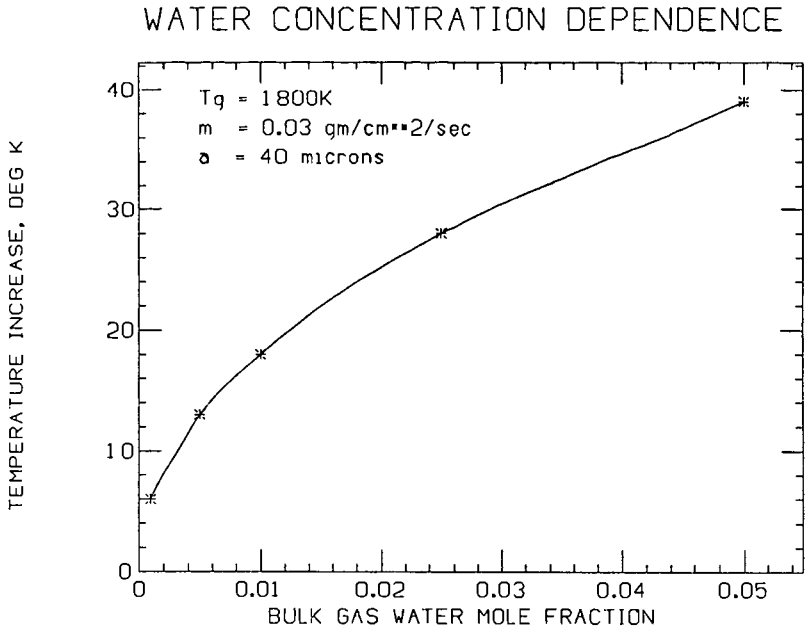

Figure 3. Water Concentration Dependence.

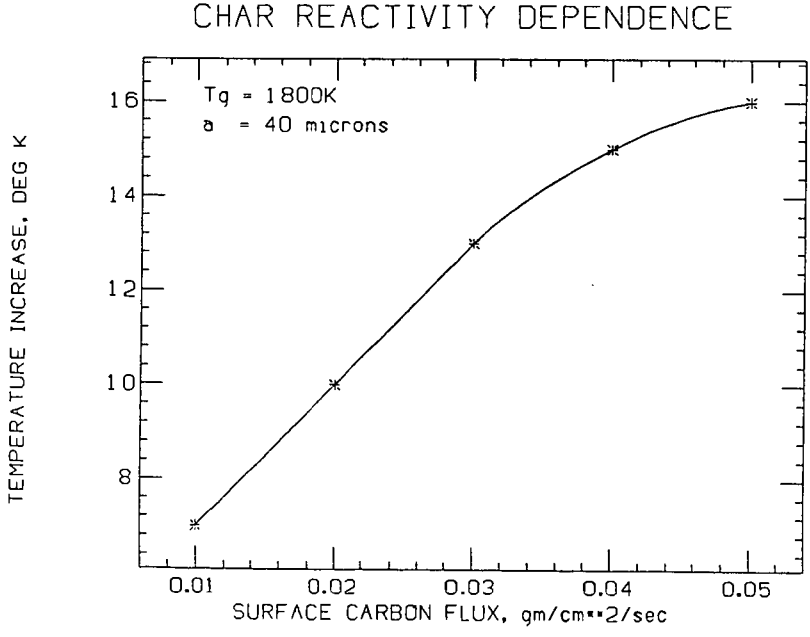

Figure 4. Char Reactivity Dependence.

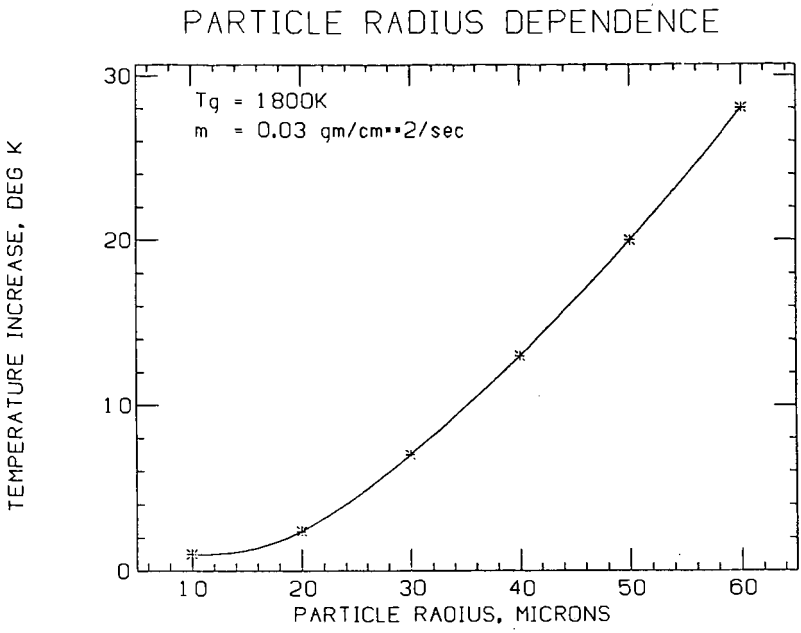

Figure 5. Particle Radius Dependence.

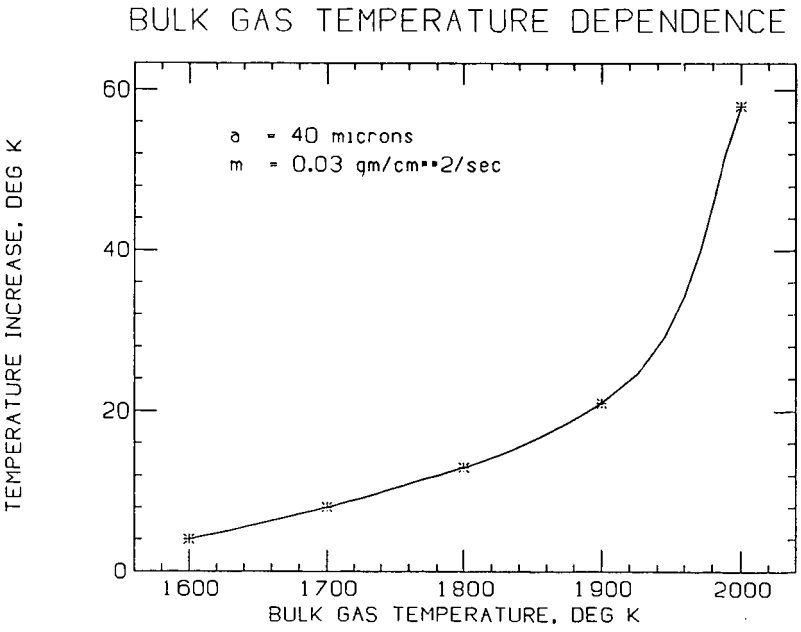

Figure 6. Bulk Gas Temperature Dependence.

DETERMINATION OF OVERALL KINETIC RATES AND OXYGEN REACTION ORDER FOR SARAN CHAR COMBUSTION

B.J. Waters, R.E. Mitchell*, R.G. Squires and N.M. Laurendeau

Purdue University, West Lafayette, IN 47907
* - Sandia National Laboratories, Livermore, CA 94550

Introduction

Recent work by Mitchell and co-workers [1,2,3] on a novel entrained flow reactor has demonstrated the feasibility of extracting kinetic rate parameters from the simultaneous measurement of the temperature, diameter and velocity of individual coal particles. These rate parameters are obtained by solving the conservation equations for a coal particle as it burns in a laminar, coflowing gas stream. In this analysis, assumptions must be made about the devolatilization processes which occur during particle heatup. Specifically, the char density, ash composition and heat gain of the particle due to homogeneous combustion of volatiles become parameters in the reactor model that depend on the parent coal.

In this work, the entrained flow reactor is used to investigate the combustion of Saran char, a very low ash, high surface area, amorphous carbon. The highly irregular Saran char particles offer a coal analog without the complicating effects associated with devolatilization and catalytic impurities. We report overall particle burning rates, apparent rate coefficients, and the apparent reaction order with respect to oxygen.

Experimental Procedure

The combustion of Saran char particles is followed in a transparent, rectangular, entrained flow reactor which is described in detail elsewhere [4]. Briefly, the particles are entrained in a cold N_2 stream and are then injected along the centerline at the base of the 40 cm high reactor. Particle loadings are kept low to insure that their presence has no influence on the free-stream gas properties. A two-color pyrometer is used to measure the temperature of the burning particles at discrete heights in the reactor. As the particle traverses the focal volume of the collection optics, the radiant emission passes through two different sized slits. The first slit is wider (1000 μm) than the diameter of the largest particle and the second is narrower (45 μm) than the diameter of the smallest particle. The ratio of the intensity of the radiant emission measured in the first slit to that measured in the second slit is directly proportional to the diameter of the particle. The temperature measurements are calibrated with a tungsten strip lamp; the size measurements are calibrated by comparison with the size distribution of well-characterized Spherocarb particles. The particle temperatures measured in this work ranged from 1440 ±20 K in 12 kPa O_2 to 2100 ±150 K in 36 kPa O_2. The measured particle diameters ranged from 80 to 170

μm which corresponds well with the -100/+170 mesh (90-150 μm) particles used to feed the reactor. The velocity of each particle is determined by measuring the time it takes the particle to traverse the large slit. The particle velocities measured in this work ranged from 2.40 to 3.10 (±0.05) m/s depending on the gas temperature.

To reduce the influence of spurious signals, 200 to 300 particles were monitored at each height and the particles were grouped in bins approximately 10 μm apart, based on their measured diameter. In this paper, a measured particle diameter refers to the diameter at the center of a bin containing at least 10 particles. A measured particle temperature or velocity refers to the average temperature or velocity for all of the particles in a given bin.

A hot, one-dimensional, laminar oxidizing gas environment is generated by a 5 cm x 5 cm array of 0.2 cm diameter $CH_4/H_2/O_2/N_2$ diffusion flamelets. The total pressure in the reactor is constant and equal to 101 kPa. Post flame O_2 partial pressures from 3 to 36 kPa and gas temperatures from 1400 to 1900 K are attained by careful control of the inlet gas mixture. During analysis of the experimental data, we found that Saran char had a negligible burning rate in 3 and 6 kPa O_2 environments. Therefore, in the remainder of this paper, we only present data obtained at 12, 24, and 36 kPa O_2. Typical post flame partial presures of H_2O and CO_2 are 16 and 2 kPa, respectively.

Gas temperatures, T_g, are determined from radiation-corrected measurements using a Pt-Pt/13%Rh thermocouple. The gas velocity in the reactor can be modeled as,

$$\sqrt{\frac{\overline{v_g}}{T_g}} = C_1 + 0.5\sqrt{\overline{C_2 z T_g^{0.68}}} + \frac{C_2 z T_g^{0.68}}{8\sqrt{\overline{C_1}}} \qquad (1)$$

where z is the height in the reactor, C_1 and C_2 are constants that are fit to the data for each gas condition, and the two $T_g^{0.68}$ terms account for the influence of T_g on the gas viscosity. Eqn. (1) represents the solution of the conservation equation governing one-dimensional flow in a square conduit, assuming that the boundary layer along each wall develops independently and that the fraction of the total mass flowing in the boundary layer is proportional to the boundary layer thickness. C_1 and C_2 are chosen to give the best fit between the measured particle velocities and the particle velocities calculated by solving the particle momentum balance (see Eqn. (3) below). An important implicit assumption in this analysis is that the density of the particles are approximately independent of burning time. This assumption is consistent with the results of the kinetic analysis discussed below.

The Saran char is made by heating Saran co-polymer (supplied by the Dow Chemical Company) to 1300 K in flowing N_2 for three hours. The exact procedure used to manufacture the Saran char is described elsewhere [5]. Saran char contains no volatiles and approximately 0.5 wt% ash. Its apparent bulk density is 0.35 g/ml and its total surface

area is 1260 m^2/g, as determined by CO_2 adsorption at 298 K analyzed using the Dubinin-Radushkevich isotherm. The only impurities detected by Proton Induced X-ray Emission Spectroscopy (PIXE) are 2300 ppm Cl, 22-30 ppm Ti, 10 ppm Fe, 7.2 ppm Cu, 1 ppm Zr, and 1 ppm Re.

Theory

The equations used to follow the mass, velocity and temperature of a particle as it burns in the laminar flow reactor are given below:

$$v_p \frac{dm}{dz} = -\rho \pi d_p^2 \tag{2}$$

$$m v_p \frac{dv_p}{dz} = -mg - 3\pi\mu d_p (v_p - v_g) \tag{3}$$

$$\frac{-m v_p C_p}{\pi d_p^2} \frac{dT_p}{dz} + \rho H = \frac{2k(T_p - T_g)}{d_p} + \sigma \varepsilon_p (T_p^4 - T_w^4) \tag{4}$$

The momentum equation (Eqn. (3)) accounts for gravitational and Stokes forces and the energy balance (Eqn. (4)) accounts for the thermal inertia of the particle, the heat of reaction, gas phase conduction, and radiation. The mass, m, of the char particle is determined from its apparent density and diameter, d_p. The particle velocity is v_p and ρ is the particle burning rate per unit external surface area. The velocity of the gas is given by v_g and g is the gravitational constant. The heat capacity of the particle, C_p, is taken to be that of graphite and the physical properties of N_2, the major component in the gas stream, are used for the free-stream gas properties. The viscosity, μ, and thermal conductivity, k, of the gas are evaluated at the mean temperature (T_m) between the gas and particle temperatures. The temperatures of the particle, the gas, and the medium to which the particle radiates are given by T_p, T_g and T_w (500 K), respectively. The Stefan-Boltzmann constant is denoted by σ, and ε_p denotes the particle emissivity (taken as 0.85). The heat released per gram of carbon consumed, H, is calculated assuming that CO is the primary combustion product.

The overall burning rate of the particle is described by:

$$\rho = k_d (P_g - P_s) = k_s P_s^n, \tag{5}$$

where P_g and P_s are the oxygen partial pressures in the bulk stream and at the surface of the particle, respectively, k_s and k_d are the chemical rate and diffusion coefficients, respectively, and n is the apparent oxygen reaction order. The chemical reaction rate coefficient includes contributions from intraparticle diffusion limitations and the intrinsic reactivity of the Saran particle. In the Arrhenius form, k_s is given as,

$$k_s = A \exp(\frac{-E}{RT_p}), \quad (6)$$

where A is the preexponential factor, E is the activation energy, and R is the universal gas constant. The external diffusion rate coefficient is given by:

$$k_d = \frac{2M_c D_{ox}}{RT_m d_p}, \quad (7)$$

where M_c is the molecular weight of carbon and D_{ox} is the diffusion coefficient of oxygen evaluated at T_m.

The computational scheme employed to obtain the overall particle burning rate parameters, A, E, and n, is initiated by setting dT_p/dz equal to zero in Eqn. (4) and then using the measured d_p and T_p to calculate ρ. Using Eqns. (5) and (7), P_s can be calculated from ρ. The rate parameters are then obtained from Eqns. (5) and (6) by fitting T_p and P_s to the calculated rate using a linear least-squares routine. These parameter values are used as the first guess in the numerical integration of Eqns. (2), (3) and (4), where ρ is obtained from an implicit expression which is independent of P_s by rearrangement of Eqn. (5). The integration employs the measured T_g profile. The initial conditions used for the integration are T_p = 300 K and v_p = 0.3 m/s. A range of initial particle diameters (from 90 μm to 190μm) in 5 μm intervals is used. When the integration reaches a height (z) where experimental measurements have been taken, the calculated relationship between dT_p/dz and d_p is used to find dT_p/dz for each measured particle size. This measured dT_p/dz is then used in Eqn. (4) to obtain a new ρ, from which updated values of the kinetic parameters are obtained for the next numerical integration. Successive iterations of this strategy are used to converge on the rate parameter values that best describe the behavior of the Saran particles. The quality of fit can be judged from the agreement between the calculated and measured T_p as a function of d_p. Both constant density and constant diameter burning are considered as limiting cases for effectiveness factors of approximately zero and one respectively. The particle ignition temperature is taken as 1000 K below which the particle burning rate is set equal to zero. Changing the ignition temperature from 300 K to 1100 K does not affect the results of this analysis.

Results and Discussion

Equations (2), (3) and (4) can be solved to calculate the predicted relationship between particle temperature and size for a given gas environment. For the 12 kPa O_2 environments at a peak gas temperature less than 1700 K and in all O_2 environments less than 12 kPa, the measured particle temperatures can be fit by setting ρ equal to zero. This is in direct contrast to the burning characteristics of an hvb-bituminous coal observed by Mitchell and co-workers [2], which exhibited appreciable reaction rates in O_2 environments as low as 3 kPa. This may be attributed to two factors: (1) the homogeneous combustion of the volatile matter (33% by weight) in the coal

increases the temperature of the resulting char and (2) the catalytic properties of the ash (21% by weight) increase the burning rate of the char.

If the measured particle temperature does not exceed the calculated zero-burning temperature by the approximate error in our temperature measurement (±20-150 K), we can not calculate a statistically significant burning rate. Defining χ as the ratio of the calculated burning rate to the diffusion-limited burning rate ($\chi=\rho/k_d P_g$), we observed that the difference in particle temperature between χ's of 0.0 and 0.1 approximately corresponds to the error in the measured particle temperature. Therefore, no measurements which give a χ below 0.1 are considered in the determination of the rate coefficients and oxygen reaction order. For the conditions of these experiments, values of χ ranged from 0.1 to 0.6 which indicates that the overall burning rate has a high sensitivity to the kinetic rate.

For an O_2 partial pressure of 36 kPa, 100 μm particles are predicted to burn out at approximately 10 cm in the reactor, if constant diameter burning is assumed. This contradicts the experimental observation of particles as small as 90 μm at 19 cm in the reactor. While a constant diameter model may be more applicable at lower O_2 pressures, this model was not used in our analysis of the combustion kinetics. An analysis incorporating an effectiveness factor into the particle burning rate expression will be considered in future work.

Constant density burning gives good fits to the experimental data at bulk oxygen pressures of 12 and 24 kPa and poor fits to the 36 kPa data (see Figures 1, 2 and 3). A least squares fit of the kinetic rate parameters and oxygen reaction order to the calculated reaction rates at 12, 24 and 36 kPa gives

$$\rho = 6.3\times10^{-3} \exp\left(\frac{-27000}{RT_p}\right) P_s^{0.8} \qquad (8)$$

where R is given in cal/mol K and P_s is given in Pa. An Arrhenius plot of the rate coefficient, k_s, versus $1/T_p$ is presented in Figure 4. The relationship between (ρ/k_s) and P_s is depicted in Figure 5.

A possible reason for the discrepancy between the calculated and experimental rates for the 36 kPa data set is that the simple diffusion model considered here does not account for the large amount of CO which must diffuse out of the particle boundary layer at higher burning rates (Stefan flow). We do note, however, that when the 36 kPa data is analyzed alone, the calculated rates fit the data better, but the activation energy is lower (~17000 cal/mol) which is indicative of intraparticle diffusion limitations.

Acknowledgements

The experimental work was performed at the Combustion Research Facility, Sandia National Laboratories and was sponsored by the U.S. Dept. of Energy through PETC. The computational work was performed at

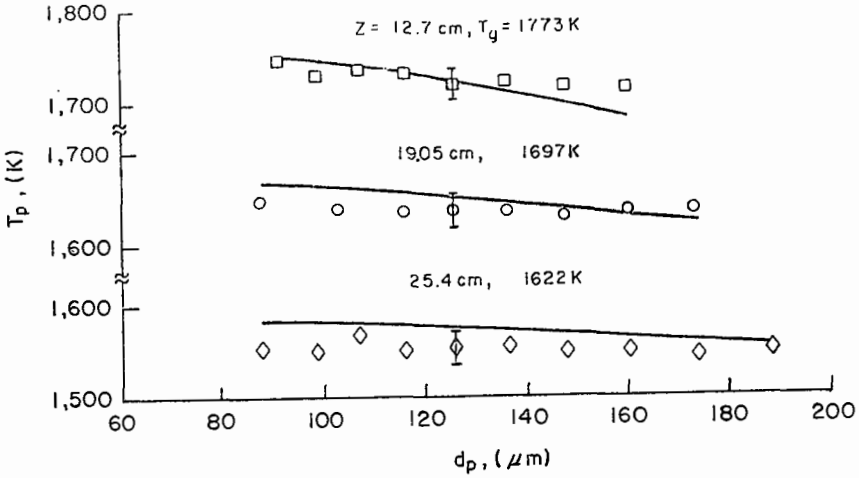

Figure 1. Particle temperature versus diameter as a function of height in the reactor. Free stream oxygen pressure is 12 kPa. (χ = 0.1-0.3)

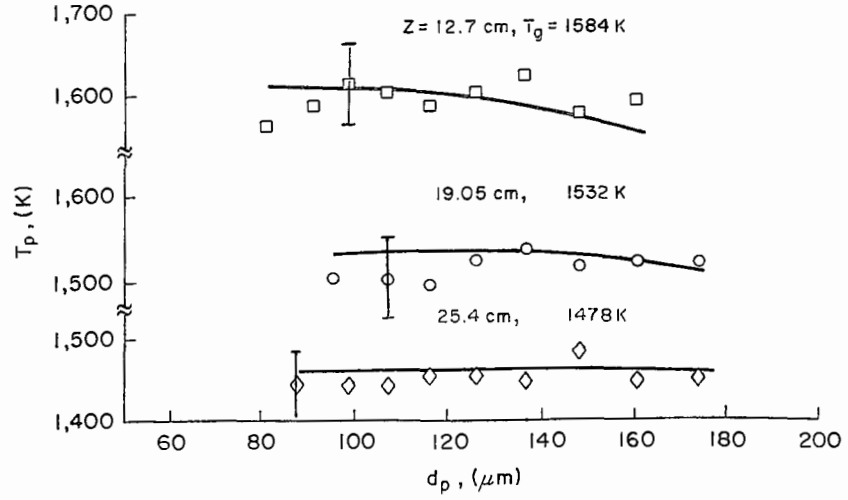

Figure 2. Particle temperature versus diameter as a function of height in the reactor. Free stream oxygen pressure is 24 kPa. (χ = 0.1-0.3)

the Purdue University Computing Center and was sponsored by the Coal Research Center at Purdue University. B.J.W. acknowledges the support provided by the D.O.E. through Associated Western Universities.

References

1. Mitchell, R.E., Tichenor, D.A. and Hencken, K.R., Proceedings of the 1985 International Conference on Coal Science, International Energy Agency, 1985, p.375.

2. Mitchell, R.E., Tichenor, D.A. and Hencken, K.R., Second Annual Pittsburgh Coal Conference Proceedings, Pittsburgh, Sept. 16-20, 1985, p.648.

3. Tichenor, D.A., Mitchell, R.E., Hencken, K.R., and Niksa, S. Twentieth Symposium (Int.) on Combustion, Ann Arbor, Aug. 12-17, 1984.

4. Hardesty, D.R., Pohl, J.A. and Stark, A.H., Sandia Report SAND78-8234, Sandia National Laboratories, Livermore, CA, 1978.

5. Waters, B.J., M.S. Thesis, Purdue University, 1985.

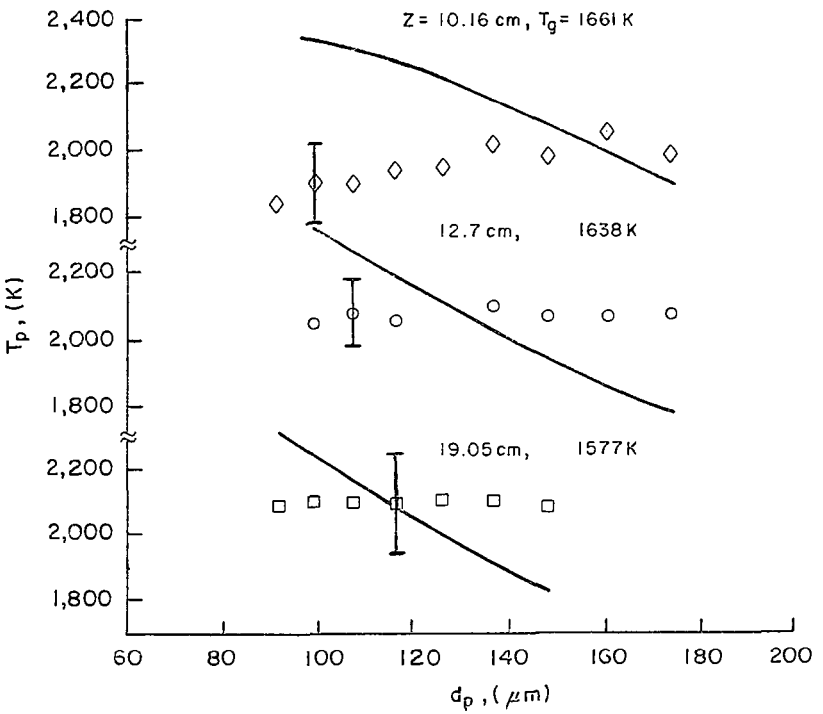

Figure 3. Particle temperature versus diameter as a function of height in the reactor. Free stream oxygen pressure is 36 kPa. (χ = 0.3-0.6)

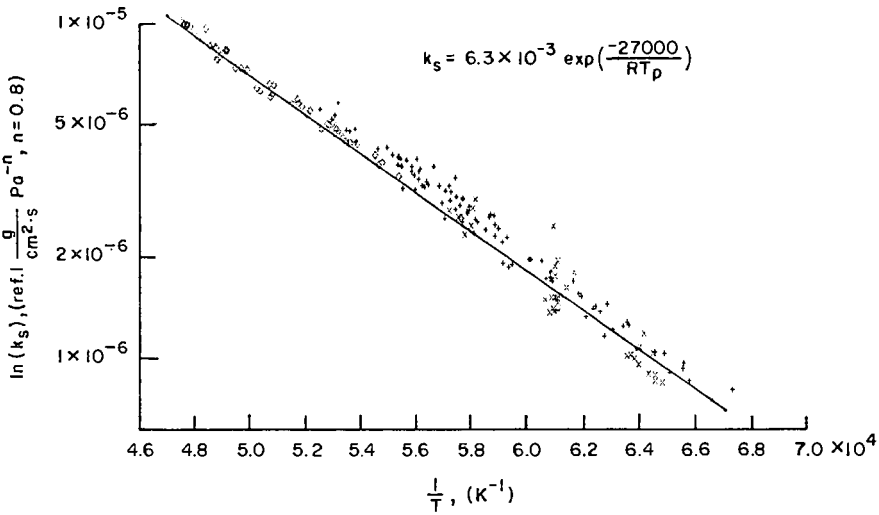

Figure 4. Temperature dependence of k_s.
Free stream oxygen: ◇ - 36 kPa; + - 24 kPa; × - 12 kPa.

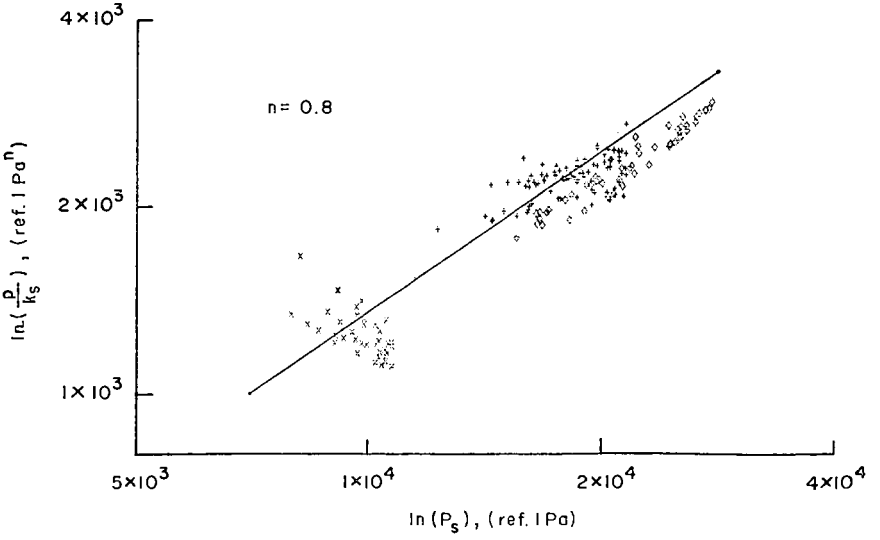

Figure 5. Surface oxygen pressure dependence of $\frac{p}{k_s}$.
Free stream oxygen: ◇ - 36 kPa; + - 24 kPa; × - 12 kPa.

Effect of $CaCl_2$ on Char Reaction Kinetics

M. A. Serageldin and W. P. Pan

Department of Chemistry and Chemical Engineering
Michigan Technological University
Houghton, MI 49931

INTRODUCTION

This work describes the effect of $CaCl_2$ on coal char reactivity; it is the third part in a series of studies related to boiler application (1,2) involving this metal-based salt. The information obtained in this work should be useful in understanding the effect of similar materials on the oxidative behavior of coal-char. The char was combusted in a thermogravimetric analyzer, TGA, under different partial pressures of oxygen (0.16 - 70% by vol.) in nitrogen and at constant temperature. The furnace temperatures (isothermal) varied between 673 and 1223 K. The sample mass and volumetric flow rate were close to 2 mg and 5 ml/s, respectively. This temperature range should cover the regions where oxidation occurs mainly by diffusion and mainly by chemical control (3,4).

EXPERIMENTAL

Materials

Lignite coal from Velva Mine, North Dakota, was used in this work; its proximate and ultimate analysis is given in Table 1.

Char preparation

The coal was placed in a boat made of ceramic material and pyrolyzed in a Hoskin electric furnace (Hoskin Co.), which was regulated by an Omega 6000 temperature controller. The boat was made by splitting a length, l, of high purity alumina tube (l = 75 mm and I.D. = 10 mm); it was positioned in the center of the furnace. A shielded Chromel Alumel thermocouple (d = 3 mm) was placed approximately 5 mm above the boat to measure the sample temperature. The sample thermocouple reading (in the absence of a sample) was a few degrees lower than that of the furnace set temperature; for example, at the set temperature of 1248 K, the sample thermocouple (inside the furnace) recorded 1223 K.

Coal pyrolysis in a constant stream of nitrogen (0.425 ml/s at S.T.P.) was achieved over a number of steps (5). The sample was first purged at room temperature for 900 s (0.9 ks). The furnace was then switched on, setting the maximum temperature to 1248 K (which was reached in about 2.58 ks). It was left for one hour at the maximum temperature. The furnace was then turned off and left to cool in nitrogen for one hour, after which the remaining part of the coal sample, i.e. char, was emptied in a clean, dry container which was subsequently stored in a dessicator for later use.

Apparatus

The char was burned in a DuPont 951 thermogravimetric analyzer (TGA) coupled with a DuPont 990 recorder unit. Each sample (2 mg) was spread evenly on the platinum pan to avoid establishing a thermal gradient in the sample. O_2 and N_2 were mixed by different proportions. The total gas flow made by O_2 and N_2 was maintained at 5 ml/s. This provided a linear velocity of 18 mm/s. The percentage of O_2 in the O_2/N_2 mixture depended on the isothermal temperature: at the higher isothermal temperature (1223 K), the lower concentration (or partial pressure) of oxygen was used, i.e. 0.16% by volume, whereas a concentration of 70% O_2 was used when the isothermal temperature was set to the lowest value investigated, i.e. 683 K. Such combinations were necessary to maintain the value of the time to 50% decomposition, $t_{0.5}$, above 1200 s, thus ensuring that the effect of temperature gradient is negligible (4). Lastly, before pushing the sample into the furnace, the latter was heated to the desired isothermal temperature

and left to equilibrate for 300 s. This procedure helped to reduce the time-lag before the sample reached the desired temperature.

RESULTS

Information regarding the influence of $CaCl_2$ on char reactivity, reaction mode, and kinetic parameters is presented in this section.

Reactivity

The influence of oxygen concentrations and temperature on char reactivity is shown in Figure 1. A greater effect (on conversion) was produced as a result of increasing the temperature by a small percentage than by an equivalent increase in oxygen percentage in the gas. Treating the char with $CaCl_2$ also increased its level of conversion, Figure 2. Considering that conversion vs. time plots for chars under different atmospheres are similar in appearance, a more satisfactory representation, in terms of reactivity, can be achieved by replotting conversion against a dimensionless time, $t/t_{0.5}$ (6). Such a plot is given in Figure 3 and indicates that $CaCl_2$ produces an insignificant effect below a conversion of ~0.58 which would suggest that the mechanism of reaction is not altered within this zone. Between 0.58 conversion and up to ~0.68 the "master curve" separated into two curves, one for char and the other for char plus $CaCl_2$. Above a conversion of 0.68 each of the above curves split into three curves, producing a total of six curves. Such a spread was not observed when char from demineralized coal was carbonized at around 1273 (6). However, evidence showing the effect of naturally occurring mineral matter in coal-char may be found (beyond a char conversion of 0.7) in Figure 1 of Tseng and Edgar's paper (4). It is, therefore, understandable that in the presence of additional mineral matter (i.e. $CaCl_2$), as in this study, a more pronounced effect occurs. This is clearly indicated (Figure 3) by a greater shift of the catalyzed reaction to the left, i.e. towards a pore diffusion mode of reaction (Figure 4). The spread in the curves may be attributed to the effect of particle temperature rise (7).

Reaction Mode of Control

To determine the mechanism controlling the reaction the data used to plot Figures 3 and 4 was replotted in terms of specific rate, $dC/d\tau$, and $t_{0.5}$, the time to 50 percent conversion. Values of $dC/d\tau$ were obtained using the cubic spline interpolation technique (8) and the cubic spline smoothed technique. Figure 5 illustrates the extent of scatter when the cubic spline smoothed technique was not applied (white circles) to the data from Figure 3. This method was previously used by Tseng and Edgar (4) to compare the reactivities of different chars in the absence of catalysts. Figure 6 shows a number of curves obtained using this procedure for char combusted at several of the low temperatures investigated and different oxygen levels. A maximum occurred in all cases at around 0.25 conversion, which indicates that the control mechanism is chemical (3,4). Beyond 0.58 the curves delineating the different experimental conditions separated and were therefore clearly identifiable. From this presentation one can see that the maximum specific rate at a given temperature was somewhat increased by treatment with $CaCl_2$. It should be stated that when the conversion was less than 0.5, Figure 6 provided more detail than Figure 3.

Figure 4 was obtained by treating the data corresponding to the runs at high temperature (>1123 K). The data for the six experiments followed very closely the film diffusion theoretical curve (dotted line). The theoretical lines in Figure 4 were calculated using the equations provided in reference 4.

Kinetic Parameters

The order of reaction in the kinetic control regime was determined by plotting $t_{0.5}$ against oxygen partial pressure (0.16 - 70 KPa) on log-log paper (4) and measuring the slope. Figure 8 shows such plots obtained at different temperatures for untreated char. The slope of the different lines was practically the same, suggesting that the average value of n for the char was 0.84. This figure is somewhat higher than 0.70 reported by a number of workers for lignite coal (see ref. 4). The value of n for char treated with $CaCl_2$ was 0.73. Both values of n are valid for a limited temperature range, i.e. 683 - 723 K. In the diffusion control regime n equals

one (9). The activation energy was obtained by plotting $t^*_{0.5}$, against 1/T on semi-log paper as is illustrated in Figure 9. The former value is defined as follows (4):

$$t^*_{0.5} = (P_{O_2}/P^*_{O_2})^n . t_{0.5} \qquad 1)$$

where $t_{0.5}$ corresponds to the value at a base of reference partial pressure of oxygen, P_{O_2}. This was chosen to be 0.005 MPa in the present study. On the other hand, the values marked with an asterisk correspond to char reacted at the same temperature under other partial pressures of oxygen. n is the reaction order. Figure 9 illustrates results for both the high temperature runs (lower left of figure) and the low temperature runs (upper right of figure). Each circle shown in Figure 9 represents the average of four runs at different P_{O_2}, i.e. the points at a given temperature fall within the bounds of such circles. However, for calculating the activation energy, all the points were used. For example, all the runs shown in Figure 8 were used to calculate the activation energy, E, in the kinetic regime. This was equal to 154 KJ/mol for char and was reduced to 141 KJ/mol when the char was treated with $CaCl_2$. However, for the higher temperature runs where the mode of control was diffusional, the value of E for the untreated char was 29.5 $\pm$ 0.5 and for the treated char was 28.0 $\pm$ 0.5 KJ/mol. The fact that the difference is insignificant suggests that char combustion under such a regime is independent of the nature of the catalyst, a point made before by others (3,10). The activation energy in the chemical control regime may also be obtained using the following equation:

$$\log_e(P_{O_2}{}^n . t^*_{0.5}) = \log_e A' + E/RT \qquad 2)$$

where A' is a measure of the char reactivity (4) and can be expressed as :

$$A' = (1/AS_o)\int_0^{0.5} (S_o/S)\,dC \qquad 3)$$

A in Equation 3 is the Arrhenius pre-exponential factor; S_o, is the specific surface area at time zero and dC is the fraction converted. Values of A' and E obtained using Equation 2 are shown in Table 2 and indicate that the reactivity of the treated char was significantly increased as a result of adding $CaCl_2$. The higher reactivity can also be deduced from Figure 10.

To evaluate the mass transfer resistance the Sherwood number of the char samples were calculated (Appendix 1) (4) for the data in the film diffusion controlled regime and summarized in Table 3. These values are significantly increased in the presence of $CaCl_2$ and by temperature; however, they have a value less than 2 which refers to a spherical particle suspended in stagnant air. The occurrence of a lower Sherwood number was attributed by Tseng and Edgar (4) to a reduction in mass transfer efficiency by the sample pan (4). They also concluded that the mass transfer resistance around a single large particle would be lower than that around smaller particles on a pan. In the latter case the particle packing is also important.

DISCUSSION

This work shows that $CaCl_2$ promotes the overall decomposition of coal-char, i.e. it occurs during a shorter time, at constant temperature. This is in agreement with previous results but under temperature programming (non-isothermal) conditions (11). In this case the same level of conversion occurred at a lower temperature which indicates agreement between isothermal and non-isothermal studies.

Since changes in porosity and density prior to oxidation can influence reactivity, these were measured for char prepared from coal and that for coal mixed with $CaCl_2$ (12). From Table 4 we can deduce that there is no significant change in density, total pore volume and porosity prior to combustion. Therefore the effectiveness of the additive in promoting char-oxygen reaction may be explained in terms of the following carbon-oxygen reactions (13,14):

$$CaO + 1/2\ O_2 \longrightarrow CaO_2 \qquad 4)$$
$$CaO_2 + C \longrightarrow CaO + CO \qquad 5)$$

In the above model the catalyst promotes the dissociation of the oxygen molecule adsorbed making it thus more reactive. In other words, dissociative adsorption is promoted (14). Such a

mechanism could account for the observed decrease in activation energy in the chemical control regime.

In the diffusion control regime E did not vary significantly, which would suggest that the above explanation is not applicable in this case. However, the fact that E was ~28 KJ/mol, i.e. higher than the usually accepted range of 8 - 12 KJ/mol (9), would suggest that it is possible that the regime is not totally film diffusion controlled, but that pore diffusion may also be important during the initial decomposition stage, Figures 7 and 9. (E for pore diffusion is around half of the intrinsic activation energy.) This reasoning could account for the observed shorter char decomposition time, which is indicated by lower values of $t_{0.5}$. The significance of the Sherwood numbers in Table 3 is now questionable. The results indicate that $CaCl_2$ increases this number significantly and, therefore, under these conditions, mass transfer resistance was reduced. However, we can see that the values of the constant b for the film diffusion controlled regime was not significantly altered by $CaCl_2$. The theoretical value of b is 0.55 (4). The use of this form of the Sherwood number may be misleading considering that we do not have single spherical particles as assumed in the derivation by the authors (4) and considering that we have reason to believe that pore diffusion may also be involved.

CONCLUSIONS

1. $CaCl_2$ decreased the activation energy and increased the reactivity of coal char in the chemical control regime. It did not, however, have an important effect the diffusion control regime.
2. In the kinetic control regime the mechanism was not altered below a conversion of 0.58. However, at higher conversion the reaction was moved towards the pore diffusion regime.
3. At the higher temperatures pore diffusion may also play a role during decomposition, which explains why the activation energies obtained were higher than that for a totally film diffusion controlled regime.

REFERENCES

1. Serageldin, M.A. and Pan, W.-P., "Effect of $CaCl_2$ on Coal Decomposition: Pollution", presented at the 39th ACS Fall Scientific Meeting, Midland, Michigan, 1983.
2. Serageldin, M.A. and Pan, W.-P., "Corrosion-Effects of Increasing the Chloride Level in Coal", Proceedings of the 9th International Congress on Metallic Corrosion, Toronto, Canada, Vol. 1, 1984, pp. 504-11.
3. Dutta, S. and Wen, C.Y., *Ind. Eng. Chem.*, Process Des. Dev., 16(1), 1977, pp 31-7.
4. Tseng, H.P. and Edgar, T.F., *Fuel*, 63, 1984, pp. 385-93.
5. Hippo, E.J., Jenkins, R.G. and Walker, P.L., Jr., *Fuel*, 58, 1979, pp. 338-44.
6. Mahajan, O.P., Yaizab, R. and Walker, P.L., Jr., *Fuel*, 57, 1978, pp. 643-6.
7. Essenhigh, R.H., in "Coal Conversion Technology" (Eds, Wen, C.Y. and Stanley Lee, E.), Ch. 3, 1979, pp. 171-312.
8. IMSL Library Reference, IMSL Inc., 9th Edition, Vol. 2, 1982, pp I-1, ICSCCU-1.
9. Satterfield, C.N., "Mass Transfer in Heterogeneous Catalysis", MIT Press, Massachusetts, 1970.
10. Weisz, P.B. and Goodwin, R.D., *J. Of Catalysis*, 2, 1963, pp. 397-404.
11. Pan, W.-P. and Serageldin, M.A., "Effects of $CaCl_2$ on reactivity of coal under non-isothermal condition", in preparation, 1985.
12. Pan, W.-P. and Serageldin, M.A., "Structure Characterization in Coal and Char with $CaCl_2$", in preparation, 1985.
13. McKee, D.W. in "Chemistry and Physics of Coal Utilization - 1980" (Eds, Cooper, B.P. and Petvabis, L.) AIP, 1981, pp. 236-55.
14. Morgan, B.A. and Scaroni, A.W. in "The Chemistry of Low-Rank Coals", ACS Symposium Ser. 264, Ch. 16, 1984, pp. 255-66.

Appendix 1: Sherwood Number

$$Sh = \frac{(1-X_a)\rho_p r_o^2 RT}{D_b \omega P_{O_2} t_{0.5}} (1 - \sqrt[3]{1/4}) \qquad 1)$$

where X_a is the ash yield; ρ_p, particle density; r_o, initial particle radius; D_b, bulk diffusivity; R, the gas constant; T, the absolute temperature; P_{O_2}, partial pressure of oxygen; $t_{0.5}$, time to 50% decomposition and $\omega = 12$, assuming all C -> CO_2.

Table 1: Analysis of lignite coal (-100, +270) mesh

Proximate analysis As received		Ultimate Analysis Moisture-Ash free	
Moisture(wt%)	34.00	Carbon	64.55
Fixed Carbon	27.46	Hydrogen	4.72
Volatiles	32.86	Nitrogen	1.02
Ash	5.68	Sulfur	0.33
		Oxygen*	29.38

*by difference

Table 2: Values of A' and activation energy

Sample	A'	Activation energy (KJ/mol)
untreated char	9.3×10^{-10}	154 ± 1
$CaCl_2$ treated char	68.4×10^{-10}	141 ± 4

Table 3: Sherwood number and film diffusion constant (b) of char samples

Temperature (K)	Sherwood number Untreated char	Sherwood number $CaCl_2$ treated char	$dC/d\tau = b(1-C)^{1/3}$ untreated char	$dC/d\tau = b(1-C)^{1/3}$ $CaCl_2$ treated char
1123	0.76	1.11	0.59 ± 0.03	0.56 ± 0.02
1173	0.91	1.23	0.59 ± 0.02	0.57 ± 0.02
1223	1.26	1.52	0.57 ± 0.03	0.57 ± 0.02

Table 4: Density, total pore volume and porosity (12)

Sample	Density (g/cm^3) Helium	Density (g/cm^3) Mercury	Total pore volume (cm^3/g)	Porosity (%)
untreated char	2.12	1.30	0.298	38.7
$CaCl_2$ treated char	2.14	1.32	0.29	38.5

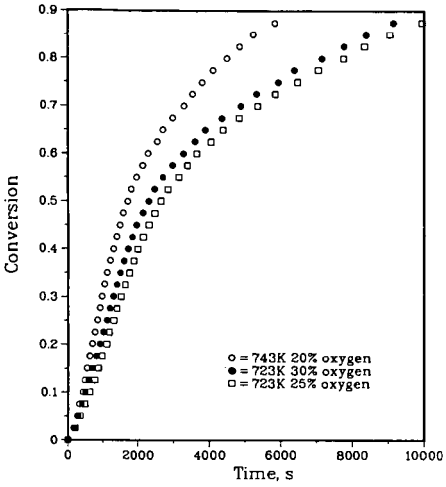

Figure 1: Influence of oxygen concentration and temperature on reactivity of char.

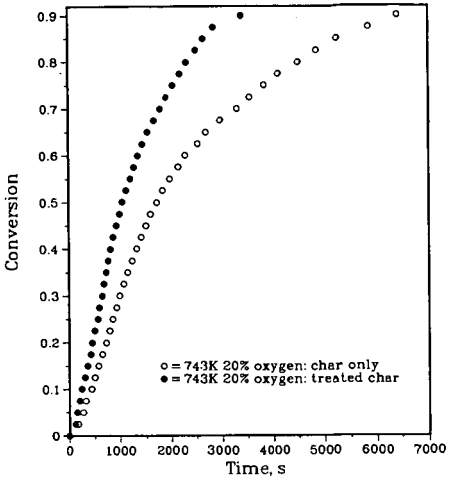

Figure 2: Effect of $CaCl_2$ on the reactivity of char.

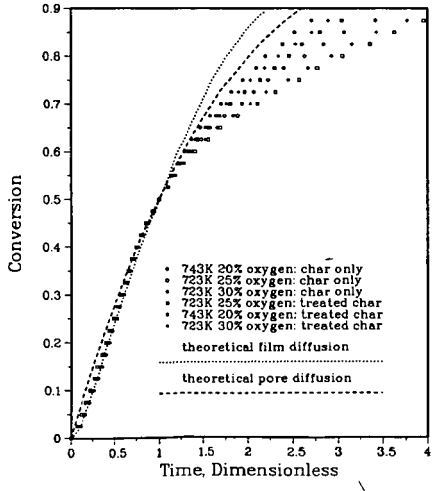

Figure 3: Effect of $CaCl_2$ on the normalized plot of char at different temperatures and oxygen concentrations.

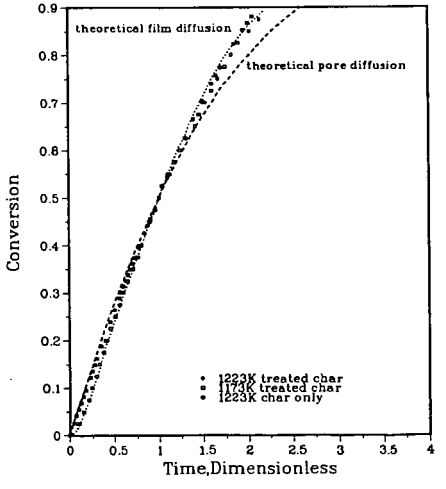

Figure 4: Effect of $CaCl_2$ on the normalized plot of char under diffusional control.

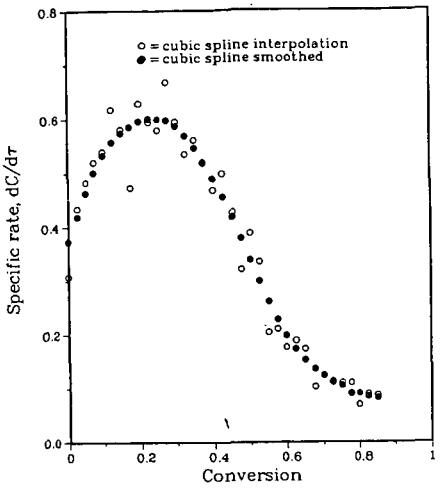

Figure 5: Application of cubic spline interpolation technique and cubic spline smoothed technique.

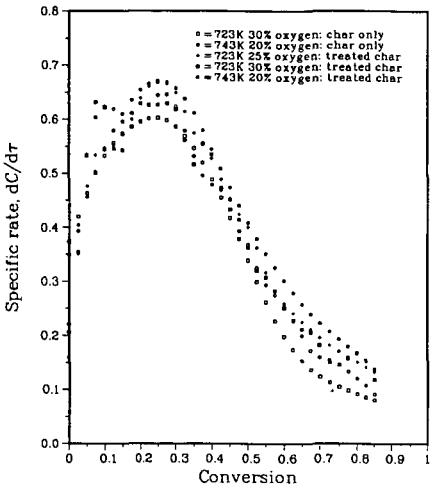

Figure 6: Effect of $CaCl_2$ on the combustion characteristic curve of char under chemical control.

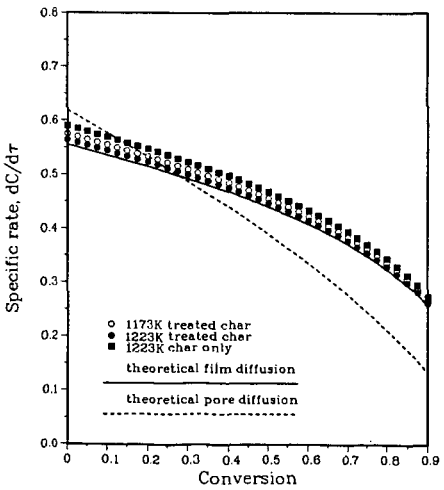

Figure 7: Effect of $CaCl_2$ on the combustion characteristic curve of char under diffusional control.

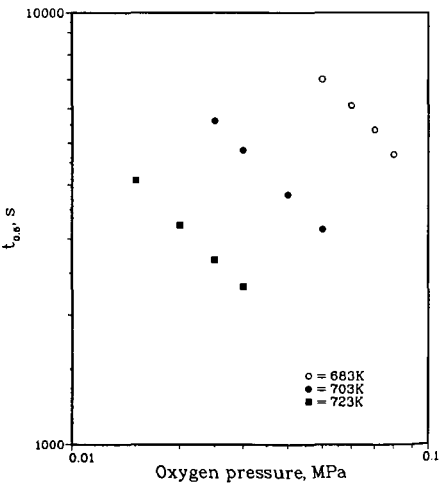

Figure 8: The reaction order of char.

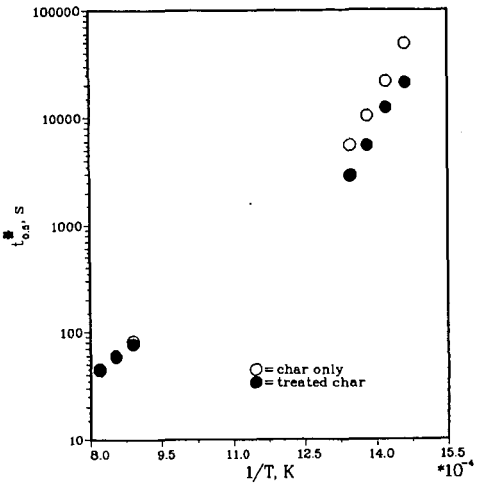

Figure 9: The effect of $CaCl_2$ on the char activation energy.

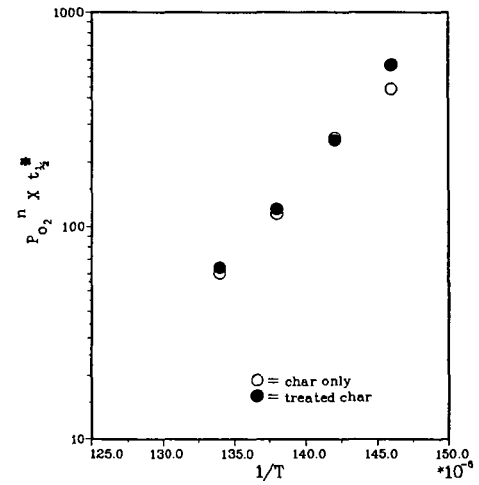

Figure 10: Comparison of the reactivity of char in the presence and absence of $CaCl_2$.

INFLUENCE OF METAL IONS AND PYROLYSIS CONDITIONS ON CARBON DIOXIDE GASIFICATION OF WOOD CHARS

William F. DeGroot and G.N. Richards

Wood Chemistry Laboratory, University of Montana, Missoula, MT 59812

INTRODUCTION

The rate of biomass gasification is limited by the reaction rate of the thermally stable char which forms as a result of the initial pyrolytic degradation. This char also represents a large proportion of the energy content of the original biomass (1), and efficient conversion of the biomass should recover the energy value of this fraction. This can be achieved by reaction with oxygen, steam, or carbon dioxide, and the intent of this research was to investigate the effects of reaction conditions and inorganic catalysts on the gasification of wood chars. These chars also provide an excellent model for studying the gasification reactions of coal, since sample pretreatment and pyrolysis conditions can be varied to provide a wide range of chemical functionality in the resulting chars. Studying the chemical structure and reactivity of these chars can provide important insight into parallel reactions in coal and other carbonaceous materials.

Previous work in our laboratory on the gasification of biomass chars indicated that the inorganic species naturally present in wood were effective gasification catalysts (2), and that some of the natural inorganic species were exchangeable with cations of salts added to the wood in solution. We have studied this ion exchange process further and have found that the wood sample used in these studies contains approximately 8 meq/100 g of carboxylic acid groups, primarily as 4-O-methyl-glucuronic acid groups associated with the hemicellulose fraction of the wood (3). In this study we have added catalysts to previously acid-washed wood through ion exchange in order to incorporate a single catalytic species in a highly dispersed form and at a reproducible level. Selected samples were also treated beyond the ion exchange capacity in order to distinguish the effects of exchanged cations as opposed to adsorbed salts.

EXPERIMENTAL

The wood sample used in this study was black cottonwood (Populus trichocarpa), a low-grade western hardwood. The heartwood and sapwood were separated and the sapwood was the primary sample studied. The wood was ground in a Wiley mill, and the 20/30 mesh fraction was retained for analysis.

Acid-washing (H^+-exchange) and ion exchange treatments were carried out by column percolation. The wood was degassed in a small quantity of the solution used for ion-exchange and transferred to a glass chromatography column. A 0.01 M solution of the acetate salt of the cation to be exchanged (at least a ten-fold excess) was then washed slowly through the column. The column was washed thoroughly with distilled, deionized water to remove any of the salt which was not bound by ion exchange. In order to add catalytic species beyond the exchange capacity of the wood, the wood was soaked in a 0.01 M solution of the acetate salt and then air-dried. All of the catalyst treatments were carried out using acid-washed wood in order that the treated samples contain only a single catalytic species.

The inorganic constituents of the wood samples were analyzed by inductively coupled argon plasma (ICP) emission spectroscopy, except for nickel which was analyzed by atomic absorption (AA) spectroscopy. Ash contents were determined by thermogravimetry (TG) at 550°C in air.

Chars were prepared in a tube furnace purged with flowing nitrogen. The wood sample was held in a porcelain boat which was pulled into the preheated furnace. After heating for a prescribed time the sample was pulled into a water condenser at the downstream end of the furnace tube, where it was cooled to approximately 10°C before being exposed to the air. Samples were stored in nitrogen- or argon-purged containers.

Cross polarization/magic angle spinning ^{13}C nuclear magnetic resonance spectrometry (CP/MAS ^{13}C n.m.r.) of the chars was carried out at the Colorado State University Regional N.M.R. Center.

Gasification was carried out in the gasification reactor/detector system depicted in Figure 1. The reactor consisted of a 1/8" I.D. alumina tube (99.8% alumina) heated by an external nichrome wire coil. The sample (3-10 mg) was confined within a 1.0 cm section of the tube by 1/8" O.D. 4-hole ceramic insulators, which also carried gas flows into and out of the reactor. The lower insulator contained a chromel-alumel thermocouple that extended 3-4 mm into the reactor and provided a reliable measure of the sample temperature throughout the reaction. The reactor was purged with a 30 cc/min flow of N_2 for inert conditions and an equivalent flow rate of CO_2 for gasification. Switching of gas flows and reactor temperature were under control of a data acquisition/control system.

Effluent gases from the reactor were mixed with a 10 cc/min air flow, causing the oxygen level of the air flow to be reduced by the stoichiometric quantity of oxygen required for combustion of any combustible gases formed by pyrolysis or gasification of the sample. The oxygen concentration of the combined gas streams was monitored by a 1/4" O.D. zirconium oxide oxygen sensor tube maintained at 900-950°K. This sensor was enclosed in a 1/2" O.D. quartz tube and produced an output proportional to the differential pressure of oxygen across its inner surface (flowing air reference gas) and outer surface (combined reactor and combustion air flows). The output of the oxygen sensor was converted to oxygen concentration during data acquisition according to the Nernst equation:

$$E = \frac{RT}{4F} \ln(P/P_{ref})$$

where R and F have their usual meanings, T is the detector temperature (°K) and P and P_{ref} are the partial pressures of oxygen in the sample and reference gases, respectively.

For the purposes of this study it was assumed that all of the combustible gases produced were CO, and the removal of one molar equivalent of O_2 from the gas stream was therefore due to the gasification of one molar equivalent of carbon. The extent of gasification determined in this manner was consistently within 10% of the measured change in char weight.

The rate of gasification of a char (HTT 800°C) prepared from cottonwood is shown in Figure 2. The detector output can be integrated over the entire run to give the total extent of gasification, or it can be integrated above the baseline defined by the rate of pyrolytic gasification to give the extent of gasification due to reaction with CO_2.

RESULTS AND DISCUSSION

The ash contents and composition of the inorganic fraction of the samples used in this study are shown in Table 1. The heartwood of the cottonwood has a very high ash content, approximately four times higher than the sapwood taken from the same tree. The main components of the natural inorganic fraction are calcium, potassium, and magnesium; in addition to these elements the lignite sample has a high concentration of iron. All of these elements are potentially active gasification catalysts.

Table 1. Composition of cottonwood, treated cottonwood and lignite samples.

Sample	% Ash	Composition of Ash (%, dry weight) K	Mg	Ca	Fe	Co	Ni	Cu
COTTONWOOD								
Untreated								
Heartwood	2.01	0.32	0.08	0.50	--	--	--	--
Sapwood	0.51	0.10	0.02	0.12	--	--	--	--
Ion-exchanged								
Sapwood								
Acid-washed	0.02	--	--	0.01	--	--	n.d.[b]	--
K^{+}-exchanged	0.41	0.28	--	0.02	--	--	n.d.	--
Mg^{+2}-exchanged	0.17	--	0.09	0.01	--	--	n.d.	--
Ca^{+2}-exchanged	0.34	--	--	0.14	--	--	n.d.	--
Co^{+2}-exchanged	0.34	--	--	0.01	--	0.23	n.d.	--
Ni^{+2}-exchanged	0.33	--	--	--	--	--	0.21	--
Cu^{+2}-exchanged	0.42	--	--	--	--	--	n.d.	0.32
Acetate Salt-treated								
Sapwood (0.01 M)[a]								
KAc	0.91	0.38	--	0.02	--	--	n.d.	--
$Ca(Ac)_2$	0.83	--	--	0.36	--	--	n.d.	--
$Co(Ac)_2$	0.89	--	--	0.01	--	0.40	n.d.	--
LIGNITE[c] (PSOC-837)	11.88	0.04	0.64	1.81	0.39	--	--	--

[a]Ion-exchanged samples were acid washed (H^{+}-exchanged) prior to treatmemt.
[b]n.d. = "not determined"; no value (--) = <50 ppm.
[c]Lignite sample and analysis provided by the Penn State Coal Data Base.

Table 2. Conversion due to pyrolysis (P) and gasification (G) of chars prepared from cottonwood and lignite at various heat treatment temperatures (HTT) and pyrolysis times. Chars were gasified for 30 minutes at 800°C in 90.9 kPa CO_2.

Sample	HTT (°C)	Time (min)	Char Yield (%)	% Conversion at 800°C P	G	Total
COTTONWOOD	800	10	13.1	1.6	32.5	34.1
(Sapwood)	900	10	11.5	1.7	30.9	32.6
	1000	10	10.4	1.2	15.9	17.1
	800	5	13.2	3.2	32.9	36.1
	800	30	12.6	1.7	31.9	33.6
	800	60	12.3	1.2	34.0	35.2
LIGNITE	800	10	61.5	3.6	66.5	70.1
	900	10	59.0	1.9	51.8	53.7
	1000	10	58.0	1.6	34.7	36.3

Acid-washing of the cottonwood sapwood removed most of the inorganic fraction, with the exception of a small quantity of residual calcium. When the acid-washed wood was treated by ion exchange with dilute salt solutions, the resulting samples contained 7-8 milliequivalents/100g with the exception of the Cu^{+2}-exchanged sample, which was treated at the 10 meq/100 g level. This is in agreement with the carboxyl content of 8 meq/100 g found previously for this sample, and indicates that ion exchange provides a high level of control for addition of inorganic cations to wood. The overall ash contents of the treated samples were all lower than that of the untreated sapwood. When the salt solution was dried onto the acid-washed wood without removing the free salts, the level of cation addition was 1.5-2.5 times higher than in the ion-exchanged samples.

Table 2 shows the effects of heat treatment temperature (HTT) and pyrolysis time on the char yields and reactivities of the resulting chars toward CO_2 gasification at 800°C. The char yields of the wood and lignite do not vary significantly within the temperature range and pyrolysis times studied. However, it is important to notice the differences in char yields between the wood and lignite samples, especially with respect to the concentration of inorganic species in the chars. The char yields from wood suggest that the ash is concentrated by a factor of 7-10, resulting in an ash content of 4-5% in the char. Similarly, the ash content of lignite char would be concentrated to nearly 20% of the weight of the char.

Reactivities of both the wood and lignite chars decreased by a factor of approximately two as the HTT was increased from 800°C to 1000°C. The contribution of pyrolysis to the gas yields in both samples was relatively small and it did not vary significantly under the conditions shown. Lignite char reactivity decreased approximately linearly between 800° and 1000°C. The reactivity declined more sharply above 900°C in the wood sample. This may indicate that one of the natural catalytic species in wood undergoes a specific transformation above 900°C, rendering it inactive, and that the reactivity of wood char is otherwise less dependent on HTT than is that of coal char. The extent of wood char gasification is independent of time of pyrolysis between 5 and 60 minutes. The dependence of reaction rate on HTT found in this study is somewhat less than that reported by Hippo et al. for a raw lignite gasified in steam (4). These workers report nearly a three-fold increase in reactivity in steam at 750°C as the HTT is reduced from 900° to 800°C.

The rates shown in Table 2 for the lignite char gasification are similar to data reported previously by other workers for CO_2 gasification of lignite chars prepared under similar conditions (5,6). Rates of wood char gasification indicate a substantially higher reactivity than reported previously for another lignocellulose-derived char gasified in CO_2 at 900°C (7). The lignite char was nearly twice as reactive as the wood char over the temperature range studied, which is no doubt due in part to its higher ash content. The lower reactivity of the wood char is also explained in part by the CP/MAS ^{13}C n.m.r. spectrum of the char prepared by 10 minutes pyrolysis at 600°C, shown in Figure 3. This spectrum contains a single peak centered at 130 ppm, corresponding to aromatic carbon. The spectrum is nearly identical to that of an anthracite coal (8), and anthracite coals have been shown to be more than ten times less reactive than lignite under gasification by CO_2 (5). Wood chars prepared at higher temperatures contained insufficient hydrogen to provide for transfer of spin polarization to carbon, as required in the cross-polarization n.m.r. technique, and they did not give well-resolved spectra. However, it is clear that chars prepared above 600°C are highly aromatic and their gasification will require effective catalysis if it is to be carried out at lower temperatures. These n.m.r. data are somewhat surprising in view of earlier work on the n.m.r. spectroscopy of wood chars which showed a significant aliphatic component in chars prepared at temperatures up to 400°C (9).

The char yields and reactivities of chars (HTT 800°C) prepared from untreated cottonwood and catalyst-treated samples are shown in Table 3. The catalysts were added by ion exchange to the acid-washed sapwood as described earlier. Acid washing had a dramatic effect on the char yield, reducing it by a factor of more than two. Addition of transition metal and alkaline earth metal catalysts had little effect on the char yield, but the alkali metal catalysts restored the char yield to near the level found for the untreated wood. Acid-washing also resulted in complete loss of the cellular structure of the wood during pyrolysis. All of these effects parallel those reported previously for the effects of inorganic species on the carbonization of the cottonwood (10).

Table 3. Ash content and char yields (HTT 800°C) of untreated and ion-exchanged cottonwood samples and extents of conversion due to pyrolysis (P) and gasification (G) of cottonwood chars gasified for 30 minutes at 800°C in 90.9 kPa CO_2.

Sample	Ash Content (%, d.a.f.)	Char Yield (%, d.a.f.)	Percent Conversion P	G	Total
Cottonwood Heartwood					
Untreated	2.01	16.8	(100% in <20 min)		
Cottonwood Sapwood					
Untreated	0.51	14.8	2	40	42
Acid-washed	<0.02	7.1	2	<1	2
Na^{+}-exchanged	0.31	14.0	4	16	20
K^{+}-exchanged	0.40	13.9	2	13	15
Mg^{+2}-exchanged	0.17	9.4	3	15	18
Ca^{+2}-exchanged	0.34	9.7	5	102	107[a]
Co^{+2}-exchanged	0.33	9.5	9	73	82
Ni^{+2}-exchanged	0.32	8.0	3	34	37
Cu^{+2}-exchanged	0.40	7.3	1	3	4

[a]Percent of conversion determined by integration of combustible gas detector signal was consistently 100-110% of weight of samples which gasified completely.

The most reactive sample was found to be the untreated cottonwood heartwood. The reactivity of this char reflects its higher ash content, and further illustrates the catalytic properties found previously for the natural inorganic fraction (2). The most effective ion-exchanged catalysts were found to be calcium and cobalt, which gave reactivities intermediate between the untreated sapwood and heartwood samples. Chars containing alkali metal catalysts were supprisingly unreactive in view of the excellent catalytic properties of these catalysts for lignite chars gasified in steam (4) and in air (11). Alkali metals are known to be lost during pyrolysis and gasification at these temperatures (12), but the char from potassium-treated wood contained 2.3% of ash by TG, suggesting that a large proportion of the catalyst was retained, at least during char formation.

The catalytic activities of the alkaline earth metals in wood gasification more closely parallel effects reported in the CO_2 gasification of coal char (5). The high catalytic activity of calcium suggests that it is the dominant factor controlling the reactivity of the untreated cottonwood sapwood and heartwood samples (see metals analysis in Table 1).

The transition metals are known to be active catalysts of CO_2 gasification, although they are often deactivated by oxidation during reaction (13). We have previously found this to be the case in the CO_2 gasification of wood chars (HTT 1000°) as well (2). The wide range of reactivities shown in Table 3 for the gasification of wood chars catalyzed by transition metals could, therefore,

represent the inherent activity of the catalyst or the activity of the catalyst under these specific conditions of pyrolysis and gasification. However, the high catalytic activity of the cobalt indicates the potential utility of these catalysts, and we are continuing to investigate the effects of pyrolysis and gasification conditions on catalysis of wood char gasification by cobalt.

The effects of different catalyst treatments are further illustrated by the reaction rate profiles shown in Figures 4-6. Figure 4 shows the rate of CO_2 gasification of char prepared from K^+-exchanged wood. The rate is nearly constant throughout the reaction, suggesting that the reaction is zero order with respect to the mass of the char. The reaction does not appear to undergo the initial induction period which is often observed in gasification reactions. By contrast, Figure 5 shows that the gasification of the char containing calcium does exhibit an induction period, and the rate decays in a more nearly first order manner following the induction period. The char was completely gasified in this case. A third type of behavior is exhibited in catalysis by cobalt, as shown in Figure 6. In this case the reaction is very rapid at the outset and decays more rapidly than would be expected for a reaction which is first order with respect to the char. The rate approaches zero well before the char is depleted, indicating that the catalyst is being deactivated during reaction, and that a very high level of catalysis could be attained if this deactivation could be avoided.

We have also determined the rates of gasification of chars prepared from wood treated beyond the exchange capacity with the acetate salts of potassium, cobalt and calcium. Gasification rates of these chars are compared to those of the chars from ion-exchanged wood in Figure 7. In all three treatments the reactivity increased at least linearly with the quantity of added catalyst. This implies that the catalyst dispersion afforded by ion exchange is lost during carbonization, or that the catalyst added as the aqueous salt solution was equally well dispersed, presumably on the hydrophilic carbohydrate portions of the wood cell wall.

Loss of dispersion of ion-exchanged catalysts has been conclusively demonstrated in calcium-exchanged coals heated at 1000°C (14). Although the temperatures employed in the current study were somewhat lower, it is possible the same processes occur, and the potential advantage of the ion-exchanged catalyst is lost due to catalyst agglomeration. If this is the case, the relative effectiveness of the ion-exchanged catalyst should be enhanced by reducing the carbonization temperatures, and studies now underway should provide additional information on the nature of these processes.

The most surprising feature of Figure 7 is the dramatic increase in reactivity of chars prepared from wood treated beyond the ion exchange capacity with cobalt acetate. This sample was so reactive that the reaction rate at 800°C could not be accurately measured in our system. The two cobalt-treated chars (HTT 800°C) were therefore gasified at 600°C with similar results, as indicated by the dotted line in Figure 7. It is difficult to envision a mechanism whereby the acetate salt would be a more effective catalyst than ion-exchanged carboxylate salts. It is possible that the two forms of the catalyst decompose to different products, which could have different catalytic activities, although it is not clear at this time what these forms might be. In any case, the catalytic efficiency of the higher level of cobalt treatment is very promising. The reactivity at 600°C is much higher than that found previously for CO_2 gasification at 650°C of wood chars treated with even higher levels of iron and nickel salts (2), and it appears to be less subject to deactivation during gasification. Cobalt has previously been studied with respect to its effects on CO_2 gasification of graphite (13) and a highly carbonized cellulose char (HTT 1000°C) (15). In each case it was found to be similar in effectiveness to nickel and iron catalysts. The results reported here indicate a unique catalytic capacity for cobalt, which may also indicate unique properties of wood chars formed in the temperature range employed in this study.

ACKNOWLEDGEMENT

This work was supported by the Gas Research Institute under Grant No. 5082-260-0683. The CP/MAS ^{13}C n.m.r. spectrum was provided by the Colorado State University Regional NMR Center, funded by National Science Foundation Grant No. CHE-8208821. The lignite sample and analysis was provided by the Penn State Coal Data Base.

REFERENCES

1. R.A. Susott, W.F. DeGroot and F. Shafizadeh, J. Fire Flamm., 6 (1975) 311.

2. W.F. DeGroot and F. Shafizadeh, Fuel, 63 (1984) 210.

3. W.F. DeGroot, Carbohydr. Res., 142 (1985) 172.

4. E.J. Hippo, R.G. Jenkins and P.L. Walker, Jr., Fuel, 58 (1979) 338.

5. E.J. Hippo and P.L. Walker, Jr., Fuel, 54 (1975) 245.

6. L.R. Radovic, K. Steczko, P.L. Walker, Jr. and R.G. Jenkins, Fuel Processing Technology, 10 (1985) 311.

7. D.M. Mackay and P.V. Roberts, Carbon, 58 (1982) 105.

8. G.E. Maciel, V.J. Bartuska and F. Miknis, Fuel, 58 (1979) 391.

9. Y. Sekiguchi, J.S. Frye and F. Shafizadeh, J. Appl. Polym. Sci., 28 (1983) 3513.

10. W.F. DeGroot and F. Shafizadeh, J. Anal. and Appl. Pyr., 6 (1984) 217.

11. L.R. Radovic, P.L. Walker, Jr. and R.G. Jenkins, Fuel, 63 (1984) 1028.

12. D.A. Sams, T. Talverdian and F. Shadman, Fuel, 64 (1985) 1208.

13. P.L. Walker, Jr., M. Shelef and R.A. Anderson in Chemistry and Physics of Carbon, Vol 4 (P.L. Walker, Jr. ed.), Marcel Dekker, New York, 1968, pp. 287-383.

14. L.R. Radovic, P.L. Walker, Jr. and R.G. Jenkins, Fuel, 62 (1983) 209.

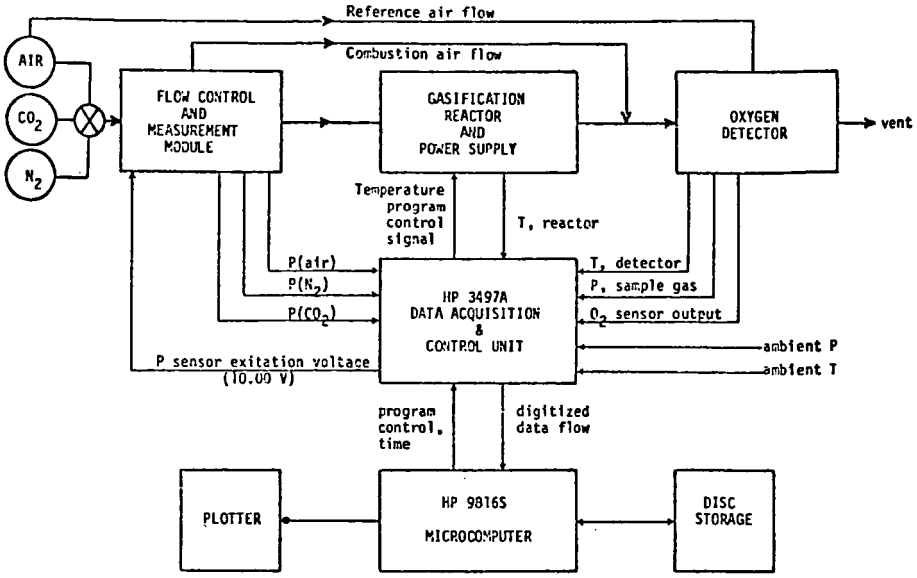

Figure 1. Schematic diagram of gasification reactor and combustible gas detector system.

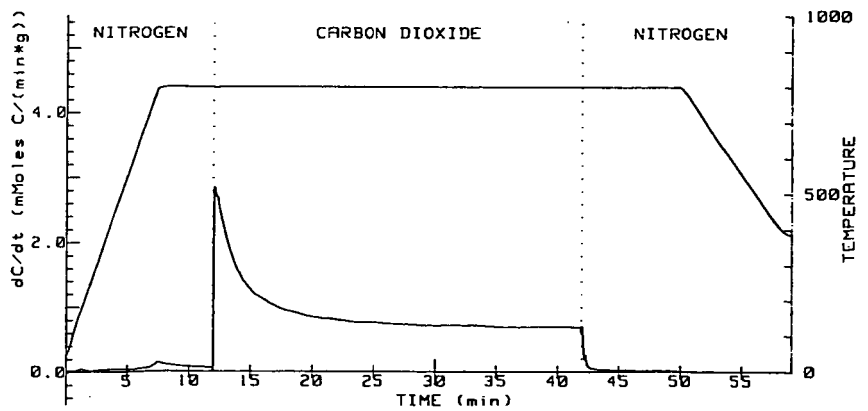

Figure 2. Reaction rate profile for the gasification of untreated cottonwood char in 90.9 kPa CO_2 at 800°C.

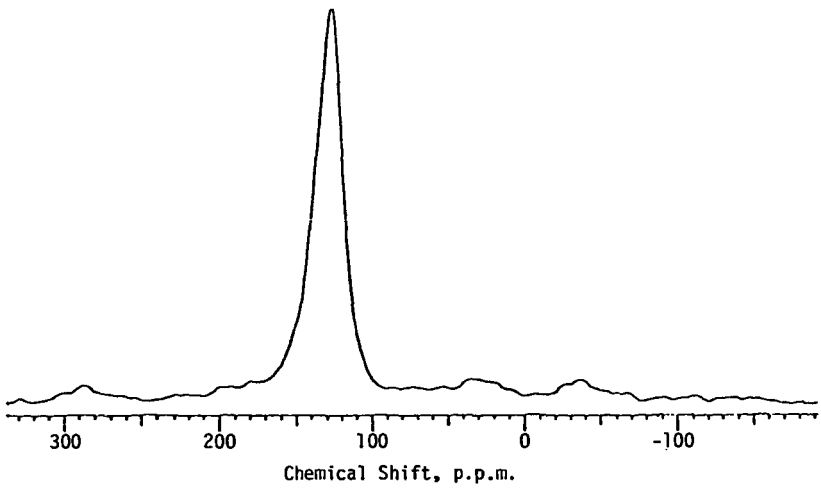

Figure 3. CP/MAS ^{13}C n.m.r. spectrum of char prepared from untreated cellulose (HTT 600°C).

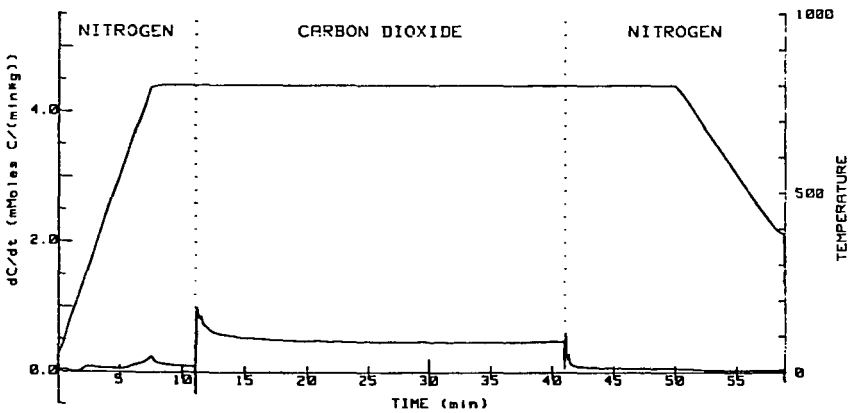

Figure 4. Reaction rate profile for the CO_2 gasification of char (HTT 800°C) prepared from K^+-exchanged cottonwood.

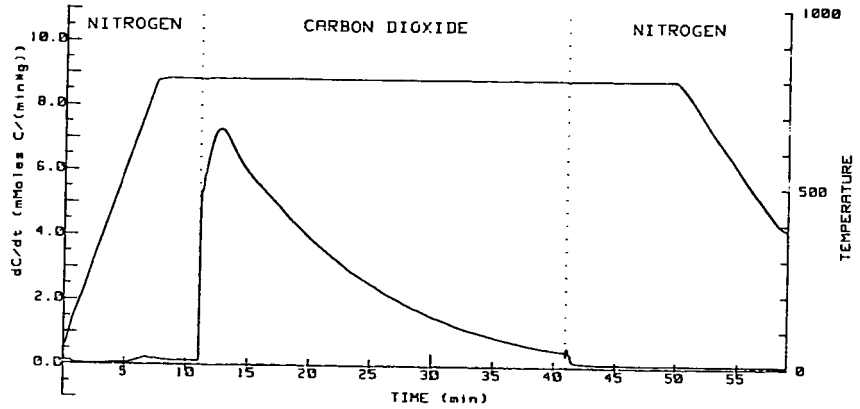

Figure 5. Reaction rate profile for the CO_2 gasification of char (HTT 800°C) prepared from Ca^{+2}-exchanged cottonwood.

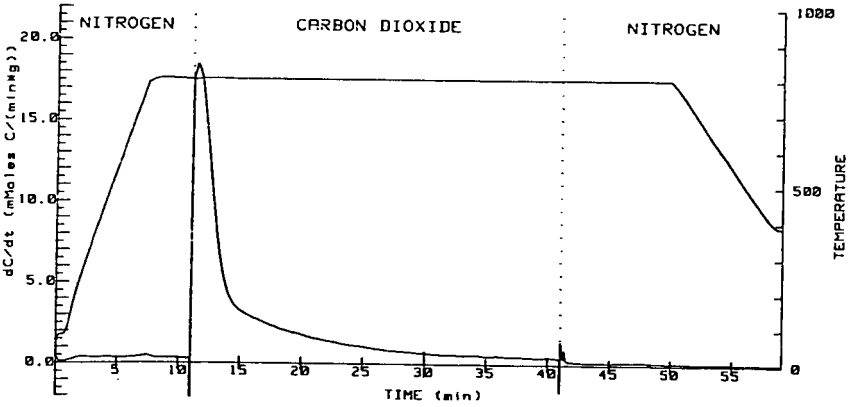

Figure 6. Reaction rate profile for the CO_2 gasification of char (HTT 800°C) prepared from Co^{+2}-exchanged cottonwood.

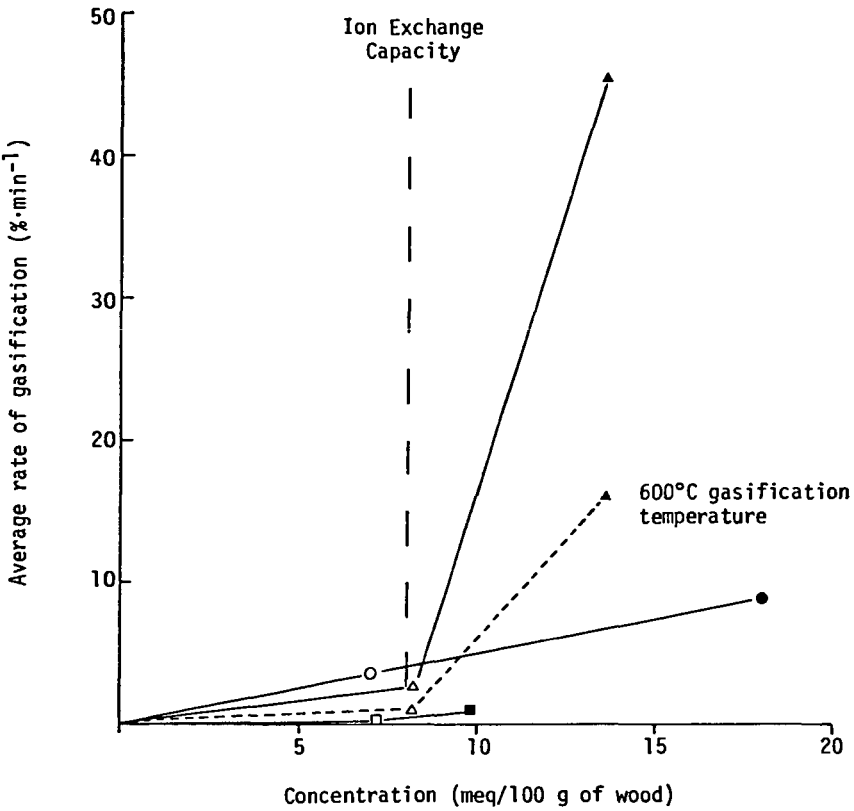

Figure 7. Average rate of CO_2 gasification at 800°C of chars prepared from cottonwood treated with inorganic catalysts at the ion exchange capacity (open symbols) and beyond the ion exchange capacity (solid symbols): potassium (□,■); cobalt (△,▲); calcium (○,●).

OXYGEN-ENRICHED COMBUSTION OF A COAL-WATER FUEL

by

Timothy S. McIlvried, Alan W. Scaroni, and Robert G. Jenkins

Fuel Science Program
Department of Material Science and Engineering
The Pennsylvania State University
University Park, PA 16802

INTRODUCTION

Several successful test firings have been performed with coal-water fuels (CWF's) in industrial boilers. However, even with advances in atomization and burner design, there are still inherent limitations associated with CWF's which cause decreased combustor performance. These include:

1) Temperatures and heat liberation from CWF flames are lower than those of oil flames. This is due, mainly, to the high water concentrations, which must be vaporized.
2) Successful ignition and flame stabilization of CWF's usually require high primary air preheat temperatures and/or a pilot flame.
3) Ignition delay and burnout times of CWF droplets are longer than those of oil droplets. The residence time of CWF droplets in oil fired boilers is usually not sufficient for complete carbon burnout. Thus, the CWF firing rate must be reduced, resulting in a derating of the boiler.

One means of overcoming, or at least reducing, the combustion problems associated with CWF's is oxygen enrichment of the combustion air. Moderate amounts of oxygen enrichment, usually between 1-4 volume percent, have been used in industry to either boost production levels or improve combustion efficiency in pulverized coal and oil fired boilers (1). Oxygen enrichment increases the partial pressure of oxygen leading to acceleration of the combustion rate and, thus, the rate of char burnout of the CWF droplets. Correspondingly, there is a decrease in the total

amount of nitrogen in the combustion air, which reduces the volume of the air and flue gases. This in turn, causes an incressed residence time of the CWF droplets because of lower gas velocities. Both increased combustion rate and longer residence time will help offset some of the derating associated with converting to CWF's. This study is aimed at determining the effect that a 2% increase in the oxygen content of the primary combustion air will have on the combustion characteristics of a CWF.

EXPERIMENTAL

A horizontally fired laboratory scale combustor, designed and built at Penn State to fire fuel oil, was modified to fire CWF's (2,3). Using this combustor, the effect of enriching the oxygen content of the primary air on the heat distribution in the furnace, the quantity of unburned carbon in the flyash and pollutant formation (NO_x and SO_2) were investigated.

The CWF used was supplied by The Atlantic Research Corporation, Fredericksburg, Virginia. Analyses of the CWF and parent coal are given in Table 1. The origin of

TABLE 1
ANALYSES OF THE CWF

	AS RECEIVED (wt%)	DRY BASIS (wt%)
C	57.4	80.8
H	3.4	4.8
N	1.1	1.6
S	0.5	0.7
O (by difference)	4.3	6.0
ASH	4.3	6.1
H20	28.9	-

Higher Heating Value 2.44×10^7 J/kg (10,500 BTU/lb)

PROXIMATE ANALYSIS (DRY BASIS)

VM	ASH	FIXED CARBON
30.9%	6.1%	63.0%

the parent coal is unknown but the analyses are typical of a high volatile eastern bituminous coal. The CWF has a solids loading of 70 wt% and a higher heating value of 2.44×10^7 J/kg (10,500 BTU/lb). Thus, the CWF is typical of many of those that are currently under consideration by industry. The furnace was operated at a firing rate of 48 kW (164,000 BTU/lb). Oxygen enrichment was achieved by combining a stream of pure oxygen with the combustion air in order to increase the oxygen content to the desired 23% concentration. The oxygen/fuel ratio was varied from 95% to 115% theoretical oxygen. Centerline furnace temperatures were measured at various axial distances along the combustor using shielded thermocouples. Stack gases were continuously monitored for O_2, CO_2, CO, NO_x, and SO_2. Flyash samples were analyzed for carbon content.

Furnace preheat and CWF ignition were achieved by a methane pilot flame. It should be noted that stable CWF flames were not able to be maintained without pilot flame support. Thus, the methane pilot flame was maintained during all trials and provided approximately 25% of the total heat input to the combustor.

RESULTS

Combustion trials were performed on the CWF with normal air and air enriched to 23% oxygen (2% oxygen enrichment). A 2% increase in oxygen content of the primary combustion air provided an 8.7% decrease in the volume of combustion air required and a 7.9% decrease in the volume of flue gases produced. Figure 1 shows higher furnace temperatures for the oxygen enriched case. There was approximately a 60 K increase at 5% excess oxygen. This increase in temperature appears to be quite constant over the length of the combustor. The amount of carbon in the flyash was reduced by about 5% at this excess oxygen level. The oxygen enriched flames also appeared visually brighter and closer to the burner (i.e. a shorter ignition delay).

Sulfur oxides are formed when sulfur in the fuel is oxidized during the combustion process. Figure 2 shows SO_2 emissions as a function of excess air (normalized to a 0% excess air basis and taking into account the reduced volume of flue gas in the oxygen enriched cases). It was found that SO_2 concentrations were

virtually independent of amount of excess air or oxygen enrichment for the fuel lean flames. However, the SO_2 concentrations appear to be increased for the oxygen enriched fuel rich flame.

As is well known, NO_x is formed in two ways during combustion; that is by oxidation of atmospheric nitrogen (thermal NO_x) and oxidation of nitrogen in the fuel (fuel NO_x). The formation of thermal NO_x is very temperature dependent and is not considered to be a significant source of NO_x formation at temperatures below about 1770 K (4). The maximum temperature reached in the experimental combustor was about 1450 K therefore, most of the NO_x was assumed to be fuel NO_x. Figure 3 shows the variation of NO_x with percent excess air for both the normal and oxygen enriched combustion. NO_x concentrations were approximately 70 PPM higher in the fuel lean oxygen enriched flames. As the flames become more fuel rich the NO_x concentrations in the oxygen enriched flames somewhat approach the concentrations found in the ambient air flames.

CONCLUSIONS

Oxygen enriched combustion of a CWF was studied in a small scale (48 kW) combustor. It was found that a 2% increase in oxygen content of the combustion air produced:

1) Increase of about 60 K in furnsce temperature.
2) More luminous flame with shorter ignition delay.
3) Approximately a 5% reduction of carbon in the flyash
4) No effect on SO_2 formation in fuel lean flames.
5) Somewhat higher NO_x emissions for fuel lean flames but only slightly higher NO_x concentrations for fuel rich flames.

ACKNOWLEDGEMENTS

Financial support for this research was provided by the Penn State coal-water fuel project funded by the Commonwealth of Pennsylvania. The coal-water fuel was provided by the Atlantic Research Corporation.

REFERENCES

1. Taschler, D.R., Nolte, F.S., Stringfello, T.E., The Impact of Oxygen Enriched Combustion of Coal Water Slurries on the Economics and Performance of Large Scale Boilers, Sixth International Symposium on Coal Slurry Combustion and Technology, Orlando, Florida, June 1984

2. Lima, J.G.H., Effect of Oxygen Enrichment on NO_x from Distillate Petroleum Flames in a 25 Kilowatt Combustor, M.S. Thesis, The Pennsylvania State University, 1983

3. Rodriguez-Pereira, R., Effect of an Atomizing Medium on Coal-Water Mixture Combustion, M.S. Thesis, The Pennsylvania State University, 1985

4. Morrison, G.F., Nitrogen Oxides from Coal Combustion - Abatement and Control, IEA Coal Research Report Number ICTIS/TR 11, November 1980

5. Wagner, J., Sommer, T.M., Taylor, B.E., Johnson, S.A., Coal-Water Mixture Firing in an Industrial Package Boiler - A Users Perspective, Seventh International Symposium on Coal Slurry Fuels Preparation and Utiliization, New Orleans, Louisiana, May 1985

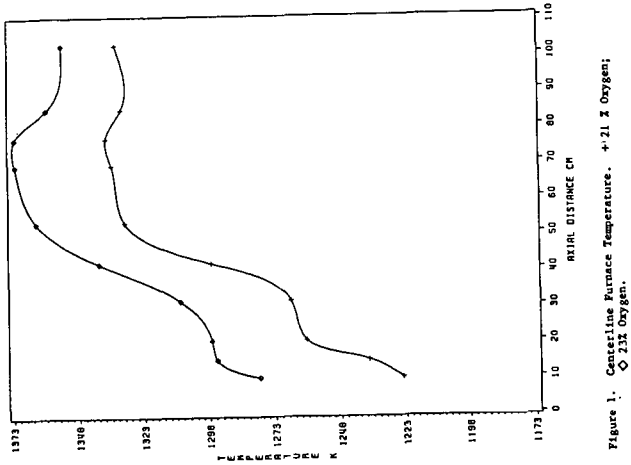

Figure 1. Centerline Furnace Temperature. + 21 % Oxygen; ◇ 23% Oxygen.

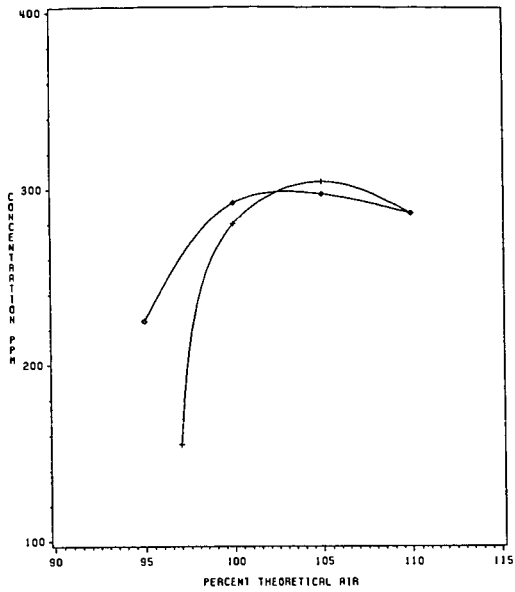

Figure 2. Sulfur Dioxide Concentration Versus Percent Theoretical Air on an Oxygen Free Basis. + 21% Oxygen; ◇ 23% Oxygen.

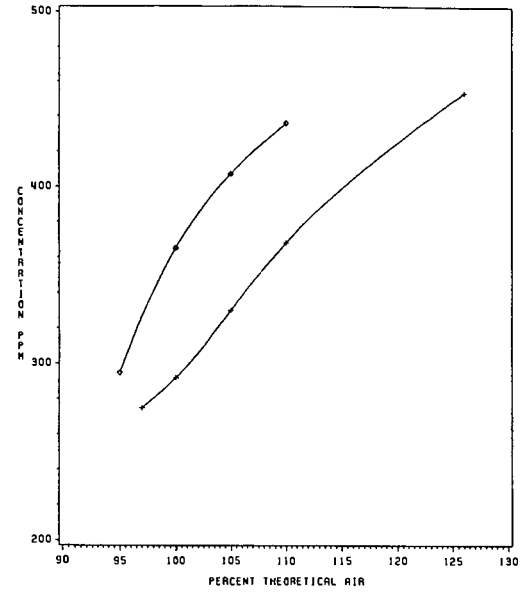

Figure 3. NO_x Concentration Versus Percent Theoretical Air on an Oxygen Free Basis. + 21% Oxygen; ◇ 23% Oxygen.

Secondary Atomization of Coal-Water Fuel Droplets Resulting from Exposure to Intense Radiant Heating Environments

Daniel J. Maloney and James F. Spann (ORAU)

U.S. DOE, Morgantown Energy Technology Center
P.O. Box 880, Morgantown, WV 26505

Introduction

The use of coal-water fuels (CWF) for direct firing in heat engines presents some challenges because conventional turbine combustors and diesel engines require short duration, intense combustion processes. It is generally understood that burning times required for efficient carbon utilization in these systems is a function of the fuel droplet size. For CWF droplets, the early stages of heating are critical. Under certain heating conditions, water is evaporated from a droplet leaving a relatively slow burning agglomerate of coal particles. Under other heating conditions, however, fuel droplets may boil explosively producing many small fragments having characteristically shorter combustion times. The behavior of CWF in a combustor depends on a number of factors including droplet size, the amount and size distribution of coal particle inclusions, and the primary mode and rate of droplet heating. A detailed knowledge of slurry droplet evaporation mechanisms is required, therefore, for accurate prediction of slurry droplet combustion times and for the design of CWF-fired heat engines.

The objective of this work is to determine the radiant energy flux conditions required to achieve explosive boiling of CWF droplets. Radiant heating is important because, when considering coal particle sizes typical of highly beneficiated micronized CWF (2 to 3 microns mean radius) proposed for use in heat engine applications, the black body radiation prevalent in combustion environments can penetrate into the droplet. The resulting internal heating of coal particles can result in superheating of the water within the droplet and thereby establish conditions necessary for explosive boiling.

Experimentally, conditions required to achieve explosive boiling were determined by electrodynamically suspending and irradiating single CWF droplets with well characterized radiation pulses. Droplet behavior in these experiments was monitored using high-speed cinematography. The energy flux required for explosive boiling was determined at ambient temperature and pressure as a function of incident radiation intensity and CWF droplet size and composition. The results were then compared with theoretical predictions of the explosive boiling threshold for CWF droplets in high-temperature black body radiation fields. The primary question we wish to address is: do sufficient conditions exist, or can they be made to exist, to cause explosive boiling of CWF droplets ranging from 20 to 200 microns in diameter in realistic combustor configurations?

Experimental

Single CWF droplets were isolated and held in an electrodynamic balance apparatus which was designed and fabricated based on the work of Davis and Ray (1). The balance, as illustrated in Figure 1, is a quadrupole trap consisting of two hyperboloidal endcap electrodes and a central ring electrode. When an AC voltage is applied between the ring and the two endcap electrodes the resulting field has a well defined null point at the geometric center of the balance. A charged droplet in the electric field is subject to a time averaged force directed toward the null point. The droplet is held at the null point by

applying a DC field across the endcap electrodes to counterbalance gravitational forces.

CWF droplets are delivered to the balance chamber from a CWF droplet generator developed specifically for use in these experiments. The basic device consists of a cylindrical piezoelectric transducer element with a capillary tube attached to one end and a fuel supply line attached to the other. The operating principle is the same as that used in ink-jet printers. Voltage pulses applied to the transducer cause sudden volume contractions which force fuel through the capillary orifice. The extruded fuel forms a monodisperse stream of droplets of uniform composition with the droplet size being determined by the capillary diameter and by the amplitude and duration of the voltage pulses. Details of the design and operating characteristics of the CWF droplet generator are provided elsewhere (2). Droplets are inductively charged by passing the droplet stream through an orifice in a charged plate prior to delivery into the electrodynamic balance chamber.

The droplet mass to charge ratio (m/q) is directly proportional to the DC voltage required to bring the droplet to the null point. For CWF droplets the mass (and so m/q) is continuously changing due to water evaporation and the balance voltage must be adjusted to hold the droplet at the null point during an experiment. To facilitate droplet position control and to provide accurate and precise measurements of changes in droplet size and mass, a microprocessor controlled, droplet imaging system (DIS) was developed. The DIS utilizes a Vidicon (video camera) detector to monitor droplet position and size. A microprocessor scans the vidicon every 17 ms and image processing techniques are employed to determine the droplet location and size. A control signal is then generated to maintain droplet position at the balance null point. Digital values corresponding to droplet cross-sectional area and balancing voltage (proportional to droplet mass) are generated at a rate of 60 Hz. The droplet size information is used to trigger the high-speed camera and to activate the pulsed radiation (laser) source. In addition, droplet diameter, mass and composition (percent coal by mass) are determined from the droplet size and balance control data. Figure 2 illustrates the capabilities of the DIS for droplet size and mass determination. The data shows the strong dependence of the droplet mass with changing droplet radius. Since droplet density increases as water evaporates from the CWF, the droplet mass dependence deviates slightly from the r^3 relationship expected for a constant density droplet. The confidence interval (95 percent) for droplet size resolution with the DIS is $\pm$ 3 microns for droplets ranging in diameter from 50 to 200 microns. The confidence interval for mass resolution is $\pm$ 50 nanograms.

The CWF used in these experiments was a physically beneficiated (3 percent ash) micronized (3 micron mean particle radius) slurry having a composition of 62 percent coal by mass. During a typical experiment a water or dilute CWF (1 to 20 percent coal by mass) droplet was delivered to the balance chamber. The droplet size and weight were monitored by the DIS until a preselected size was attained. The high-speed movie camera was then activated and the laser was pulsed. A schematic of the experimental configuration is provided in Figure 3.

CWF droplets delivered to the balance chamber were on the order of 250 microns in diameter. Droplet size and composition were controlled by changing the initial coal composition in the droplet and by carefully monitoring the water evaporation. In this manner droplet sizes (50 to 200 microns in diameter) and compositions (50 to 70 percent coal by mass) of interest for combustion applications could be easily accessed.

Results

Experiments were conducted using an eximer laser (wavelength 0.248 microns) to determine explosive boiling thresholds for water and CWF droplets at radiation pulse times of 10 nanoseconds. The test variables included droplet size and composition and radiation intensity. Single droplets of water and CWF (25 and 50 percent coal by mass) with radii of 25, 50, and 75 microns were irradiated from two sides (see Figure 3). The geometric cross section of the droplets then was twice πr^2 and the incident radiation intensity was varied from 2.5×10^7 W/cm^2 to 5×10^8 W/cm^2 by defocussing the laser beam. At the most intense radiant heating conditions the beam cross section was larger than 300 microns so that in all cases the droplets were completely blanketed by the incident radiation.

The results of experiments performed on CWF droplets containing 50 percent coal by mass are presented in Figure 4. The results can best be described in the context of Figure 5. Over the range of conditions employed CWF droplet behavior varied from oscillatory distortions to violent fragmentation as the radiant intensity was increased. The onset of fragmentation occurred over a narrow range of intensities from about 5×10^7 to 1.5×10^8 W/cm^2 . Figure 5 shows high speed film records for 75 micron radius droplets containing 50 percent coal by mass. The framing rate was 5,000 frames per second. Figure 5A illustrates the oscillatory behavior observed for these droplets when irradiated at an intensity of 2.5×10^7 W/cm^2. At this radiant intensity no droplet fragmentation was observed. Lower radiation intensities resulted in no observable fragmentation or oscillation. When the radiant intensity was increased to 5×10^7 W/cm^2 (Figure 5B) droplet fragmentation was observed. The first frame in sequence 5B shows the CWF droplet prior to initiation of the radiation pulse. The second frame of the sequence shows the droplet 0.2 ms later, after the laser pulse. The droplet appears to be a large prolated sphere suggesting the possible growth of vapor bubbles within the droplet. However, the time resolution available was not sufficient to conclusively show the existence of vapor bubbles. The third frame in the sequence shows the collapse of the prolated sphere and the formation of fuel "ligaments" attached to a central droplet core. This is followed by the breakup of the droplet to form three fragments. At this radiant heating intensity we consistently observed the formation of one or two small satellite fragments and a larger core droplet. After breakup, the fragments moved with a minimum velocity of 1 m/s. Figure 5C illustrates that as the radiant intensity was increased to 1.2×10^8 W/cm^2 the fragmentation of the droplets was more violent resulting in the formation of many small fuel droplets having minimum velocities ranging from 0.5 to 2 m/s. At higher radiant intensities (Figure 5D), fragmentation was evident, however, droplet fragments had velocities in excess of 3 m/s and resolution of droplet fragments was poor.

Based on the different behavior evident in the high-speed film records modes of droplet behavior have been arbitrarily defined as: NF, no fragmentation of the droplets, F, fragmentation of the droplets to form a few relatively large droplet fragments, and EF, explosive fragmentation of the droplet to produce many small droplet fragments. Figure 4 summarizes the results of experiments using CWF droplets containing 50 percent coal by mass. The dashed line in the figure represents the theoretical predictions of Sitarski (3-5) for explosive boiling thresholds for CWF droplets exposed to high-temperature black body radiation. The theoretical predictions illustrated in Figure 4 have been modified to reflect the fact that the droplets were irradiated from two sides with a geometric cross section of $2 \pi r^2$. Figure 4 illustrates that explosive boiling thresholds decreased as droplet size was reduced. Experiments performed on droplets with 25 percent coal by mass showed a similar trend with decreasing

droplet size. Within the error of the experiment there was no observable difference between the behavior of CWF droplets as the coal loading was increased from 25 to 50 percent coal by mass. The presence of coal in the droplet did play an important role, however. Pure water droplets showed no evidence of oscillation or fragmentation at radiation fluxes of 5×10^8 W/cm^2 and below. This observation is consistent with the fact that pure water is essentially transparent to radiation at 0.248 micron wavelength.

Discussion

The theory developed by Sitarski (4) assumes that electromagnetic radiation is absorbed uniformly within the droplet causing strong superheating of the liquid at the center of the droplet where thermodynamic conditions approach those on the spinodal line. The sudden burst of vapor bubbles produced at the spinodal temperature then leads to disruption of the droplet. The experimental observations are consistent with this physical description of the explosive boiling phenomena and the agreement between the experimentally determined thresholds for explosive fragmentation are in excellent agreement with the explosive boiling thresholds predicted by Sitarski.

Two alternative mechanisms for droplet breakup were also considered. They were the effect of radiation pressure and the potential for significant ionization and plasma formation. Calculations were performed to evaluate the radiation pressure associated with the laser pulse. The momentum imparted to the droplet due to the light pressure was found to be two orders of magnitude lower than the observed momentum (determined from the velocity of the fragments). Therefore, the contribution due to radiation pressure was insignificant. At radiation intensities similar to those employed in the present study, plasma formation has been observed for aerosol particles in air (6, 7). The accompanying laser breakdown depends on a number of factors including, the radiation wavelength, intensity and pulse time and the optical properties and size of the aerosol particles. Plasma formation and growth is usually accompanied by a characteristic flash of light followed by an acoustic pressure pulse (shock wave) as the plasma cloud expands at a rate of 2 to 3 km/s. Over the range of radiant heating conditions reported in Figure 4 there were no observations supporting the formation of a plasma cloud. At radiation intensities above 10^9 W/cm^2, however, the characteristic signs of plasma formation were evident.

Conclusion

Capabilities have been developed to determine radiant intensities required to achieve explosive boiling (secondary atomization) of CWF droplets of well defined size and composition. The system has been used to determine explosive boiling thresholds for CWF droplets at short duration high intensity radiant heating conditions. The experimental results are both qualitatively and quantitatively in good agreement with theoretical predictions for explosive boiling thresholds. Attention has now been directed toward applying these techniques to make measurements of explosive boiling thresholds at radiation wavelengths in the infrared region of the energy spectrum with millisecond heating times to address conditions which are representative of combustion applications.

Acknowledgements

The efforts of G. E. Fasching and L. O. Lawson in the development of the DIS are gratefully acknowledged. Discussions with Dr. M. Sitarski have been stimulating and insightful and are gratefully appreciated. This work was funded out of the United States Department of Energy Advanced Research and Technology Development Program.

References

1. Davis, E. J., and A. K. Ray, J. Colloid and Interface Science, 75, 566-576, 1980.

2. Maloney, D. J., L. A. McCarthy, W. F. Lawson, G. E. Fasching, and K. H. Casleton, "Laboratory Coal-Water Fuel Droplet Generator," Sixth International Symposium on Coal Slurry Combustion and Technology, Orlando, Florida, June 25 to 27, 1984.

3. Sitarski M., "Thresholds for Explosive Evaporation of Water and Coal-Water Mixture Fine Droplets Exposed to High-Temperature Black Body Radiation," Proceedings of Condensed Papers, International Symposium-Workshop on "Particulate and Multi-Phase Processes," 16th Annual Meeting of the Fine Particle Society, Miami Beach, Florida, April 22 to 26, 1985.

4. Sitarski, M., "Modification of an Analytical Model Which Predicts the Effect of Radiative Heating on Two-Phase Aerosols," presented at the AR&TD Direct Utilization Contractors Meeting, Morgantown, West Virginia, August 13 to 15, 1985.

5. Sitarski, M., Private Communication, October, 1985.

6. Danilychev, V. A., and V. D. Zvorykin, JSLRDU 5(6), 647-758, 1984.

7. Akhtyrchenko Y. V., L. A. Vasil'ev, Y. P. Vysotskii, and V. N. Soshnikov, JSLRDU, 5(2), 233-236, 1984.

2A:11-18-85:dr:5a

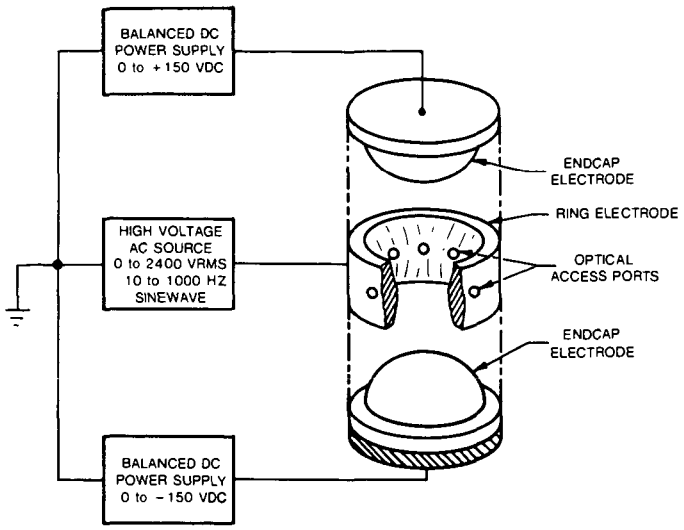

Figure 1. Electrodynamic Balance Apparatus

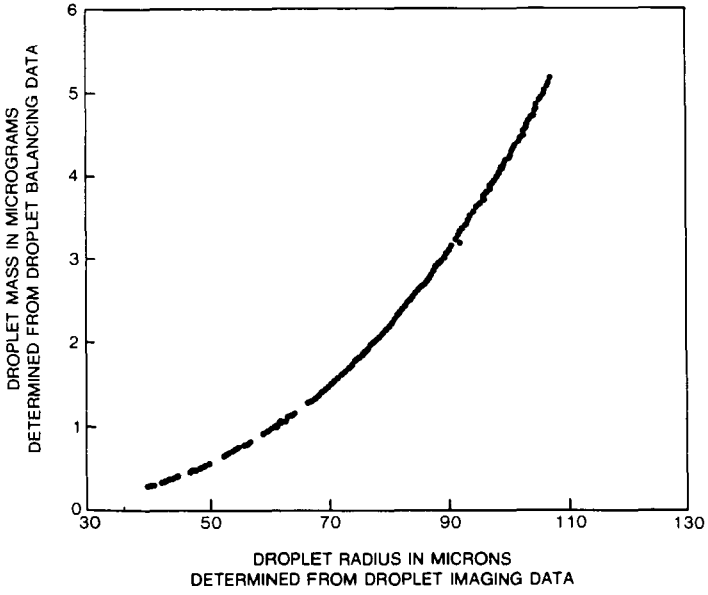

Figure 2. Droplet Mass and Size Resolution Capabilities for an Evaporating CWF Droplet

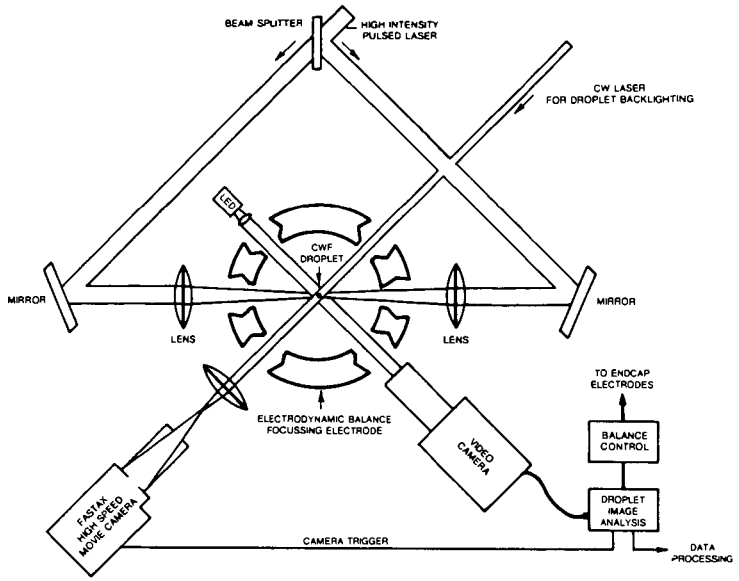

Figure 3. Experimental Configuration for Explosive Evaporation Studies

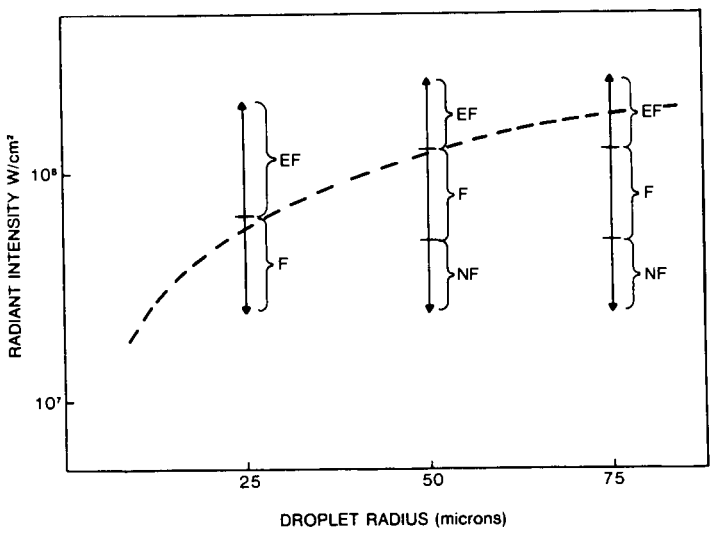

Figure 4. CWF Droplet Response as a Function of Radiant Heating Intensity at 10 ns Heating Time

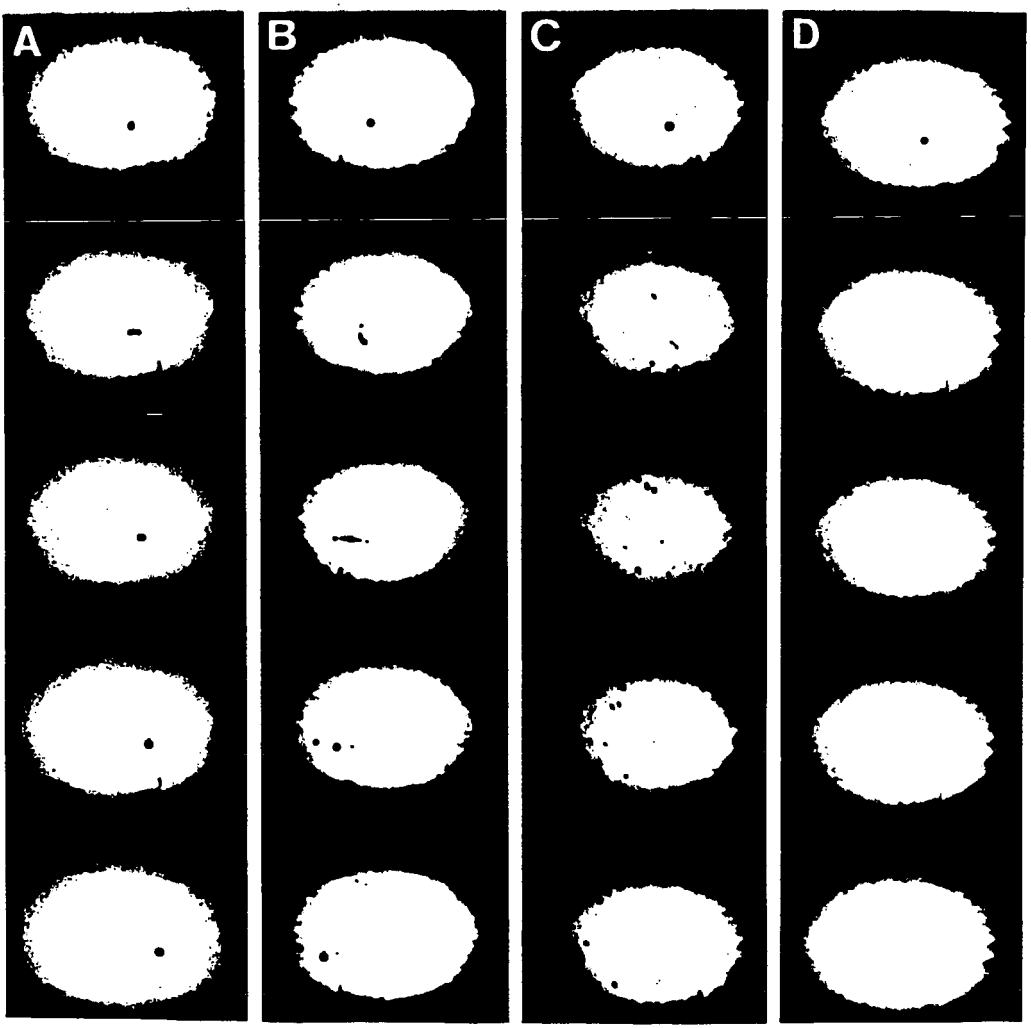

Figure 5. High-Speed Motion Picture Records of CWF Droplet Response to High-Intensity Radiant Heating. Radiant Intensity: A - 2.5 x 10^7 W/cm^2, B - 5 x 10^7 W/cm^2, C - 1.2 x 10^8 W/cm^2, D - 2.5 x 10^8 W/cm^2. Framing Rate of 5000 fps.

A BI-DIMENSIONAL OPTICALLY ACCESSIBLE F.B.C. FOR COAL COMBUSTION STUDIES

P.G. Lignola*, G. Raso**, N. Di Muro**, R. Parri*, M. Bader*

(*) - Dipartimento di Ingegneria Chimica - Università - 80125 Napoli
(**) - Istituto di Ricerche sulla Combustione - CNR - 80125 Napoli

INTRODUCTION

Bi-dimensional fluidized beds have been since long adopted for studying fundamentals of fluidization. Optical accessibility has been a valid tool for analysis of bubbles and their interaction, in spite of the existing behavioural difference between three and two dimension experiments. A bi-dimensional bed has been recently used for application of mass spectrometric analysis of gas concentration profiles in single bubbles rising through a bed kept at minimum fluidization velocity (1).

Coal combustion and gasification in fluidized bed is now actively and intensively studied. Models of coal combustion process, including volatilization have been proposed. However lack of optical access into traditional fluidized bed combustors, renders difficult the comparison between model prediction and experimental result.

The idea of developing a bi-dimensional combustor, fitted with mass spectrometric probe seemed very appealing, though of not easy design and construction.

In this paper design and construction of a bi-dimensional fluidized bed combustor (F.B.C.) and result of first experiments performed are reported.

F.B.C. DESIGN

Very crude and preliminary calculations show that it is not possible to operate steadily a bi-dimensional fluidized bed coal combustor normally exposed to ambient. Assuming for a quartz sand bed (70-600 μm size) a temperature of 1150-1200 K, radiant heat transfer reaches values of 80 kW/sqm, which cannot be carried by enthalpy of fluidizing gas. Generation of this substantial power is not possible by means of combustion itself, owing to the small amount of coal in the bed. Consequently it is necessary to feed the F.B.C. with extra power in order to obtain a steady operation. Hypothesis of adopting Vycor™ silica glass covered with thin tin oxide layer has been discarded, since its application at these temperatures are not known, neither it was possible to assess the semiconductivity properties at high temperature of tin oxide layer.

The obvious solution to the problem was to design a furnace, fitted with windows, in which the bed had to be enclosed. The furnace essentially consists of a parallelepipedic enclosure, the dimension of which are 1070 mm height, and 890 mmx1440 mm base. Starting from the inside, furnace walls are made of Triton Kaowall (TM), which is particularly suitable for high temperature, of Calsil (TM), which has good insulating properties and is asbestos free and, for the outer layer, of Monolux 500 (TM) which has good mechanical properties, but can stand lower temperatures. The bottom has been made of CER 21/M (TM) which presents good mechanical properties even at high temperature. Thickness of insulation has been calculated on the basis of following assumption: outer wall temperature <333 K, inner wall temperature equal to maximum operation temperature, linear temperature gradient through walls. Constant thermal conductivity for each material, averaged on temperature has been used in calculations. Front, rear and top walls are removable. Furnace top possesses a slot, which coincides with highest level of bed free-board and can be connected to an exhaust line. A square window, 250 mmx250 mm, made of polished Vycor (TM) glass as been made on front and rear panel. Windows are parallel to the bed and permit its optical observation. Four electrical resistances, each providing 3.6 kW, are immersed into a ceramic support, which is 50 mm thick, 300 mm wide and 600 mm high. These resistances give the necessary power to furnace, for every possible regime of operation, since several series and series-parallel insertions are possible. Calculations show that at steady state about 4 kW are necessary for keeping furnace at 1223 K. However resistances are

capable of producing 14.4 kW, which are useful for shortening apparatus start up.

A proportional, integral temperature controller has been designed which features a thyristor power unit, and safety set points which can be triggered by maximum and minimum temperature and which can be overridden during start up procedure. For safety reasons, thermocouple failure triggers the power off. Owing to large heat capacity of furnace and prevalent radiant heat transfer within enclosure, uniform temperature is achieved throughout the bed.

The bed is confined by means of two polished Vycor (TM) glass walls, 18 mm apart, inserted into slots created on furnace sides. The transparent walls are made of a double layer of sheets, 6 mm thick, 300 mm wide and 300 mm high. Owing to the limited size of Vycor (TM) sheets the two layers are skintled in order to prevent air and solid materials leakage during operation. Vycor (TM) glass walls continue up to the top of furnace, consequently free board is kept at the same temperature of the bed. Figure 1 shows the apparatus.

Even gas distribution at bottom of bed is achieved by means of a distributor made of aluminum silicate, which practically consists of a porous plate (140-200 μm pore size) 20 mm thick. Great care has been taken to seal the junction between distributor and bed. To this end a special Triton Kaowall(TM) cement has been used.

Flow of fluidizing gas is measured by means of conventional rotameter. Inlet gas pressure is measured by conventional open tube manometers. Temperature of bed is measured by means of thermocouple. On each side of the bed at different heightsthree channels have been drilled and fitted with 12 mm alumina tubes for coal feeding and gas sampling.

Arriflex cine camera, 16 mm, at 50frames per second has bees used for optical observation and recording of F.B.C. behaviour. Analysis of single frames has been carried out by means of a graphic tablet hooked to an Apple IIe(TM) personal computer. Bubble areas were evaluated by means of specific software. Time variation of dimension of coal and char particles was also analyzed by means of the same technique.

A continuous sampling CO_2 analyzer was also used for monitoring coal combustion.

The whole apparatus performed as expected. The bed could be kept steady at temperature of 1223 K as long as necessary.

RESULTS

To the best of authors' knowledge, the bi-dimensional F.B.C. is the first that has been ever constructed. Consequently it seems that up to now no direct optical test has been made yet on general fluidodynamics behaviour of fluid beds at high temperatures. Results reported in the following refer to a bed 260 mm wide and 140 mm high of sand (density 2.6 g/cm^3). Mass of solids was kept constant at 1 kg. The first set of experiments that has been run was aimed at assessing the possibility of testing these fundamental aspects of fluidization.

Minimum fluidization velocity U_{mf} has been experimentally evaluated for sand of two different sizes: 300÷400 μm and 850÷1000 μm. In fig. 2 U_{mf} values measured at experimental conditions are reported against temperature. For both sizes U_{mf} decreases with increasing temperature. Results are in accord with those obtained by Botterill and Teoman (2) and can be easily explained on the basis of viscosity increase with increasing temperature. Comparison with available theoretical models has not been fully accomplished yet, owing to the limited number of data. However first trials seem to indicate that for smaller size, available theory extrapolated at operation temperatures underestimate U_{mf}, whereas for larger size U_{mf} is nearly correctly estimated at temperatures lower than 673 K and is overestimated at higher temperatures.

Several films have been shot by means of cine camera with the aim of measuring bed expansion and bubble volume fraction at different temperatures. Results refer to bed of sand 300÷400 μm size. In fig. 3 bed voidage is reported against relative fluidization velocity U/U_{mf} for different bed temperatures. Bed voidage was evaluated by measuring on film frame bed height at different U/U_{mf}. Data show that bed voidage depends on temperature.

Experimental technique features the possibility of measuring bubble size on film frame by means of graphic tablet digitization. In fig. 4 an example of digitized frame is reported. Bubble fraction at different U/U_{mf} and temperatures have been measured by means of the above technique. Results are reported in fig. 5.

Combustion at 1123 K of batch of five particles of South African char, approximately spherical, of 130 mg mass and 6 mm diameter each, has been followed by cine camera recording and by monitoring CO_2 concentration in exhaust gases. Burn-out time has been determined by observation of particle disappearance and by CO_2 monitoring. Same experiment has also been performed with batch of three particles of South African coal, each of 400 mg mass and of 9 mm diameter. Data are reported in fig. 6. Cine camera was run at immission of particles into the bed and after 228 s and 552 s. In fig. 7 char particle diameter against time is reported as evaluated by the two methods. Data obtained by film frame analyses and data obtained by calculation of particle diameter reduction from CO_2 concentration measurement, to compare fairly well. On the same diagram theoretical variation of char particle diameter with time has been reported. Curve is drawn assuming shrinking particle model and diffusion control.

Combustion of a batch of three South Africal coal particles tested also apparatus capabilities of following devolatilization. Coal particles were spherical with 9 mm diameter and with a weight of 400 mg each. Devolatilization phase could be followed at ease and flamelets generated by gas combustion were observed.

CONCLUSIONS

The first results confirm that the apparatus that has been developed can be a powerful tool for studying high temperature processes in fluidized beds. Specifically fundamental fluidodynamics of beds can be investigated and combustion process of coal can be followed, even during devolatilization phase. Hypotheses of current models can also be checked, though with the limitation deriving from bi-dimensionality.

ACKNOWLEDGMENT

The work has been performed with partial financial support from Ministero della Pubblica Istruzione of Italy.

REFERENCES

1) Lignola P.G., Donsì G. and Massimilla L.: A.I.Ch.E. Symposium Series 79, 19 (1983)
2) Botterill J.S.M., Teoman Y.: in "Fluidization" ed. Grace J.R. and Matsen J.M., Plenum Press, N.Y. (1980), p. 93

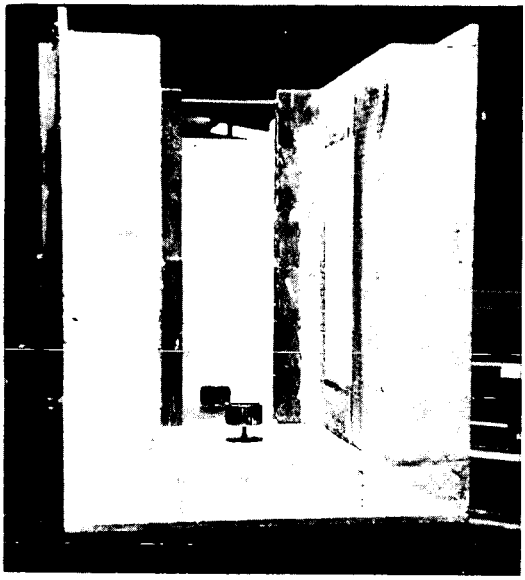

Fig. 1 - Furnace encloses F.B.C.

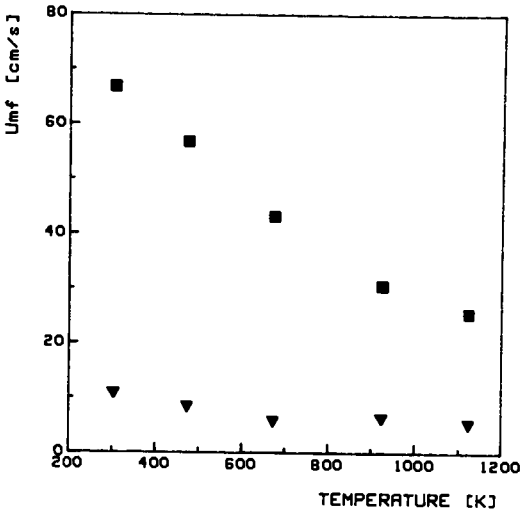

Fig. 2 - Minimum fluidization velocity vs temperature.
Bed solids: sand; ▼ 300 ÷ 400 μm; ■ 850 ÷ 1000 μm.

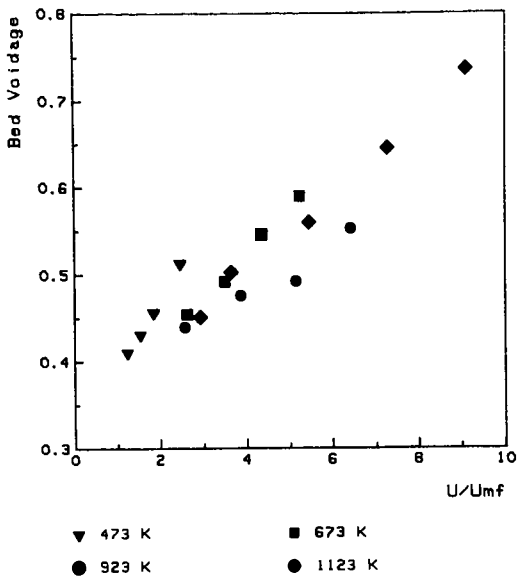

Fig. 3 - Bed voidage vs relative fluidization velocity for different temperatures. Bed solids: sand; 300 ÷ 400 μm.

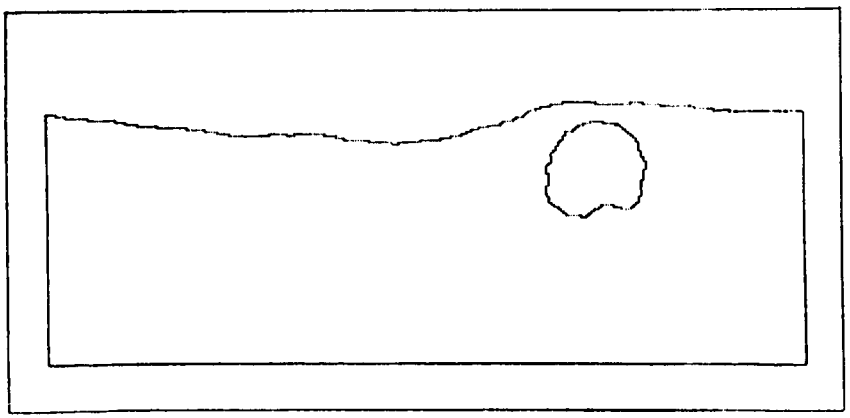

Fig. 4 - Example of digitized film frame showing a bubble rising thru the bed. Solid displacement caused by bubble ascent is evident. Bed solids: sand; 300 ÷ 400 μm; 1123 K.

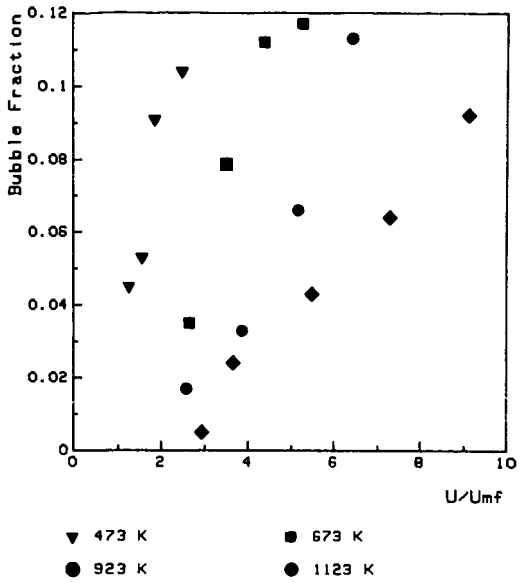

Fig. 5 - Bubble fraction vs relative fluidization velocity for different temperatures. Bed solids: sand; 300 ÷ 400 μm.

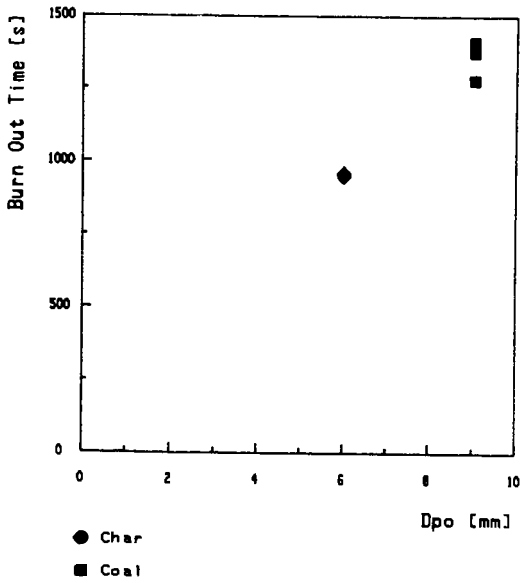

Fig. 6 - Burn out time vs particle diameter. Bed solids: sand; 300 ÷ 400 μm.

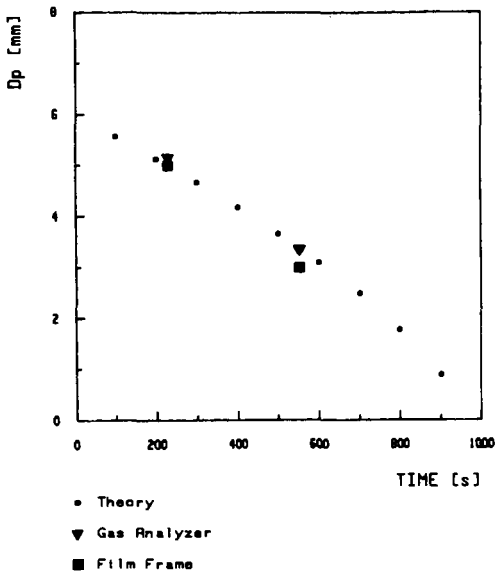

Fig. 7 - Reduction of char particle diameter vs time during combustion, as determined by film frame analysis and by treatment of the CO_2 analysis data. Bed solids: sand; 300 ÷ 400 μm; 1123 K.

Intra-Particle Sulfur Capture During Battelle Treated Coal Combustion Under Simulated Turbine Conditions

J. J. Reuther, H. N. Conkle, and H. F. Feldmann

BATTELLE
Columbus Division
505 King Avenue
Columbus, Ohio 43201

Introduction

For the last several years, Battelle Columbus Laboratories has been actively conducting research on the development of a practical, cost-effective process for improving both the fixed-bed gasification(1) and the boiler combustion(2) characteristics of high-sulfur, agglomerating, low-reactivity bituminous coal. The product of this research is a calcium-impregnated coal called Battelle Treated Coal (BTC), given the acronym BTC. The properties of BTC are much different from those of the raw coal from which it is processed(1,2). Specifically, these differences are:

- Increased ASTM volatile matter content.
- Higher char reactivity.
- Reduced tar formation tendency.
- Hotter ash fusion temperatures.
- Diminished coal particle agglomeration tendency.
- Enhanced sulfur retention by the ash.

As near-term markets for gasifier and boiler coal diminish or stabilize, respectively, Battelle has expanded the search for other old or new applications for bituminous coal that would also benefit from the alterations that could be given it by the Battelle calcium impregnation process. Recent planning studies by the United States Department of Energy (U.S. DOE) have forecast a need for coal-fired combustion turbines for the repowering of electric utilities when they become capacity-limited or deficient in the early-to-mid 1990s(3). The purpose of the program reported here is to demonstrate the promise of utilizing BTC as a fuel in advanced, coal-capable combustion turbines.

This paper is the second(4) in a series to present the results of a U.S. DOE-sponsored program designed to determine the intra-particle sulfur capture efficiency of BTC under simulated combustion turbine conditions. The BTC consisted of either of two high-sulfur (>4 percent by weight) Illinois No. 6 coals that had been impregnated with calcium-containing catalysts using a proprietary Battelle process. The simulated turbine combustion conditions consisted of super-atmospheric pressure, ultra-high excess air levels, average firing temperatures, and near-quantitative carbon conversion. Combustion test results reported here will focus on the parametric and comparative effects of raw coal organic sulfur content, calcium source, and calcium impregnation technique on sulfur capture efficiency. The effects of pressure and temperature on sulfur capture efficiency, as well as on ignition, burnout, and ash deposition, were the subjects of the earlier report(4).

Experimental

A coal-fired combustion turbine simulator was constructed at Battelle by converting a continuous high-pressure reactor from a gasifier to a combustor(4). A schematic of the combustion turbine simulator is shown in Figure 1. This device is capable of simulating(3,4) the following combustion turbine conditions:

- Super-atmospheric pressure: 4 atmospheres.
- Maximum coal flame temperature: 2600 F.
- Maximum firing temperature: 1900-2100 F.
- Maximum liner temperature: 1000-1500 F.
- Primary fuel/air ratio: 20 percent excess air.
- Overall residence time: 150-300 milliseconds.
- Carbon conversion efficiency: 99+ percent.

A premixed methane/air pilot flame was first used to ignite the down-flowing pulverized coal feed at atmospheric pressure. The coal firing rate was then adjusted to about 40,000 Btu/hour. Primary air amounted to 20-30 percent of the total air required for combustion at 20 percent excess air. Secondary air made up the remainder. Temperatures were continuously monitored down the vertical axis of the combustor at locations in the pre-to-post flame zones using Inconel-sheathed Chromel-Alumel thermocouples. Firing temperature was adjustable over a 200 F range by either varying the amount of tertiary dilution air introduced or by oxygen enriching the secondary air to various levels. After combustion was completed within the 12-foot long, 6-inch diameter combustion chamber, samples of gaseous and solid products were collected using an uncooled stainless steel probe or a cyclone mounted in the exhaust, respectively. Flue gases were analyzed for CO_2, CO, O_2, and SO_2 using conventional analytical instrumentation(4). Once the diagnosis of atmospheric-pressure combustion conditions was completed, the system was pressurized to 65 pounds per square inch absolute (psia) and the gas/solid sampling procedure repeated.

The combustion test plan consisted of experiments designed to determine the comparative in situ sulfur capture efficiency, under simulated combustion turbine conditions of: (a) raw pulverized bituminous coal, (b) pulverized BTC prepared from this raw coal, and (c) a physical mixture of the raw pulverized coal and pulverized lime with the same amount of calcium added as for the BTC.

The two raw bituminous coals used were both from the Illinois No. 6 seam. As Table 1 shows, both had total sulfur contents of greater than 4.50 weight percent. The difference between them was that one's total sulfur was predominately organic, whereas the other's consisted of a near-equal split between organic and inorganic sulfur.

The raw coals were first dried to about 2 percent moisture, pulverized to 85-90 percent minus 200 mesh (75 microns), and then fired.

To produce BTC, coarse raw coal, 100 percent minus 20 mesh (850 microns), was first treated via the proprietary Battelle calcium impregnation process (1) to increase its molar Ca/S ratio to the levels listed in Table 1. Either commercial grade or technical grade lime was used as the source of the calcium. The difference between these calcium sources is purity and cost with the commercial grade being less pure and less expensive. The BTC was then dried to 2-3 percent moisture, pulverized to 85-90 minus 200 mesh, and then fired.

For the third fuel, finely-pulverized (85-90 percent minus 200 mesh) raw coal was physically mixed with either the commercial or the technical grade lime, each having a particle size of 100 percent minus 325 mesh (45 microns), and then fired. The physical mixtures' molar Ca/S ratios were adjusted to be as equivalent as possible to that of the BTCs (see Table 1).

Results

The following are the significant new results regarding sulfur capture of these latest combustion tests, the results of which are documented in Table 1:

- Inherent sulfur capture by raw Illinois No. 6 seam coal appears to be independent of sulfur form, i.e., organic vs inorganic.
- Sulfur capture by Illinois No. 6 seam coal treated via the Battelle calcium impregnation process (BTC) apepars to be independent of sulfur form and grade of lime at both low and high Ca/S ratios.
- Sulfur capture by BTC made from Illinois No. 6 seam coal is at least 50 percent more efficient than that achievable upon physically mixing raw coal and either grade of lime.
- Sulfur capture by BTC at low levels of calcium impregnation exhibits a positive pressure dependence over the entire range of pressures studied.
- All other positive effects of Battelle calcium impregnation on raw coal combustion performance(4) -- higher ash fusion temperatures, lower free-swelling indices, smaller fly ash, negative pressure dependence for NO_x -- are observed for the organic sulfur enriched Illinois No. 6 seam coal.

Acknowledgements

The authors gratefully acknowledge the financial support of this research by the U.S. Department of Energy under Contract No. DE-AC21-84MC21289, which is monitored by Mr. Nelson F. Rekos, Jr. of the Morgantown Energy Technology Center.

References

1. Feldmann, H. F. and Conkle, H. N., "Coal Catalysis Expands Gasifier Application Options", Energy Progress, 3:2, 105-109 (1983).

2. Merryman, E. L. and Levy, A., "In-Situ Capture of Sulfur in Combustion", Central States Section Combustion Institute, CSS/C1-82-10, 23 pp (1982).

3. Crouse, F. W., Chairman, Proceedings of the First Annual Heat Engines Contractors Review Meeting, Morgantown Energy Technology Center, United States Department of Energy, DOE/METC/84/31, 369 pp., November 1984.

4. Reuther, J. J., Conkle, H. N., Webb, P. R., and Feldmann, H. F., "In-Situ Sulfur Capture by Battelle Treated Coal Under Simulated Combustion Turbine Conditions", Processing and Utilization of High Sulfur Coals, pp. 485-498, Elsevier Science Publishers (1985).

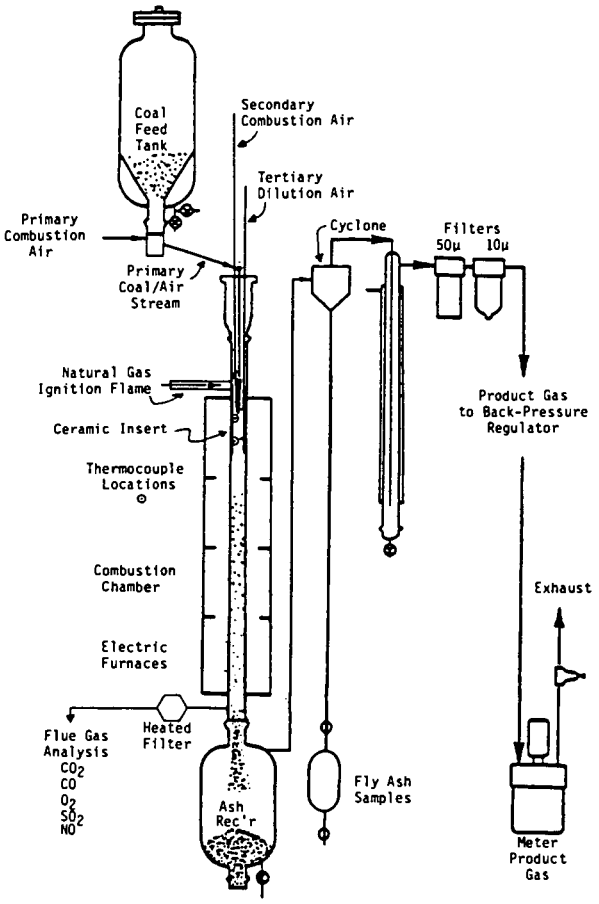

FIGURE 1. BATTELLE COMBUSTION TURBINE SIMULATOR

TABLE 1. SIGNIFICANT RESULTS OF TESTS TO STUDY THE EFFECT OF ORGANIC SULFUR CONTENT AND CALCIUM SOURCE ON SULFUR CAPTURE AS A FUNCTION OF PRESSURE, CALCIUM IMPREGNATION TECHNIQUE, AND Ca/S RATIO

Illinois No. 6 Seam Coal		Calcium			Sulfur Capture	
Total Sulfur (Weight %, DAF)	Organic Sulfur (%)	Impregnation Technique	Calcium Source	Ca/S Ratio	@15 PSIA (%)	@70 PSIA (%)
5.24	72	None	Nature	0.08	12±5	18±9
4.55	47	None	Nature	0.17	17±9	13±6
5.24	72	BTC	CGL	1.12	61±2	80±3
4.55	47	BTC	CGL	1.31	60±5	81±6
5.24	72	BTC	CGL	3.50	75±4	92±3
4.55	47	BTC	CGL	4.11	83±7	95±8
5.24	72	PM	CGL	0.98	35±10	57±18
5.24	72	PM	CGL	3.10	59±7	74±3
5.24	72	BTC	TGL	1.15	68±2	82±2
5.24	72	BTC	TGL	3.25	86±1	96±2

BTC = Battelle Treated Coal
PM = Physical Mix of Raw Coal and Lime
CGL = Commercial Grade Lime
TGL = Technical Grade Lime

Mechanism Of Radical-Radical Reactions: The Reaction Of Atomic Hydrogen With The Formyl Radical

Lawrence B. Harding and Albert F. Wagner

Chemistry Division, Argonne National Laboratory,
Argonne, IL 60439

Abstract

The addition and abstraction reaction pathways on the potential energy surface for H+HCO have been characterized by an *ab initio* four electron, complete active space, self-consistent field electronic structure calculation. The elimination pathway to go from the excited adduct H_2CO^* to products H_2+CO has already been characterized by others[1]. All this information is used in variational transition state theory and RRKM calculations to calculate a rate constant as a function of temperature and pressure. The room temperature value agrees with the lowest of three experimental measurements. The results indicate that abstraction is the dominant process.

I. Introduction

While the dissociative dynamics of H_2CO have been well studeid[1,2], the reverse reactions of the dissociation products are less well known. In particular the three measurements[3-5] of the rate of H+HCO differ by almost an order of magnitude and have only been done at room temperature. Like many radical-radical reactions, H+HCO has several possible pathways to reaction:

$$H + HCO \rightarrow H_2 + CO \qquad (1a)$$

$$H + HCO \rightarrow H_2CO^* \longrightarrow H_2 + CO \qquad (1b)$$

$$\qquad\qquad\quad \underset{[M]}{\longrightarrow} H_2CO \qquad (1c)$$

Reactions (1a) and (1b) are disproportionations by either direct, bimolecular abstraction or addition-elimination. Reactions (1c) is recombination by pressure stabliztion of buffer gas [M]. In this theoretical study, the reaction pathway of abstraction (1a) and of adduct formation in (1b) and (1c) are characterized by electronic structure calculations. Then this information along with the characterization of the elimination of (1b) are used in dynamics calculations of the rate constant.

II. Potential Surface Calculations

The calculations reported here employ the Dunning[6], valence, double-zeta contractions of the

*Work performed under the auspices of the Office of Basic Energy Sciences, Division of Chemical Sciences, U. S. Department of Energy, under Contract W-31-109-Eng-38.

Huzinaga[7] (9s,5p) sets of oxygen and carbon centered primitive Gaussians. For the hydrogens the (4s/2s) contraction was used with a scale factor of 1.2. In addition sets of d polarization functiions were centered on the carbon and oxygen (α_C=0.75, α_O=0.85) and one set of p polarization functions on each of the hydrogens (α=1.0).

With this basis set, four electron, four orbital complete active space, self-consistent field (CASSCF) calculations were carried out. In this wavefunction the four electrons invloved in the two CH bonds of formaldehyde are correlated with all possible orbital occupations of four orbitals, a total of 20 configurations. The remaining electrons are not correlated. With the exception of minor differences in the basis set, this is the same wavefunction used by Dupuis et al[1].

The calculations were carried out with the Argonne QUEST-164[8] programs, SOINTS and UEXP. An average calculation on a planar point took approximately 11 minutes on the FPS-164 while a typical nonplanar point required 16 minutes. The energy was evaluated at a total of appoximately 300 points.

Initially it was assumed that the addition and abstraction reaction coordinates could be approximated by the distance between the carbon and the incoming hydrogen. The grids of points were calculated at 0.5 au increments in this CH distance along the two paths. A total range of CH distances from 5 to 10 au was covered. Variations in the inactive geometrical parameters of 0.05 au for bond lengths, 5°-10° for bond angles and 10°-20° for the dihedral angle were used. These grids of points were then fit separately to Simons-Parr-Finlan type expansions, using the program SURVIB[9], inorder to obtain local representations of the potential surface in the region of the abstraction and addition reaction paths. The dependence of the energy on the angle of approach is depicted in Figure 1. From this figure it can be seen that there are two distinct reactive channels, one corresponding to abstraction and one to addition. The calculations predict no significant barrier in either channel.

The two reaction paths were then obtained by following steepest descent paths in mass-weighted, atomic cartesian coordinates. The starting points for the two paths were obtained by freezing the CH distance at 8 au and optimizing the remaining geometrical parameters. Two minima were found in this procedure (see Figure 1), one in which the incoming hydrogen is trans to the HCO hydrogen and a second in which the two hydrogens are cis, these were used as starting points for the addition and abstraction paths respectively. A plot of the energy along the two reaction paths is given in Figure 2. Vibrational frequencies were obtained along the reaction paths by numerically calculating the second derivative matrix in mass-weighted atomic cartesian coordinates, projecting out the translations, rotations, and gradient vector, and then diagonalizing the resulting 5 dimensional matrix. Plots of the vibrational frequencies along the two reaction paths are given in Figures 3 and 4.

III. Rate Constant Calculations

The calculated frequencies, structures and energetics as a function of distance along the reaction path can be used directly in a variational transition state theory (VTST) calculation to produce the abstraction rate constant, ie., for Reaction (1a). In this calculation, the rate constant at each temperature is that one which is a minimum with respect to position along the reaction path. Two of

the vibrational frequencies go to free rotations of the HCO in the reactant asymptote. The partition function used in the VTST expression for these two degrees of freedom is approximated as the minimum of the vibration or free rotation partition function. Subsequent calculations will include the hindered rotor effects. The resulting abstraction rate constant is shown in Fig. 5 along with the three rate constants measurements refered to in the introduction.

The measurements include both abstraction and addition processes. The VTST rate constant for addition is also in Fig. 5. This rate constant was determined in the same way as for abstraction, only with the calculated addition frequencies, structures and energetics. However, unlike abstraction, this rate constant can not be directly compared to experiment because it is only an adduct formation rate constant to form metastable, highly vibrationally excited H_2CO^*. H_2CO^* may decay back to reactants, may go on to products by eliminating H_2, ie., Reaction (1b), or may be stabilized by buffer gas to thermalized H_2CO, ie., Reaction (1c). That fraction of the adduct formation rate constant that corresponds to elimination or stablization is what is needed for comparison to experiment. To determine that fraction, characterizations of the potential energy surface in the region of the H_2CO equilibrium and the elimination transition state H···H···CO are required. Then the stablization rate constant and variational RRKM theory can be used to calculate the rate constant for Reactions (1b) and (1c).

In electronic structure calculations of comparable quality, Dupuis et al.[1] characterized the structure and frequencies of both H_2CO at equilibrium and the H···H···CO elimination transition state. The calculated properties at the equilibrium are very close to the experimental values and for consistency are used in the rate constant calculations. In a careful study of the energetics, the best estimate of the calculated barrier height to elimination is 81±3 kcal/mole with the zero point energy correction. Experimental values[2] for the energetics give a number of about 84±1 kcal/mole. The expeimental value for the energetics of H_2CO dissociation to H+HCO is about 86±2 kcal/mole and is due to thermochemical measurements with the uncertainity from the heat of formation of HCO[10]. These experimental values for the enegetic placement of asymptotes and barrrier heights will be used in the rate constant calculations.

With the transitition states selected at each temperature by the VTST calculation for formation of the adduct, chemically activated RRKM calculations were be performed to determine the subsequent fate of the adduct. These calculations are of a standard form[11] with total angular momentum approximately included only as a thermally averaged value. A direct count Beyer-Swinehart algorithm[12] is used. Tunneling through the elimination barrier is included in in an Eckhart manner[13]. The final pressure dependent rate constant produced is in the high pressure limit the adduct formation rate constant in Fig. 5.

The calculations require as input the rate constant for stablization of the H_2CO^* by buffer gas. In the three experiments, the buffer gas differs. CO, H_2CO, and Ar were used at pressures ranging from a few torr to atmostpheric. Under these conditions, stablization of the adduct turns out to be an unlikely event and the calculations are not particularly sensitive to detailed specifications of the stablization rate constant. The rate constant used is the the Lennard-Jones gas kinetic rate constant

times an efficiency factor for stablization. The Lennard-Jones parameters are taken from the tabulation of Ref. 14 with the values for ethylene used for H_2CO^*. The efficiency factor is determined in a way to empirically mimic a master equation solution[15] and requires as input the average energy $\langle\Delta E\rangle$ transferred between buffer gas and metastable adduct per up and down collision. This value used (-20 cm^{-1}) were those measured[16] for CS_2, the only triatomic where direct measurement of $\langle\Delta E\rangle$ have been published. $\langle\Delta E\rangle$ was presumed to be independent of temperature[17].

To complete the input for the chemically activated RRKM calculations, the external rotations of the equilibrium and saddle points must be classified as either active or adiabatic. The external rotations are presumed similar to those of a symmetric top. The conserved total angular momentum and its projection on a space fixed axis are associated with the two larger moments of inertia and are treated adiabatically. The projection of the total angular momentum on the molecular axis is associated with the smallest moment of inertia and is not necessarily a conserved quantity. If there is substantial vibration-rotation interaction through centrifugal stretching or Coriolis coupling, the energy associated with this projection becomes active[18]. The amount of vibration-rotation interaction in H+HCO is unknown and so in the calculations this degree of freedom was treated both ways, either actively or adiabatically. Fortunately the results are not particularly sensitive to the choice and only those for the active treatment will be discussed.

In Fig. 5 the final calculated rate constant for reactions (1b) and (1c) as a function of pressure in Ar buffer gas is displayed for two different choices of the energetics of dissociation of formaldehyde. As mentioned above the experimental uncertainties in both the height of the elimination barrier and the H+HCO asymptote relative to the bottom of the H_2CO well are a few kcal/mole. The two cases in Fig. 5 are for the difference between the asymptote and barrier (ie., ΔE) being as large or as small as these uncertainties allow. The pressure dependence of the calculated rate constants show that stabilization (1c) is a minor process relative to elimination (1b) although, as expected, it is more important if the elimination barrier and the H+HCO asymptote are very close to one another. The importance of elimination should increase with changing the buffer gas to CO or H_2CO but not so as to qualitatively change the results. The figure also shows by comparison to the adduct formation rate that the most likely fate of the adduct is to decompose back to reactants. This is due to the fact that the elimination transition state is a tight, constricted configuration and the lifetime of the adduct (which controls stablization) is short because it is only a 4 atom system. As a result, direct abstraction is the dominant process. The sum of abstraction, addition-elimination, and stablization rate constants gives a total rate constant at or slightly below (depending on the choice of energetics) the lowest and most recent experimental value[5].

References

1. M. Dupuis, W. A. Lester, Jr., B. H.Lengsfield III and B. Liu, *J. Chem. Phys.* **79**, 6167 (1983) and references therein.
2. C. B. Moore, *Ann. Rev. Phys. Chem.* **34**, 525 (1983).
3. J. P. Reilly, J. H. Clark, C. B. Moore and G. C. Pimentel, *J. Chem. Phys.* **69**, 4381 (1978).
4. V. A. Nadtochenko, O. M. Sarkisov and V. I. Vedeneev, *Dokl. Akad. Nauk SSSR.* **244**, 152 (1979).
5. C. J. Hochanadel, T. J. Sworski and P. J. Ogren, *J. Phys. Chem.* **84**, 231 (9180).
6. T. H. Dunning Jr., and P. J. Hay, "Methods of Electronic Structure Theory", H. F. Schaefer III, Ed., Plenum Press, New York, **1971**, Chapter 1.
7. S. Huzinaga, "Approximate Atomic Wavefunctions. I", Chemistry Report, University of Alberta, Edmonton, Alberta, Canada, **1971.**
8. R. Shepard, R. A. Bair, R. A. Eades, A. F. Wagner, M. J. Davis, L. B. Harding, T. H. Dunning Jr., *Int. J. Quantum Chem. Symp.* **1983**, 17,613.
9. L. B. Harding and W. C. Ermler, *J. Comp. Chem.* **1985**, 6,13.
10. P. Warneck, *Z. Naturforsch. Teil A* **29**, 350 (1974).
11. P. J. Robinson and K. A. Holbrook, *Unimolecular Reactions* (Wiley-Intersience, New York, **1972**) Chaps. 4 and 8.
12. D. C. Asholtz, J. Troe and W. Wieters*J. Chem. Phys.* **70**, 5107 (1979).
13. W. H. Miller, *J. Amer. Chem. Soc.* **101**, 6810 (1979).
14. H. Hippler, J. Troe and H. J. Wendelken *J. Chem. Phys.* **78**, 6709 (9183).
15. J. Troe, *J. Phys. Chem.* **1983**, *87*, 1800.
16. J. E. Dove, H. Hippler and J. Troe *J. Chem. Phys.* **82**, 1907 (1985).
17. M. Heymann, H. Hippler and J. Troe *J. Chem. Phys.* **80**, 1853 (1984).
18. W. Forst, *Theory of Unimolecular Reactions* (Academic Press, New York, **1973**) Chap. 5.

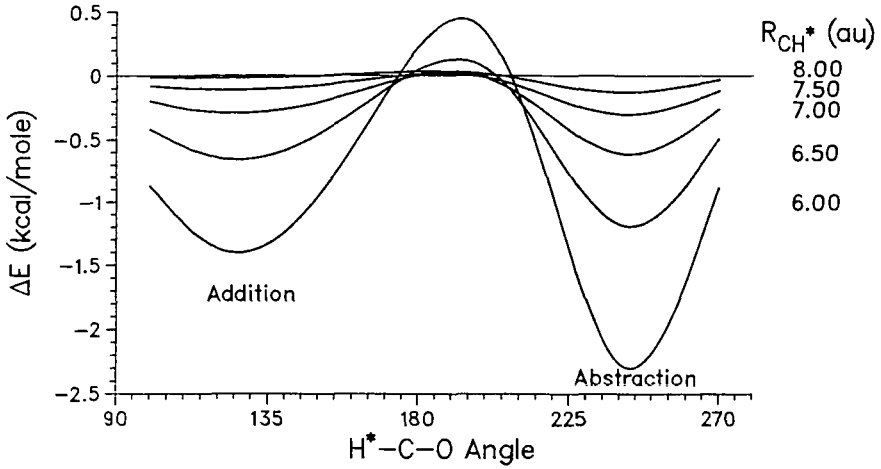

Figure 1. Angular dependence of the energy in the approach of atomic hydrogen to the formyl radical.

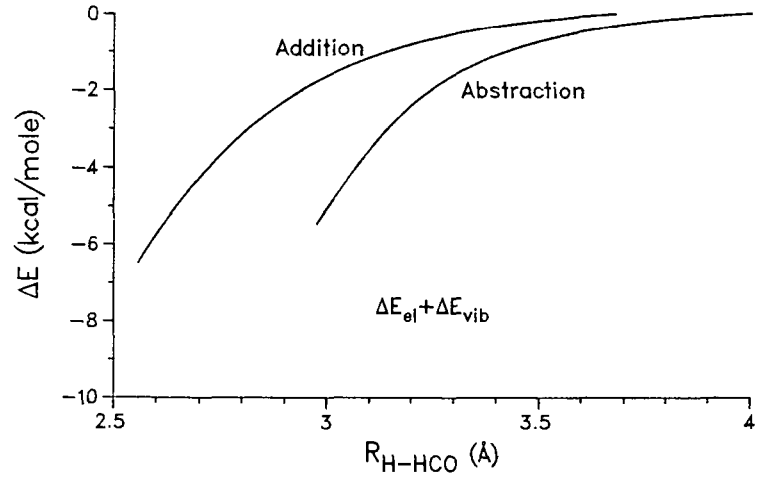

Figure 2. Energy profiles along the addition and abstraction reaction paths.

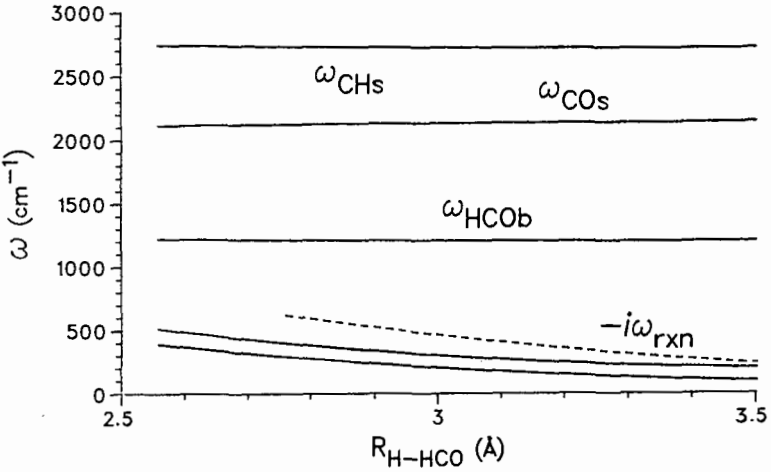

Figure 3. Vibrational frequencies along the addition reaction path.

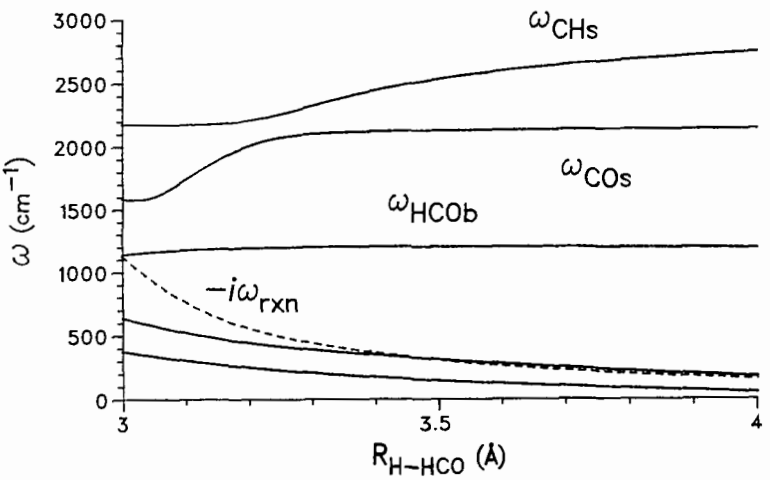

Figure 4. Vibrational frequencies along the abstraction reaction path.

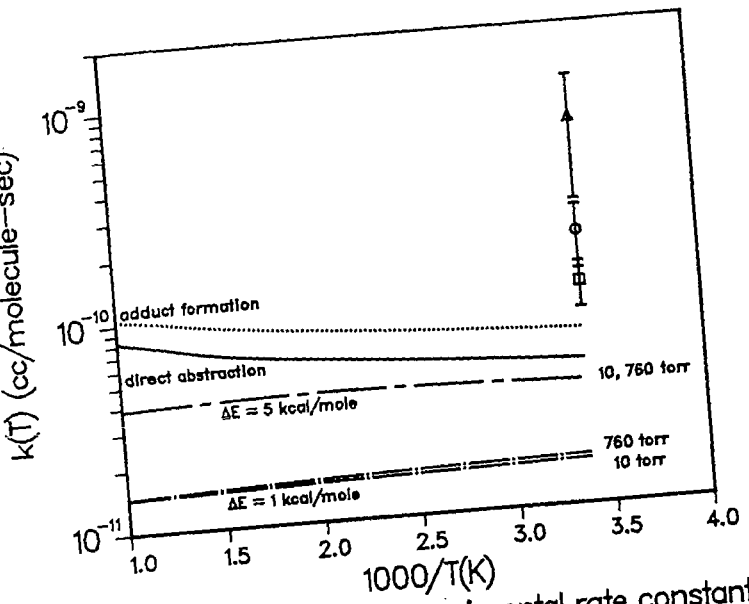

Figure 5. Calculated and experimental rate constants versus inverse temperature

Thermal and State-Selected Rate Constant Calculations for $O(^3P) + H_2 \rightarrow OH + H$ and Isotopic Analogs

Donald G. Truhlar

Department of Chemistry
University of Minnesota
Minneapolis, Minnesota 55455

Bruce C. Garrett
Chemical Dynamics Corporation
1550 West Henderson Road
Columbus, Ohio 43220

Abstract

We use ab initio potential energy surfaces, including new parametrizations of the bending potentials for the two lowest electronic states, to calculate the rate constants for the reaction $O(^3P) + H_2$. The dynamics calculations are based on variational transition state theory with multidimensional semiclassical tunneling corrections. We present results for the temperature range 250-2400K. In general the calculated rate constants for the thermal reaction are in excellent agreement with available experiments. We also calculate the enhancement effect for exciting H_2 to the first excited vibrational state. For the reaction of vibrationally excited H_2 the rate constant is based on a dynamical bottleneck of 7.2 kcal/mol, as compared to a saddle point value of 12.6 kcal/mol, and it is in good agreement with experiment. The good agreement of theory and experiment for the excited state rate provides a dramatic demonstration of the reality of dynamical bottlenecks at locations far from the saddle point.

1. Introduction

Theoretical advances in chemical kinetics often require integration of several kinds of information. The combination of electronic structure and chemical dynamics calculations provides one particularly fruitful way to gain a detailed understanding of the forces responsible for observed kinetic phenomena. In our own work we have made several calculations of chemical reaction rates based on potential energy surfaces derived in whole or in part on ab initio electronic structure theory. Systems studied have included the reactions $H + H_2$, $OH + H_2$, $O + OH$, $F + H_2$, and $O + H_2$.

The $O + H_2$ reaction, unlike all the others on the above list, has more than one low-lying potential energy surface. In addition to the $^1A'$ water surface, that does not correlate adiabatically to the ^3P state of O, there are two $^3A'$ surfaces and a $^3A''$ one that do. One $^3A'$ surface and the $^3A''$ surface form a degenerate Π state for all collinear goemetries but have different bend potentials: The $^3A''$ state has a significantly broader bending valley, and hence it dominates the thermal rate at most temperatures of interest, although the $^3A'$ state may make a non-negligible contribution at high temperature (1,2). The second $^3A'$ state is unimportant for the thermal reaction rate. In our previous calculations (3,4) we included only the contributions from reaction on the lowest-energy $^3A''$ surface. The collinear part of this surface was treated by the modified rotated Morse oscillator spline fit of Lee et al. (5) to the ab initio calculations of Walch et al. (1,2,6) and the bend potential was treated by an anti-Morse bend model (7-9) with one parameter adjusted to reproduce the harmonic bend potential at the saddle point for the same ab initio calculations. In the present paper we include both electronic states, and the potential energy surfaces are treated by an improved parametrization. The improved parametrization consists, for each of the two surfaces, of a three-parameter fit to the bend potential so that it agrees with the newest ab initio calculations (10)

for large-amplitude (45°) bends at three points along the reaction path, including both the saddle point and a point close to the vibrationally adiabatic ground-state barrier maximum. We use the PolCI calculations of Walch et al. (1,6,10) because (i) they are available at enough geometries to determine both potential energy surfaces in the regions important for the reaction rate and (ii) they appear reasonably accurate. We note that in our previous study (4) of the $O + H_2$ reaction, we calculated rate constants for five potential energy surfaces. Two of these, called surfaces P and M, were based on the PolCI calculations, and the results appeared to show that these were the most accurate of the five.

The procedure used to fit the bend potential in the present study is a specific example of a strategy that may be very useful in many cases (11), namely the fitting of a globally defined potential in the wide vicinity of a reaction path with special emphasis on dynamical bottleneck locations (12) as determined by variational transition state theory (13,14) or the adiabatic theory of reactions (15).

Having obtained a representation of the potential energy surface, we calculated both thermal rate constants and state-selected rate constants for vibrationally excited H_2 by variational transition state theory with semiclassical ground-state transmission coefficients (3,16-18). These methods have been shown to provide reasonably accurate estimates of the quantum mechanical local-equilibrium and state-selected reaction rates for most chemical reactions (3,13,14,19,20). In general we believe we can use these methods to calculate rate constants that are reliable for a given potential energy surface to within a factor of two or better at room temperature and above. This is sufficient to compare computed rate constants to experiment, to test ab initio potential energy surfaces, and to draw useful conclusions about which features of the potential energy surface are significant for determining the magnitudes of observed rate constants and kinetic isotope effects.

2. Potential Energy Surfaces

The $^3\Pi$ potential energy surface is represented by the rotated Morse oscillator spline function of Lee et al. (5) for collinear geometries augmented by an anti-Morse bend (AB) potential (7-9). The parameters of the bend potential are adjusted to ab initio calculations (1,6,10) in the region near the saddle point and the vibrationally adiabatic ground-state barrier maximum {the maximum of $V_a^G(s)$ in the notation used previously (12,17)}. Further details are given elsewhere (21).

3. Dynamical Calculations

We calculated a separate rate constant for each potential energy surface. Denoting these results by $k_{A''}$ and $k_{A'}$ respectively, the thermal (i.e., canonical ensemble) rate constant is

$$k = k_{A'} + k_{A''} \qquad 1)$$

Each of the single-surface rate constants includes a multiple-surface coefficient (22) equal to $3/Q_O^{el}$ where 3 is the electronic degeneracy of the generalized transition state and Q_O^{el} is the electronic partition function of atomic O.

The single-surface rate constants were calculated by improved canonical variational transition-state-theory (ICVT) with semiclassical ground-state transmission coefficients. The methods are described in detail elsewhere (3,16-18). First we calculate the minimum energy path (MEP) by following the negative gradient of the potential in mass-scaled coordinates. Then for each distance s along the MEP we calculate the improved generalized standard-state free energy of activation $\Delta G^{IGT,O}(T,s)$ for a generalized transition state at this s, where T is the temperature. The hybrid ICVT rate constant for temperature T is then given by

$$k^{ICVT}(T) = \min_s \frac{\tilde{k}T}{h} K^{\neq,0} \exp[-\Delta G^{IGT,0}(T,s)/\tilde{k}T] \qquad 2)$$

where $\tilde{k}$ is Boltzmann's constant, h is Planck's constant, and K^0 is the reciprocal of the standard-state concentration. This rate constant is a hybrid because the reaction coordinate is treated classically but other degrees of freedom are all treated quantally. In the final step we add quantal effects on the reaction coordinate by a ground-state (G) transmission coefficient $\kappa^G(T)$:

$$k^{ICVT/G}(T) = \kappa^G(T) k^{ICVT}(T) \qquad 3)$$

We consider two methods to approximate $\kappa^G(T)$: the minimum-energy-path semiclassical adiabatic method (MEPSAG) (17) and the least-action method (LAG)(18). The latter accounts for the shortening of the tunneling path due to the system "cutting the corner" of the curved MEP through mass-scaled coordinates by finding the dynamically optimal tunneling path by evaluating an imaginary-action functional along a one-parameter sequence of trial paths. These vary linearly between the MEP at one extreme and a straight line through mass-scaled coordinates from the translational turning point on the MEP in the entrance channel to the translational turning point on the MEP in the exit channel at the other extreme.

Anharmonicity is included as discussed elsewhere (3,17).

The evaluation of state-selected rate constants for H_2 in the n=1 excited vibrational state requires further assumptions. Figure 1 shows the vibrationally adiabatic potential curves for n=0 and 1 for the $^3A''$ surface. The potential curves in Fig. 1 are defined by

$$V_a^g(n,s) = V_{MEP}(s) + \varepsilon_{str}(n,s) + 2\varepsilon_{bend}^g(s) \qquad 4)$$

where $V_{MEP}(s)$ is the Born-Oppenheimer potential on the MEP, $\varepsilon_{str}(n,s)$ is the local vibrational energy of the stretching mode orthogonal to the MEP and in quantum state n, and $2\varepsilon_{bend}^g(s)$ is the local zero point energy of the twofold-degenerate bending mode. Figure 2 shows the same quantities for the $^3A'$ state. In both cases we also show the curvature $\kappa(s)$ of the MEP through mass-scaled coordinates (17). We will consider two limits for the excited-state rate constants. The first is the adiabatic limit (4,16,18,23), in which case we perform calculations identical to those for the thermal reaction rate except that in both $\Delta G^{IGT,0}(T,s)$ and the tunneling calculation we neglect all stretching vibrational states except the n=1 state. The second treatment is a sudden nonadiabatic model explained elsewhere (21).

We will consider three reactions:

$$O + H_2 \rightarrow OH + H \qquad R1)$$

$$O + D_2 \rightarrow OD + D \qquad R2)$$

$$O + HD \rightarrow OH + D \text{ and } OD + H \qquad R3)$$

4. Results

Table I shows results for two methods of calculating transmission coefficients. The MEPSAG results are based on a semiclassical adiabatic treatment of tunneling along the minimum energy path (17). As compared to the LAG method this underestimates the rate constrant by a factor of 24 at 200K and a factor of 3.3 at 300K. This

confirms, as first discovered for the $H + H_2$ reaction (24) and then found in many cases (4,13,16-19,25-31), that multidimensional effects on the tunneling probabilities are very important and reduction to a one-dimensional problem by simply straightening out the minimum-energy reaction path seriously underestimates the extent of tunneling.

Table I also compares the final thermal rate constants of this study for reaction R1) to a selection of experimental (32-34) results. For 297-472K, the table shows only the most recent experimental data (32). The ICVT/LAG rate constants are usually larger than these results but agree within 25%. Rate constants in this temperature range are very sensitive to the barrier height, and the uncertainty in the ab initio potential energy surface is certainly great enough to yield larger errors. Thus the agreement of the present calculations with experiment is better than could have been expected. Furthermore the other recent experimental measurements in this range do not all agree with those of Presser and Gordon within a factor of two. The most recent evaluation (33) of experimental data for the $O + H_2$ reaction concludes that for $T \geq 400K$ the expression of Baulch et al. (34) fits most of the data within experimental error. We use this expression for the experimental values at 600-1500K. In this temperature range the present calculated rate constants are all larger than these experimental results, but the ICVT/LAG results are high only by factors of 1.2-1.5. At 2400K the agreement with experiment (35) is excellent.

We also calculated thermal rate coefficients for the isotopic analog reactions and the kinetic isotope effects and compared them to experimental (32,34-37) results. Because of space limitations we simply point out here that the calculated results agree with the experimental ones within the reliability of the latter. We also calculated kinetic isotope effects by conventional transition state theory (TST). These are qualitatively similar to the ICVT/LAG results, and hence also to the experimental results, but that is at least partly fortuitous since TST greatly underestimates the individual isotopic rate constants. For example for reaction R1) the TST rate constant is a factor of 9.3 lower than the ICVT/LAG one at 300K and a factor of 2.5 smaller at 400K. The LAG transmission coefficients are even larger, 12.6 at 300K and 3.1 at 400K, but the lack of quantal effects on reaction-coordinate motion in conventional TST is partly compensated by the lack of variational minimization of the hybrid rate constant with respect to the location of the generalized transition state. Then a further cancellation of errors occurs in the kinetic isotope effect ratio.

The adiabatic and sudden nonadiabatic rate constants for reaction R1) with vibrationally excited H_2 are very similar for the present potential energy surface; thus we tabulate only the adiabatic values. The rate constants calculated by the adiabatic theory for reaction R1) when H_2 is excited to the n=1 vibrational state are given in Table II. We see that the transmission coefficients (ratios of ICVT/LAG tunneling-corrected rate constants to ICVT hybrid ones) are 2.6-2.7 at 302K, which are very significant factors but are smaller than for the thermal reaction rate. At 302K the calculated vibrational enhancement factor in the ICVT/LAG approximation is 1.4×10^3 by Light (38), but it is only 8.2×10^2 times larger than the interpolated vaule of Presser and Gordon (32). The agreement of theory with experiment is satisfactory.

Table III shows some of the properties of the dynamical bottlenecks for the vibrationally excited reaction. The variational transition states are farther from the saddle point (s=0) for the vibrationally excited reaction than for the thermal reaction. Similar results have been found previously for $H + H_2$ (23) and $OH + H_2$ (39) for vibrationally excited reactants. This means that the improved parametrization of the bend potential for geometries far from the saddle point becomes more important for n=1. It also means that conventional TST becomes worse. Conventional TST predicts a vibrational enhancement factor of 2.5×10^5 at 302K, which is two orders larger than the accurate values. The good agreement of the ICVT/LAG values with experiment provides a dramatic demonstration of the reality of dynamical bottlenecks at locations far from the saddle point.

5. Acknowledgments

The authors are grateful to A. F. Wagner for helpful correspondence. The work at the University of Minnesota was supported in part by the U.S. Department of Energy, Office of Basic Energy Sciences, under contract no. DE-AC02-79ER10425 and that at Chemical Dynamics Corporation was supported in part by the Army Research Office through contract no. DAAG-29-84-C-0011.

TABLE I. Thermal rate constants ($cm^3 molecule^{-1} s^{-1}$) for $O + H_2 \rightarrow OH + H$.

T(K)	ICVT	ICVT/MEPSAG	ICVT/LAG	Exp.
250	2.94(-20)	2.35(-19)	1.77(-18)	...
297	8.45(-19)	3.32(-18)	1.15(-17)	1.0(-17)[a]
318	2.76(-18)	8.85(-18)	2.38(-17)	1.9(-17)[a]
370	2.93(-17)	6.66(-17)	1.20(-16)	1.1(-16)[a]
422	1.75(-16)	3.24(-16)	4.70(-16)	3.8(-16)[a]
472	6.84(-16)	1.10(-15)	1.43(-15)	1.2(-15)[a]
600	8.21(-15)	1.09(-14)	1.24(-14)	1.0(-14)[b]
1000	3.89(-13)	4.28(-13)	4.45(-13)	3.4(-13)[b]
1500	3.31(-12)	3.43(-12)	3.52(-12)	2.3(-12)[b]
2400	2.10(-11)	2.07(-11)	2.15(-11)	2.1(-11)[c]

[a] Presser and Gordon (32).

[b] Baulch *et al.* (34).

[c] Pamidimukkala and Skinner (35).

TABLE II. Rate constants ($cm^3 molecule^{-1} s^{-1}$) for the state-selected reaction $O + H_2(n=1) \rightarrow OH + H$.

T(K)	ICVT	ICVT/LAG	Exp.[a]
250	1.03(-15)	4.25(-15)	...
302	7.31(-15)	1.89(-14)	1.0(-14)
400	7.68(-14)	1.31(-13)	...
1000	8.58(-12)	9.33(-12)	...
2400	7.73(-11)	7.84(-11)	...

[a] from Light (38).

TABLE III. Bottleneck properties at conventional and canonical variational transition states for $O + H_2(n=1) \rightarrow OH + H$.[a]

Surface	T (K)	s (a_0)	r_{12} (a_0)	r_{23} (a_0)	V_{MEP} (kcal/mol)	$V_a^g(n=1)$ (kcal/mol)	$\epsilon_{str}(n=1)$ (kcal/mol)	$2\epsilon_{bend}^g$ (kcal/mol)
$^3A''$	...	0.00	2.29	1.74	12.58	19.07	4.89	1.61
	300	-0.55	2.95	1.45	7.22	23.02	14.74	1.07
	1000	-0.51	2.91	1.45	7.64	22.96	14.22	1.10
$^3A'$	...	0.00	2.29	1.74	12.58	20.00	4.89	2.53
	300	-0.54	2.93	1.45	7.36	23.92	14.57	1.98
	1000	-0.51	2.90	1.45	7.69	23.87	14.14	2.04

[a] r_{12} and r_{23} are the nearest-neighbor OH and HH distances at the saddle point (s=0) or the variational transition state for the temperature indicated. 1 a_0 = 1 bohr = 0.5292 Å.

References

(1) S. P. Walch, A. F. Wagner, T. H. Dunning, Jr., and G. C. Schatz, J. Chem. Phys. 72, 2894 (1980).

(2) T. H. Dunning, Jr., S. P. Walch, and A. F. Wagner, in Potential Energy Surfaces and Dynamics Calculations, edited by D. G. Truhlar (Plenum Press, New York, 1981), p. 329.

(3) B. C. Garrett and D. G. Truhlar, J. Chem. Phys. 81, 309 (1984).

(4) D. G. Truhlar, K. Runge, and B. C. Garrett, in Proc. Twentieth Int. Symp. Combustion (Combustion Institute, Pittsburgh), p. 585.

(5) K. T. Lee, J. M. Bowman, A. F. Wagner, and G. C. Schatz, J. Chem. Phys. 76, 3563 (1982).

(6) S. P. Walch, T. H. Dunning Jr., F. W. Bobrowicz, and R. Raffenetti, J. Chem. Phys. 72, 406 (1980).

(7) H. S. Johnston, Gas Phase Reaction Rate Theory (Ronald Press, New York, 1966).

(8) B. C. Garrett and D. G. Truhlar, J. Am. Chem. Soc. 101, 4534 (1979).

(9) B. C. Garrett, D. G. Truhlar, and A. W. Magnuson, J. Chem. Phys. 76, 2321 (1982).

(10) J. M. Bowman, A. F. Wagner, S. P. Walch, and T. H. Dunning, Jr., J. Chem. Phys. 81, 1739 (1984).

(11) D. G. Truhlar, F. B. Brown, R. Steckler, and A. D. Isaacson, in Proceedings of the NATO/CECAM Workshop on Theory of Chemical Reaction Dynamics, Orsay, France, June 1985.

(12) B. C. Garrett, D. G. Truhlar, and R. S. Grev, in Potential Energy Surfaces and Dynamics Calculations, edited by D. G. Truhlar (Plenum Press, New York, 1981), p. 587.

(13) D. G. Truhlar and B. C. Garrett, Acc. Chem. Res. 13, 440 (1980).

(14) D. G. Truhlar and B. C. Garrett, Annu. Rev. Phys. Chem. 35, 159 (1984).

(15) D. G. Truhlar, J. Chem. Phys. 53, 2041 (1970).

(16) B. C. Garrett and D. G. Truhlar, J. Phys. Chem. 83, 1079 (1979), errata: 84, 682 (1980), 87, 4553 (1983).

(17) B. C. Garrett, D. G. Truhlar, R. S. Grev, and A. W. Magnuson, J. Phys. Chem. 84, 1730 (1980); errata: 87, 4554 (1983).

(18) B. C. Garrett and D. G. Truhlar, J. Chem. Phys. 79, 4931 (1983).

(19) D. G. Truhlar, A. D. Isaacson, R. T. Skodje, and B. C. Garrett, J. Phys. Chem. 86, 2252 (1982); errata: 87, 4554 (1983).

(20) D. G. Truhlar, W. L. Hase, and J. T. Hynes, J. Phys. Chem. 87, 2664 (1983); errata: 87, 5523 (1983).

(21) B. C. Garrett and D. G. Truhlar, Int. J. Quantum Chem., to be published.

(22) D. G. Truhlar, J. Chem. Phys. 56, 3189 (1972), 61, 440(E) (1974).

(23) B. C. Garrett and D. G. Truhlar, J. Phys. Chem. 89, 2204 (1985).

(24) D. G. Truhlar and A. Kuppermann, Chem. Phys. Lett. 9, 269 (1971).

(25) R. A. Marcus and M. E. Coltrin, J. Chem. Phys. 67, 2609 (1977).

(26) B. C. Garrett and D. G. Truhlar, J. Chem. Phys. 72, 3460 (1980).

(27) B. C. Garrett, D. G. Truhlar, R. S. Grev, and R. B. Walker, J. Chem. Phys. 73, 235 (1980).

(28) D. K. Bondi, D. C. Clary, J. N. L. Connor, B. C. Garrett, and D. G. Truhlar, J. Chem. Phys. 76, 4986 (1982).

(29) R. T. Skodje, D. G. Truhlar, and B. C. Garrett, J. Chem. Phys. 77, 5955 (1982).

(30) D. K. Bondi, J. N. L. Connor, B. C. Garrett, and D. G. Truhlar, J. Chem. Phys. 78, 5981 (1983).

(31) A. D. Isaacson, M. T. Sund, S. N. Rai, and D. G. Truhlar, J. Chem. Phys. 82, 1338 (1985).

(32) N. Presser and R. J. Gordon, J. Chem. Phys. 82, 1291 (1985).

(33) N. Cohen and K. Westberg, J. Phys. Chem. Ref. Data 12, 531 (1983).

(34) D. L. Baulch, D. D. Drysdale, D. G. Horne, and A. C. Lloyd, Evaluated Kinetic Data for High-Temperature Reaction, Vol. 1 (Butterworths, London, 1972), p. 49.

(35) K. M. Pamidimukkala and G. B. Skinner, J. Chem. Phys. 76, 311 (1982).

(36) A. Westenberg and N. deHaas, J. Chem. Phys. 47, 4241 (1967).

(37) A. Westenberg and N. deHaas, J. Chem. Phys. 50, 2512 (1969).

(38) G. C. Light, J. Chem. Phys. 68, 2831 (1978).

(39) D. G. Truhlar and A. D. Isaacson, J. Chem. Phys. 77, 3516 (1982).

Figure captions

Fig. 1. Vibrationally adiabatic potential curves (solid curves with scale at left) defined by eq. 4) for n=0 and 1 and curvature of the reaction path (dashed curve with scale at right) as functions of the distance s along the minimum energy path through mass-scaled coordinates for the $^3A''$ potential energy surface. The saddle point is at s=0. The long tick marks on the ordinate scales denote the energies of $O + H_2(n=1)$, left side, and $OH(n=1) + H$, right side.

Fig. 2. Same as Fig. 1 except for $^3A'$ surface.

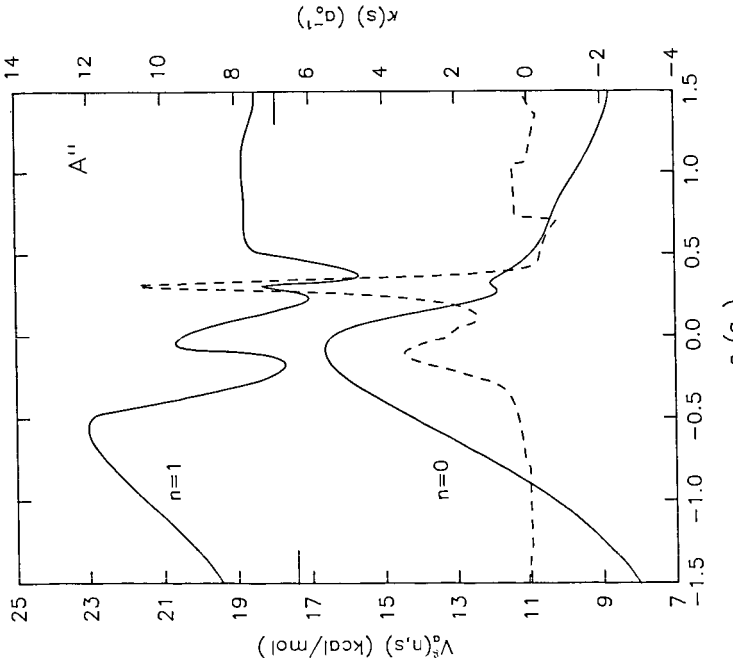

Fig. 1. Vibrationally adiabatic potential curves (solid curves with scale at left) defined by eq. 4) for n=0 and 1 and curvature of the reaction path (dashed curve with scale at right) as functions of the distance s along the minimum energy path through mass-scaled coordinates for the $^3A''$ potential energy surface. The saddle point is at s=0. The long tick marks on the ordinate scales denote the energies of $O + H_2(n=1)$, left side, and $OH(n=1) + H$, right side.

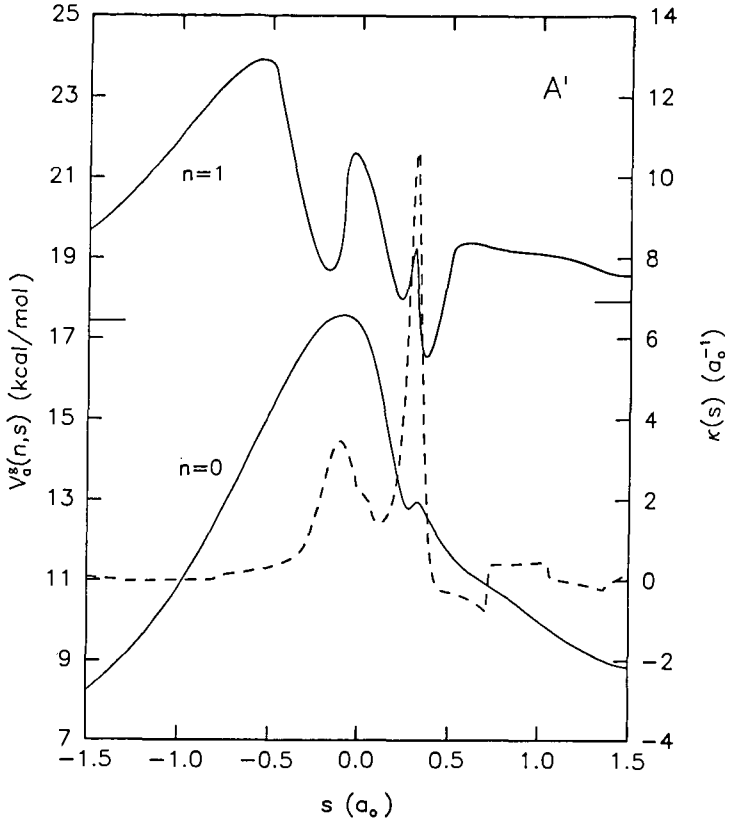

Fig. 2. Same as Fig. 1 except for $^3A'$ surface.

FUNDAMENTALS OF NITRIC OXIDE FORMATION IN FOSSIL FUEL COMBUSTION

Thomas J. Houser, Michael E. McCarville and Gu Zhuo-Ying

Chemistry Department, Western Michigan University
Kalamazoo, MI 49008

INTRODUCTION

Combustion of fossil fuels in large stationary furnaces causes the emission of nitrogen oxides, a large fraction of which arise from the nitrogen-containing components in the fuel, producing a major pollution problem which is expected to increase in severity in the future. The results being reported in this paper are part of those obtained from a continuing study to determine the mechanism by which these oxides may form. Because studies have shown that most of the nitrogen in heavy oils is in the form of heterocycles (1-3) and it is believed that the nitrogen components of coal are similar, pyridine was selected as representative of these components. It was assumed that the radical fragments formed during pyridine pyrolysis and rich, low temperature oxidation would be similar to those obtained from the same reactions of fossil fuels that occur during the pre-flame stages of combustion. Later experiments emphasized HCN oxidation since several studies indicated that it was the key volatile, nitrogen-containing intermediate formed during fuel nitrogen combustion (4-8). In addition, HCN used with several fuel additives allowed a greater control of the chemical nature of the reaction environment. We have previously reported on the inert pyrolysis kinetics of pyridine (9), the rate of formation of HCN during pyridine pyrolysis (10), the oxidation kinetics of cyanogen (11), and of pyridine (12) and HCN (13) at low temperatures.

EXPERIMENTAL

A flow system designed to operate at atmospheric pressure was constructed for the study of the oxidation of the pertinent nitrogen-containing reactants. The system is suitable for the introduction of volatile liquids (reactants and solutions with additives) into a heated helium stream through the use of a syringe pump to drive a calibrated, tuberculin syringe. The system can also utilize gaseous species; these reactants and additives, mixed with helium at the desired concentrations, are maintained in steel storage tanks. The flow stream is examined by a quadrupole mass analyzer equipped with capillary probe atmospheric sampler which functioned as an on stream monitor for the consumption of reactants. Helium is used as the carrier gas because it is chemically inert and has a very high thermal conductivity, thus providing rapid heating and quenching. The system has a group of removable Vycor reactors heated by an electric furnace. One reactor was a stirred-flow design (40 cc) which had been previously tested for stirring efficiency (14), the others were plug-flow type (10 to 40 cc). A flow line which bypasses the reactor was used so that entrance and exit concentrations of reactants could be measured. A Thermo Electron Chemiluminescent NO/NO_x analyzer with on stream sampling was used for the oxidation studies of pyridine, HCN and N_2O. A modification of the flow stream was required to obtain direct samples from the reactor effluent to measure the light gases with a gas chromatograph. A linear switching valve was used to provide a series-bypass capability with

constant back pressure for the two columns. A molecular sieve 5A column was used for O_2, N_2 and CO while a porous polymer Chromosorb 101 column was used for CO_2 and N_2O. In order to determine the amounts of HCN and NH_3 produced from the oxidation of pyridine and HCN, dilute solutions of NaOH or HCl in the bubble towers were used in separate experiments to trap the HCN or NH_3 respectively, for ion-specific electrode analysis. A second bubbler in series with the first was found to be unnecessary.

RESULTS AND DISCUSSION

The current study has shown that in order to produce significant yields of NO from the oxidation of pyridine or HCN-fuel mixtures, conditions which promote a flame must exist in the flow reactor. The existence of a flame was confirmed by visual observation in several, but not all, experiments. The capability of producing a flame depends on the nature of the fuel (Tables 1, 2 and 3, all data are stirred-flow), temperature (Tables 1, 2, 3 and 5), concentrations (Tables 1-5), reactor design (stirred - or plug-flow, Table 5), and flow rate (Tables 1 and 5). The conditions which promoted NO formation where characterized by complete consumption of fuel-nitrogen at all flow rates in the stirred-flow reactor, however, the plug-flow reactor exhibited an inverse consumption at intermediate temperatures, at first decreasing from complete consumption at high flows, passing through a minimum then increasing again (Table 5, C_5H_5N and HCN/C_6H_6 mixtures at 800 C and HCN/CO at 700 C) while the NO yield continually decreased. After a threshold temperature was reached in the plug-flow reactor, the NO yield did not appear to depend on temperature significantly (Table 5). The non-flame conditions, at relatively low temperatures and/or concentrations of fuels, were characterized by a flow rate dependent consumption of fuel-nitrogen which was converted essentially completely to N_2 and N_2O (maximum yield of about 50% of the latter) (12, 13). This was observed in both types of reactors, however, the flame condition persisted to a much lower temperature in the entrance of the plug-flow reactor as evidenced by visual observation and NO production. The observed dependence of NO yields on flow rate, first increasing to a maximum then decreasing (Tables 1, 2 and 5) in the stirred-flow reactor was not observed with plug-flow, thus is thought to be an anomaly due to reactor-induced flame instability. However, other yield dependencies are qualitatively the same in both types of reactors. The transition between flame and non-flame reaction was abrupt as evidenced by a rapid increase in fuel nitrogen consumption and shift in products, thus is attributed to a change in mechanism rather than a sequential process.

Specifically it was found that pyridine and benzene/HCN mixtures give similar results (Tables 1, 2 and 5) while CO (Tables 2 and 5) and acetylene (13) added to HCN promoted NO formation at lower temperatures and concentrations (on an atom or heat equivalent basis), than the other fuel combinations. Mixtures of H_2/HCN were very different from other fuel combinations, producing lower extents of HCN consumption and very low to negligible yields of NO at conditions which normally gave high yields of NO with other fuels (Table 1). Finally, it has been clearly established that N_2O was the prevalent oxide of nitrogen at low temperatures (Table 5 and Reference 15) and/or equivalence ratios (Table 4), whereas NO became prevalent at higher temperatures and fuel concentrations (up to stoichiometric mixtures) and that their concentrations were inversely related. In order to further check the possibility of NO/N_2O interconversion experiments were performed by adding NO_2 (NO did not exist in our reactant storage tank) to the

reaction mixture at low temperatures and by oxidizing N_2O in the presence of various fuels (Table 7). The results with NO were somewhat inconclusive since some experiments showed some increase in N_2O and others did not (16). The relatively small increases observed indicate that NO/NO_2 could not be a major source of N_2O at those conditions. The results with N_2O clearly show that NO is not formed from N_2O in large yields.

In addition to the volatile products observed, it was noted that a white solid was formed (about a 3% yield) at non-flame conditions with lean mixtures of $HCN/CO/O_2$ and $HCN/H_2/O_2$. Samples of these solids were examined by infrared and elemental analyses which indicated that those from HCN/CO were NH_4NCO, whereas most, but not all, of those from HCN/H_2 were urea (Table 8). It was also found that a room temperature sublimate from NH_4NCO was urea, indicating an easy conversion was possible. These solids show the presence of NH_3 and HNCO in the reactor at non-flame conditions. In an attempt to determine the nature of the intermediate that leads to N_2O formation, oxidation studies of methylisocyanate and dimethylhydrazine, with and without additive fuels, were made. No increase in N_2O formation was noted from these over that obtained from HCN.

CONCLUSIONS

The conclusions reached from the above observations are: (1) That N_2O and NO are probably formed from a common precursor in the mechanistic chain, although possibly not the same immediate intermediate, and neither are formed from each other. The data strongly shows that NO does not form at those lower temperatures which promote N_2O formation and N_2O does not oxidize to NO. In addition, the equivalence ratio dependence shows that N_2O forms at leaner conditions than does NO, which is most likely due to maintainance of flame conditions at the more rich condtions. Thus, the reported mechanism steps for the formation of N_2O from NO, at least at our conditions, are not applicable (17). (2) That NO formation cannot occur primarily by an interaction between NH or N and OH, as usually assumed in mechanisms (17), because of the observed influence of different fuels on the conditions necessary to produce NO.

ACKNOWLEDGEMENT

We are grateful to the U.S. Department of Energy for the financial support of this study under Contract No. DE-FG22-81PC408).

REFERENCES

1. L.R. Snyder, Anal. Chem., 41, 314 (1969).

2. C.F. Brandenburg and D.R. Latham, J. Chem. Eng. Data, 13, 391 (1968).

3. D.K. Albert, Anal. Chem., 39, 1113 (1967).

4. R.A. Altenkirch, R.E. Peck and S.L. Chen, Combustion Science and Tech., 20, 49 (1979).

5. C.P. Fenimore, Combustion and Flame, 26, 249 (1976).

6. B.S. Haynes, Combustion and Flame, 28, 81 (1977).

7. C. Morley, Combustion and Flame, 27, 189 (1976).

8. C. Morley, Eighteenth Symposium (International) on Combustion, 23 (1981).

9. T.J. Houser, M.E. McCarville and T. Biftu, Int. J. Chem, Kinet., 12, 555 (1980).

10. T.J. Houser, M. Hull, R.M. Alway and T. Biftu, Int. J. Chem. Kinet., 12, 569 (1980).

11. T.J. Houser and P.K. Lee, Combustion Science and Tech., 23, 177 (1980).

12. T.J. Houser, M.E. McCarville and B.D. Houser, Combustion Science & Tech., 27, 183 (1982).

13. T.J. Houser, M.E. McCarville and B.D. Houser, Combustion Science and Tech., 29, 101 (1982).

14. J.M. Sullivan and T.J. Houser, Chem. Ind. (London), 1057 (1965).

15. T.J. Houser and M.E. McCarville, "Fundamentals of Nitric Oxide Formation in Fossil Fuel Combustion", DOE/PC/40805-4, May 1983.

16. T.J. Houser and M.E. McCarville, "Fundamentals of Nitric Oxide Formation in Fossil Fuel Combustion", DOE/PC/40805-7, July 1984.

17. G.T. Chen, J.V. Shang and C.Y. Wen, "NO_x Emission from Combustors - A State of the Art Review", DOE/MC/11284-166, May 1981 (Table 6).

TABLE 1 Fuel Type Effects on NO Yields (% of Reacted N) at 950 C
Reactants - Initial Concentrations (mole %)

Time(sec)\ER[a]	$.9C_5H_5N/7O_2$ .87	$1HCN/.5C_6H_6/7O_2$ .79	$1HCN/3CO/7O_2$ .46	$1HCN/3H_2/7O_2$ .46	$1HCN/3H_2/6O_2$[b] .54
0.375	13	18	42	--	0.4
0.5	12	26	35	0.5	0.3
0.75	27	67	34	--	--
1.0	69	66	32	0.3	0.2
2.0	44	42	19	--	--
4.0	6	14	5	--	--

Time(sec)\ER[a]	$.5C_5H_5N/7O_2$ .48	$.2HCN/.25C_6H_6/3.5O_2$ .64	$2HCN/5CO/7O_2$ .86	$2HCN/14O_2$ .25	$2HCN/7O_2$ .50
0.375	17	--	--	--	--
0.5	24	24	70	2.0	2.1
1.0	32	26	60	2.2	5.0
2.0	44	52	35	1.1	5.5
4.0	24	29	14	0.5	2.8

(a) Equivalence ratios were calculated on the basis of CO_2, H_2O and NO as products
(b) These were run at 900 C

TABLE 2 Temperature Effects on NO_x Yield (% of Reacted N) for Various Fuels

Time(sec)	$.9C_5H_5N/7O_2(.87)$[a] 900 C	950 C	$.5C_5H_5N/7O_2(.48)$ 900 C	950 C	$1HCN/.25C_6H_6/7O_2(.52)$ 900 C
0.5	6	12	13	24	5
0.75	14	27	--	--	--
1.0	20	69	13	32	6
1.5	10	54	--	56	--
2.0	7	44	9	44	5
4.0	--	6	12	24	3

	$.25HCN/.2C_6H_6/3.5O_2(.53)$			$2HCN/4CO/7O_2(.79)$		
	925 C	950 C	1000 C	800 C	900 C	1000 C
0.5	15	24	--	8	40	56
1.0	15	26	96	8	41	52
2.0	12	52	80	2	30	48
4.0	--	29	44	--	--	26

	$1HCN/6CO/12O_2(.40)$			$1HCN/8CO/12O_2(.48)$	
	700 C	800 C	900 C	700 C	800 C
0.5	2	29	70	7	46
1.0	4	62	66	27	80
2.0	2	56	56	70	69
4.0	--	20	20	1	27

(a) Reactant concentrations and (equivalence ratios) are the same basis as in Table 1

TABLE 3 Fuel Rich NO_x Yields (% Reacted N)

Time(sec)	$.65C_5H_5N/3.5O_2(1.25)$[a] 1000 C[b]	$1HCN/8CO/3O_2(1.92)$ 800 C	900 C
0.5	12	6	55
1.0	22	7	51
2.0	22	1	30
4.0	12	0.2	8
	$1HCN/4CO/2O_2(1.88)$	$1HCN/5CO/4O_2(1.06)$	
	1000 C	800 C	900 C
0.5	3	10	48
1.0	4	33	44
2.0	2	24	32
4.0	--	3	10

(a) See Table 1 footnote (a) for ER calculation
(b) Yields were negligible for this mixture at 900 C

TABLE 4 Equivalence Ratio Effects on NO_x/N_2O Yields

% C_6H_6[a]	ER	Yield NO_x/N_2O[b] Stirred (775 C)	Plug (800 C)
0	0.25	0.7/29	0.2/30
0.12	0.38	0.5/39	--
0.25	0.52	0.4/40	0.2/28
0.5	0.79	0.5/34	12/14
0.75	1.05	1.1/23	26/2
1.00	1.32	2.5/1.2	24/--

(a) Reactants are $1HCN/7O_2$ plus benzene in mole % - ER as in Table 1, footnote (a)
(b) Both stirred and plug flow reactors were used with one second contact time for all experiments

TABLE 5 Comparison of Plug and Stirred-Flow Data: NO/N_2O Yields in % Reacted Nitrogen

$1HCN/.25C_6H_6/70_2$[a]

Time(sec)	800 C		900 C		950 C	
	Plug	Stirred	Plug	Stirred	Plug	Stirred
0.25	40/13	--	39/22	--	39/10	10/--
0.5	16/25	n/45	16/22	5/41	29/13	15/--
1.0	n/30	n/40	3/45	6/39	10/15	46/--
2.0	n/34	n/43	n/8	5/33	1/11	28/--
4.0	n/28	n/40	n/8	3/31	n/5	11/--

$.5C_5H_5N/70_2$

	725 C	800 C		900 C		950 C	
	Plug	Plug	Stirred	Plug	Stirred	Plug	Stirred
0.25	--	56/6	--	--	--	56/6	--
0.5	n/n	34/18	n/--	42/12	13/28	40/8	24/--
1.0	4/3	9/33	--	18/24	13/30	19/13	32/--
2.0	3/32	n/37	--	4/26	9/30	5/10	44/--
4.0	5/43	n/40	--	--	12/26	1/5	24/--

$1HCN/4CO/60_2$[b]

	700 C		750 C		800 C	
	Plug	Stirred	Plug	Stirred	Plug	Stirred
0.25	40/5	--	--	--	35/1	--
0.5	17/11	n/--	21/7	1/37	32/3	9/13
1.0	3/26	n/28	21/11	2/37	16/22	33/18
2.0	n/32	n/27	n/14	1/40	n/36	23/22
4.0	n/22	n/25	n/--	--	n/23	2/22

(a) Compositions in mole %, n is for negligible amounts
(b) For CO added fuels below 700 C the HCN consumption dropped drastically and was time dependent, whereas, above 700 C the HCN was more than 90% consumed at all flow rates

TABLE 6 Low Temperature - Pyridine Oxidation (Plug Flow Reactor)
% Yields of HCN/N_2O

	$.5C_5H_5N/7O_2$[a]		
Time(sec)	750 C	725 C	
0.25	68/n	--	--
0.5	11/48	30/n	--
1.0	2/55	58/3	47/n
2.0	--	16/32	9/50
4.0	--	2/43	7/48
	800 C		
	NO_x high at .25 and .5 sec. HCN negligible at all flows		

(a) Concentrations in mole %

TABLE 7 N_2O Oxidation Data
% N_2O Reacted/NO_x Yield (% of Reacted N_2O)[a]

	$2.2N_2O/7O_2$[b]		$2.2N_2O/8CO/7O_2$		$2.2N_2O/.5C_6H_6/7O_2$
Time(sec)	900 C	1000 C	900 C	1000 C	1000 C
0.5	10/13	53/12	84/14	94/18	--
1.0	20/9	80/9	79/11	91/14	91/9
2.0	33/9	91/7	76/9	98/8	--
4.0	54/3	92/5	83/5	99/6	99/3

(a) Similar low yields of NO_x were found at 800 and 750
(b) Concentrations in mole %

TABLE 8 Solids Formation

%N-Fuel Reacted	Temperature (C)	Principal Solid Product
	$2HCN/8CO/7O_2$	
15	650	NH_4NCO
18	650	NH_4NCO
17	650	NH_4NCO
40	675	NH_4NCO
	$2HCN/4H_2/7O_2$	
50	650	Urea
29	700	Urea
20	600	NH_4NCO
	$2C_5H_5N/7O_2$	
97	750	NH_4NCO

Kinetics of the Reaction of NCO with Ethene and Oxygen Over the Temperature Range 295-662K*

Robert A. Perry

Sandia National Laboratories
Combustion Research Facility
Livermore, California 94550

Introduction

The NCO radical is intimately connected with nitric oxide formation from fuel-bound nitrogen in combustion systems.[1,2] In order to model nitrogen chemistry in combustion systems, it is essential to explore the possible chemical reactions that might enter into any extensive model of nitrogen chemistry in these systems. While little has been done toward understanding the detailed chemistry of the NCO radical with combustion species,[1-5] certain reactions can be anticipated to occur based upon analogous electrophilic radical/molecule reactions. One of these reactions is the reaction of NCO with ethene.

$$NCO + C_2H_4 + M \rightarrow \text{products} \qquad 1)$$

Unsaturated hydrocarbons are found extensively in combustion, with ethene being a major component after pyrolysis of larger fuels. This reaction was chosen to facilitate predictions of NCO radical reactions with unsaturated hydrocarbons and hence to understand more fully nitrogen chemistry in rich combustion systems. To the extent that this reaction occurs at combustion temperatures, it is a pathway to recycle reactive nitrogen radicals back into fuel-bound nitrogen i.e., HCN.

Other possible important reactions, if they occurred, are the exothermic reactions of NCO with oxygen.

$$NCO + O_2 \rightarrow NO + CO_2 \qquad 2a)$$
$$NCO + O_2 \rightarrow NO_2 + CO \qquad 2b)$$

Besides being of potential importance in combustion systems, these reactions could be important in atmospheric oxidation of HCN. An upper limit has been placed on the exothermic, although sterically restricted, reactions between NCO and oxygen.

In this paper current research that employs a laser photolysis/laser-induced fluorescence technique to measure absolute rate constants for the reaction of NCO radicals with ethene and oxygen over the

temperature range 295-662K is discussed. In addition, the pressure dependence of the reaction between NCO and ethene is explored at room temperature. The implications for combustion modeling will be addressed.

EXPERIMENTAL

The technique is essentially identical to that which was developed to study the products of the reaction of $O(^3P)$ with HCN.[6] NCO radicals are produced from the excimer laser photolysis of HNCO that was introduced along with the reactant of interest in a flowing gas mixture of HNCO:Ar:reactant at total pressures (primarily argon) of 10-372 Torr. The NCO radicals result either directly from the photolysis of HNCO or, as suggested by Drozdoski et al.[7], from the rapid reaction of $NH(^1\Delta)$ with HNCO. (Recent experiments at 157 nm and 193 nm suggest that the latter is the dominant mechanism.[8]) Both 193 nm and 157 nm radiation are used to photolyze HNCO in order to check for interference due to photolysis products.

An argon ion pumped ring dye laser, operating with stilbene-3 dye at 416.8 nm (100mW), is used to pump the $A^2\Sigma_{(1,0,0)} \leftarrow X^2\Pi_{(0,0,0)}$ transition of NCO. The resulting fluorescence is monitored using an EMI 9789QA photomultiplier tube fitted with an interference filter at 438.5nm (FWHM=8.0nm) mounted at right angles to the crossed laser beams. The intersection of the detection system aperture and the laser-induced fluorescence radiation defined a fluorescence viewing zone at the center of the reaction vessel whose cross section was ~2cm in diameter. This region was well separated from the reaction vessel walls, minimizing wall losses of the NCO radicals. The reactor consisted of a quartz reaction vessel enclosed in a ceramic furnace that could be heated to temperatures as high as 1200K. The temperature of the furnace was monitored by Chromel/Alumel thermocouples mounted inside the reaction vessel, with the temperature of the vessel maintained to ±5K over the entire temperature range.

The HNCO was synthesized according to the procedure of Okabe.[9] Cyanuric acid was heated in an evacuable pyrex vessel to 400K. The HNCO generated was passed through a P_2O_5 and Ag_2O trap to remove the water, and HCN and was then condensed in a liquid nitrogen trap. The liquid was vacuum distilled using a dry-ice/acetone trap until constant vapor pressure (0.88 Torr) resulted. Argon was bubbled through the liquid and the resulting Ar/HNCO mixture was flowed to the reaction vessel. The flow rate was monitored by use of a rotameter. All other flows were monitored by the use of Tylan flow controllers that were calibrated prior to use.

The excimer laser intensity was varied by a factor of 2 using a purge tube situated between the excimer laser and the reaction vessel. Mixtures of nitrogen and oxygen were used to attenuate the 157 nm radiation, while nitrous oxide and air were used to attenuate radiation at 193 nm. All experiments were performed at a repetition rate of 0.3Hz. Signals were obtained by photon counting in conjunction with multichannel scaling. Decay curves of NCO radicals were accumulated from 25-500 pulses

depending on the signal strengths. NCO half-lives ranged from 2.43-200 msec, and the NCO radical concentrations were followed for at least three half-lives.

All experiments were carried out under slow-flow conditions so that the premixed reactant gas mixture could be replenished between laser pulses, thereby avoiding the accumulation of photolysis or reaction products. The partial pressure of HNCO was approximately 1.8-19 mTorr. The gases used had the following purity levels according to the manufacturer: Ar ≥99.995%; C_2H_4≥99.0%; O_2 ≥99.9995%.

RESULTS AND DISCUSSION

Over the entire temperature range 295-652K, and in the presence of excess reactant gas, pseudo-first order kinetics is observed, and the bimolecular rate constant is obtained using the expression:

$$\ln [NCO]_o / [NCO]_t = \ln S_o/S_t = (k_o + k_i [Reactant])(t-t_o)$$

Here $[NCO]_o$ and $[NCO]_t$ are the concentrations of NCO radicals at times t_o and t, respectively, S_o and S_t are the corresponding fluorescence intensities, k_o is the first order rate coefficient for removal of the NCO in the absence of added reactant, and k_i is the rate constant for reaction with the added reactant, i.e., ethene or oxygen.

The decay was analyzed following a ~1 ms delay after the excimer laser pulse to minimize interference from laser-induced emission from the silica vessel and to ensure that secondary reactions of other radical species formed during the photolysis event, such as $NH(^1\Delta)$ would not interfere with the reaction of interest.[7] In all experiments exponential decays were observed after the first millisecond supporting the contention that secondary reactions were not important. Also, at low pulse energies (≤.1mJ/pulse) no effect, within experimental uncertainty, due to laser intensity was observed with a factor of two change. (Without attenuating the excimer laser radiation the apparent rate was measured to be faster and decays were nonexponential.)

The data were analyzed by numerical least squares fitting of the decays. The measured decay rates were found to depend linearly on the concentration of added reactant for fixed total pressure and temperature. The absolute rate constants were determined by plotting the measured decay rate against reactant concentration and performing a least squares fit to obtain the slope, k_i.

Rate constants, k_1, for the reaction of NCO with ethene were determined over the temperature range of 295-652K with the total pressure being varied from 10-372 Torr at 295K. Figures 1 and 2 show the plots of the data at 295K and higher temperatures, respectively, while Figure 3 shows a plot of the pressure dependence. Table I gives the rate constants determined for this reaction by least squares analysis over the entire temperature range.

Figure 4 shows an Arrhenius plot of the rate constants k_1 with the region from 295-447K being described by the following Arrhenius expression:

$$k_1 = 3.0 \times 10^{-12} e^{(230 \pm 300)/RT} \text{ cm}^3 \text{ molecule}^{-1} \text{s}^{-1},$$

where the error limit in the activation energy is the estimated overall error limit.

The pressure dependence observed at 295K (figure 3) is best explained by a Lindemann mechanism.

$$NCO + C_2H_4 \underset{\leftarrow}{\rightarrow} complex^* \qquad (a,-a)$$

$$complex^* + M \rightarrow complex + M \qquad (b)$$

where complex* is the complex formed by the terminal addition of NCO to ethene. The pressure dependent rate is given by the expression:

$$k_{bi} = k_a k_b[M] / (k_{-a} + k_b[M])$$

In the high pressure region where $k_b[M]$ is much greater than k_{-a}, $k_{bi} = k_a$, while in the low pressure region $k_{bi} = k_a(k_b[M]/k_{-a})$.

At temperatures greater than 447K a dramatic reduction in the bimolecular rate constant was observed. As seen in Figure 4 the reaction rate drops by greater than two orders of magnitude from 447K to 652K. This reduction in bimolecular rate constant apparently occurs due to the very rapid decomposition of the complex formed between NCO and ethene. Although such a dramatic reduction in reaction rate has been observed in the past for OH radical reactions,[10-14] nonexponential decays (after 1ms) were not apparent in these experiments. The absence of nonexponential decays suggest that the life time of the complex formed must be short in comparison to the experimental observation time. A proposed reaction mechanism whereby the thermalized adduct, [complex], begins to dissociate on a time scale that is comparable to the time frame of the experiments, analogous to the explaination of the effect observed for OH radical reaction with unsaturated hydrocarbons,[10-14] could explain the sharp drop in rate with increasing temperatures ($\geq$ 447K), but in order to explain fully the essentially exponential decays observed in all of the experiments, competitive reactions that turn off at higher temperatures (or a different reaction mechanism that regenerates NCO radicals at higher temperatures) is required. Calculations are presently under way to address the possible alternate channels, such as ring closure to form the ethylene imine analog.

Using 193nm photolysis of HNCO, with a mixture of nitrous oxide and oxygen as a UV attenuator/filter, the reaction of NCO with oxygen was not observed to occur at room temperature and 372 Torr argon with

2.27×10^{16} molecule/cm^3 of oxygen added. In addition no reaction was observed at 662K and 389 Torr when 2.4×10^{16} molecule/cm^3 of oxygen was added. From these data the rate of reaction with oxygen was estimated to be less than 1×10^{-16} cm^{3}molecule^{-1} s^{-1} at 295 and less than 5×10^{-17} cm^{3}molecule^{-1} s^{-1} at 662K. These data suggest that under the conditions that exist in combustion environments or in the stratosphere, it is unlikely that the reaction of NCO with oxygen will be important. As suggested by Cicerone and Zellner[15], the primary fate of NCO in the atmosphere is most likely photolysis at wavelengths less than 300 nm.

CONCLUSIONS

At low temperatures the NCO radical will react with ethene to form a complex. At temperatures greater than 450K a marked decrease in the rate of reaction occurs until finally at 650K the reaction has decreased by two orders of magnitude. This effect suggests that the reaction with ethene, or, by inference, other unsaturated hydrocarbons, will not serve to recycle the NCO radical in combustion environments.

At the temperatures of this study NCO radicals do not react with molecular oxygen. The reaction of NCO with oxygen should be unimportant in combustion or atmospheric systems.

ACKNOWLEDGEMENT

This work was supported by the U. S. Department of Energy, Office of Basic Energy Sciences. I would like to thank Mark Jaska for his assistance in carrying out the experiments.

Table I. Rate constants, k_1 for the reaction of NCO radicals with ethene. The indicated error limits are the estimated overall error limits; they include the least squares standard deviations (2.0-15%), as well as the estimated accuracy limits of other parameters such as pressure and reactant concentrations.

Temperature (K)	Total Pressure (Torr)	$k_1 \times 10^{12}$ (cm^3 molecule^{-1} s^{-1})
295	10.5	3.37 ± 0.57
295	25.0	3.78 ± 0.38
295	53.3	4.37 ± 0.44
296	102.0	4.39 ± 0.44
296	204.0	4.58 ± 0.46
295	372.0	4.69 ± 0.47
330	198.0	4.00 ± 0.40
381	203.0	3.99 ± 0.40
447	200.0	3.88 ± 0.39
487	202.0	2.56 ± 0.64
535	201.0	1.30 ± 0.26
585	372.0	0.112 ± 0.02
652	372.0	0.027 ± 0.005

REFERENCES

1. J. A. Miller, M. C. Branch, W. J. McLean, D. W. Chandler, M. D. Smooke, and R. J. Kee, 20th Symposium (International) on Combustion, The Combustion Institute, 673 (1985).
2. R. A. Perry, J. Chem. Phys.,84 5485 (1985).
3. M. Y. Louge and R. K. Hanson, 20th Symposium (International) on Combustion, The Combustion Institute, 665 (1985).
4. M. Y. Louge and R. K. Hanson, Combustion Flame 58,291 (1984).
5. J. L. Cookson, G. Hancock, and K. G. McKendrick, Ber. Bunsenges. Phys. Chem. 89, 335 (1985).
6. R. A. Perry and C. F. Melius, 20th Symposium (International) on Combustion, The Combustion Institute, 639 (1985).
7. W. S. Drozdoski, A. P. Baronavski, and J. R. McDonald, Chem. Phys. Letts., 64 421 (1979).
8. T. Spiglanin, R. A. Perry, D. W. Chandler, private comunication.
9. H. Okabe, J. Chem. Phys., 53 3507 (1970).
10. R. A. Perry, R. Atkinson, J. N. Pitts, Jr., J. Phys. Chem. 81 296 (1977).
11. R. A. Perry, R. Atkinson, J. N. Pitts, Jr., J. Phys. Chem. 81 1607 (1977).
12. F. P. Tully, A. R. Ravishankara, R. L. Thompson, J. M. Nicovich R. C. Shah, N. M. Kreutter and P. H. Wine, J. Phys. Chem. 85, 2262 (1981).
13. F. P. Tully, Chem. Phys. Letts., 96 148 (1983).
14. K. Lorenz, and R. Zellner, Ber. Bunsenges Phys. Chem. 87, 629 (1983).
15. R. J. Cicerone, and R. Zellner, J. Geophys. Research, 88 10,689 (1983).

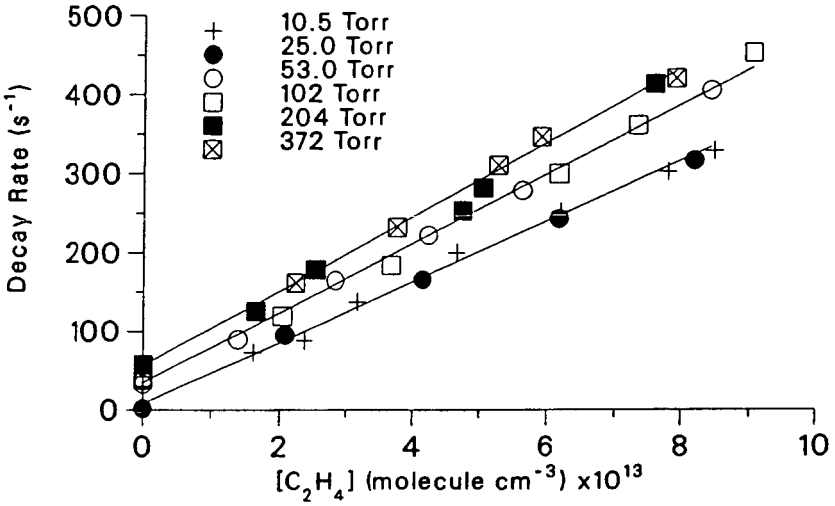

Figure 1. Plots of the decay rate against ethene concentration for the reaction on NCO with ethene at 295K. The solid lines represent best fit to data at 25 Torr, 53 Torr and 372 Torr.

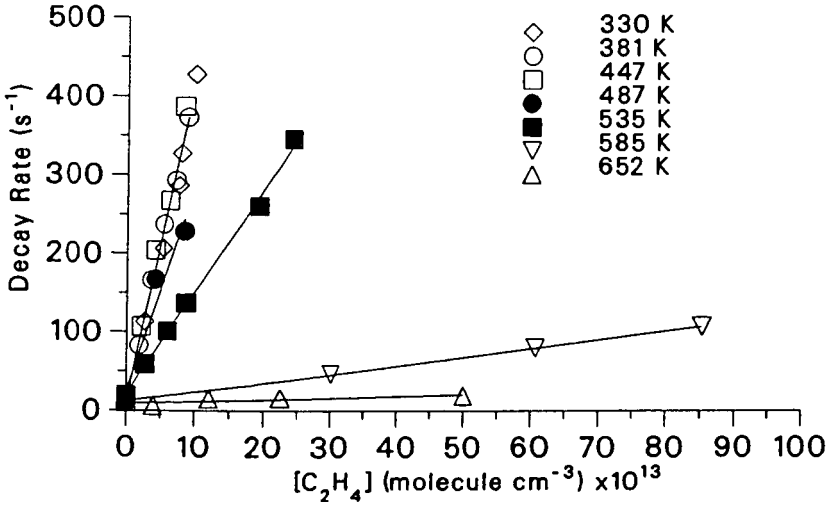

Figure 2. Plots of the decay rate against ethene concentration.

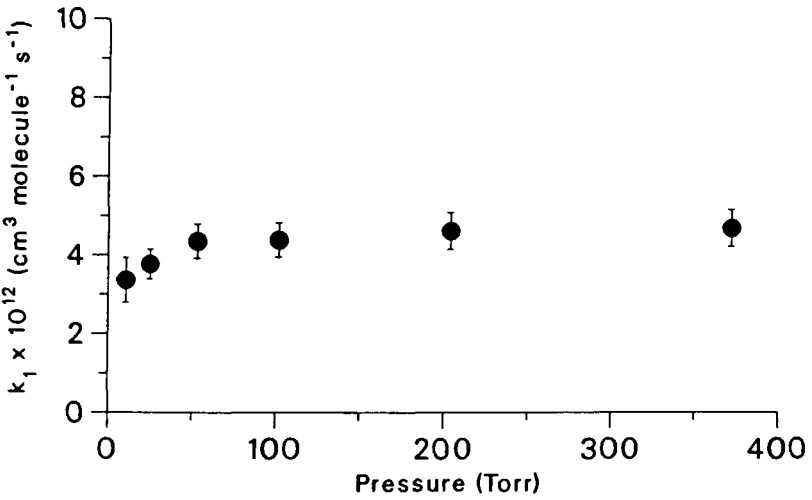

Figure 3. Plot of the rate constant versus pressure at room temperature.

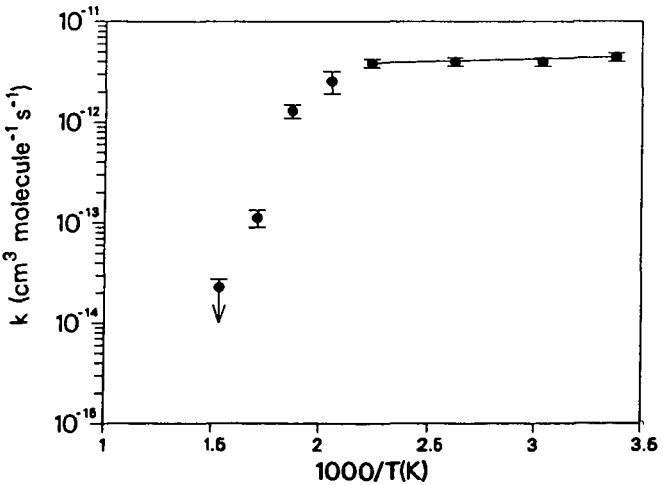

Figure 4. Arrhenius plot of log k_1 for the reaction of NCO with ethene against 1000/T(K). The solid line is the least squares fit to the data for the temperature range 295-447.

Pyrolysis of C_6H_6

by

M. B. Colket, III

United Technologies Research Center
Silver Lane, East Hartford, CT 06108

Introduction

Several mechanisms for the pyrolysis of benzene at elevated temperatures have been previously proposed. Unfortunately, none of these mechanisms is entirely satisfactory when both experiments and thermodynamics are considered. Yet, knowledge of benzene decomposition will increase the understanding of the breakup and formation of other aromatic compounds. Consequently, a single-pulse shock tube (SPST) investigation of the pyrolysis of benzene has been performed over the temperature range of 1200 to 2400K. In addition, thermochemical estimates and detailed chemical kinetic modeling have been performed to evaluate the previously proposed mechanisms for benzene pyrolysis.

Description of Facilities and Model

The 3.8 cm (i.d.) single-pulse shock tube (SPST) used in this experiment utilizes the "magic hole" technique for quenching pyrolyzed samples at rates above 10^5 K/sec. SPSTs were developed by Glick, Squire, and Hertzberg (1) and the UTRC facility has been described by Colket (2). Gas samples, after dwell times of approximately 700 microseconds, were automatically collected and analyzed for reactant and products using heated gas sampling valves and a Hewlett Packard 5880A gas chromatograph. With a CP Sil 5 CB (from Chrompack, Inc.) capillary column and a silica gel packed column, H_2 and hydrocarbons up to C_{10} were identified and quantitatively analyzed.

Argon (99.999% pure) was obtained from Matheson and LC-grade benzene was obtained from the Burdick and Jackson Laboratory. The initial mixture concentration was 130 ppm benzene in argon and was prepared gravimetrically. Gas chromatographic analysis indicated that impurities included unidentified C_5, C_6 and C_7 hydrocarbons as well as toluene, although the total concentration of impurity was less than 0.2% of the initial benzene.

Detailed chemical kinetics calculations are performed using CHEMKIN(3), LSODE (4), and a version of a shock tube code (5) which has been modified to include the quenching effects in a SPST. Quenching rates varied with shock strength and were calculated using measured pressure traces and assuming isentropic expansion. The modified code also allows monitoring of time-dependent contributions from each reaction to the formation and/or destruction of each species.

Proposed Mechanisms

Mechanisms for the decomposition of benzene are listed in Table I. It is important to note that most are not single-step mechanisms. Radical intermediates equilibrate rapidly and their concentrations are sufficiently low to render them (nearly) undetectable in many systems. Experimental results from the present and previous high temperature works (6,7) suggest that primary stable products are acetylene, diacetylene, and hydrogen and the initial production rate of acetylene is two to three times higher than that of diacetylene. Unfortunately, this information is of minimal use in sorting out the mechanisms since benzene pyrolyzes at high temperatures (relative to pyrolysis temperatures of other hydrocarbons) and all intermediates shown in Table II rapidly pyrolyze to the approximate mixture of acetylene and diacetylene that has been observed.

Mechanism A is the generally accepted reaction sequence; however, only Reaction 1 is understood. The breaking of the C-H bond is believed to be the initiation step in both pyrolytic and some oxidation studies. Its rate has been determined from D-atom production (in pyrolysis of C_6D_6) (8) and from detailed modeling studies of both pyrolysis (9) and oxidation (10). An RRKM fit has been performed by Kiefer, et al (9) using available experimental data and is consistent with thermodynamics. Their k_1^{∞}, is given by $10^{17.3}$ exp(-118 kcal/RT) sec^{-1}. Knowledge of the mechanism for phenyl decomposition is substantially less than that for Reaction 1. Some information is available on the overall rate, k_3; yet the details of the ring fracturing process have not been defined. The thermochemical estimate by Fujii and Asaba (11) has been until recently the most often quoted rate for this process. More recent modeling (8,9) of benzene pyrolysis has produced similar rates as Ref.11; however, since Reaction 1 is rate limiting over most of the temperatures regimes examined, the modeling results for k_3 are expected to be lower limit estimates with large uncertainties in the temperature dependence. The Fujii and Asaba (11) estimate, $k_3 = 3.16 \times 10^{14}$ exp (-86 kcal/RT) sec^{-1}, was based on an "old" value for the heat of formation for i-C_4H_3 of 102 kcal/mole (12); however, more recent estimates using group additivity (13) and BAC-MP4 (14) techniques fix this value closer to 115 kcal/mole. In addition, n-C_4H_3, which has a ΔH_f of 126 kcal/mole, is the preferred isomer for phenyl decomposition. Consequently, Reaction 3 is over 100 kcal/mole endothermic. If this process involves direct C_2H_2 elimination, then the previous modeling efforts that produced lower limit rates strongly suggest that the high pressure A-factor is at least $10^{17.8}$. This value is orders of magnitude higher than what would be expected for this multibond process. Consequently, it must be assumed that Reaction 3 represents an overall process or that processes involving radicals other than, or in addition to, phenyl are important to benzene decomposition.

One alternative route for benzene decomposition is direct C_2H_2 elimination (Mechanism B) and has received recent support (6,8); however, Kiefer, et al (9) have shown it is not necessary to invoke this step to describe experimental profiles. In addition, it should be noted that the direct elimination is a multibond process which should be unlikely, and presumably involves the intermediate formation of the C_4H_4 diradical. For this intermediate, the effective activation barrier to Reaction 4 may be as high as 180 kcal/mole.

Another possible pyrolysis route involves the production of benzyne, which subsequently decomposes. Unimolecular decomposition of phenyl (Reaction 5) to benzyne is endothermic by 93 kcal/mole, which is nearly as much as Reaction 3. Similar thermochemical arguments can eliminate this decomposition route. The other route, Reaction 6, is a radical termination step and would produce an overall slowing of benzene pyrolysis. Knudsen cell pyrolysis experiments (7) have shown the formation of a C_6H_4 compound. Assuming this compound is benzyne or another product of phenyl decomposition, Smith and Johnson (7) argued that C_6H_4 is an important intermediate during benzene decomposition, especially at elevated temperatures. At least some of the product, however, may be composed of the chained isomers of C_6H_4. These isomers may be produced via hydrogenation of triacetylene, which was also observed in significant concentrations. Consequently, no clear evidence of the importance of Mechanism C is apparent.

Mechanism D appears to be very attractive, since an extrapolation of the rate coefficient (15) for H-atom addition to benzene (Reaction 8) is approximately an order of magnitude higher (Ref. 9) than H-atom abstraction (Reaction 2) at 1600 K. The addition reaction, however, competes with its reverse reaction. Using thermodynamics for c-C_6H_7 derived from measurement of the forward and reverse rates of Reaction 8 (15), Mechanism D can be shown to have a negligible impact on benzene pyrolysis. However, a different set of thermodynamics for c-C_6H_7 reported in Ref. 15 suggests that Mechanism D may play an important role at low temperatures. Detailed modeling calculations using Mechanism D were limited, due to what appears to be rather large uncertainties in both the heat of formation and entropy. Nevertheless, there are attractive features of this decomposition mechanism, especially at low temperatures, and it should be explored further. It is worth noting that Reaction 8 is not sufficiently energetic (only 16 to 26 kcal), that it can be followed immediately by Reaction 9 (71-81 kcal required). Instead, c-C_6H_7 will collisionally thermalize prior to its decomposition to products. Only a minimal acceleration in rate due to the formation of an excited complex can be expected. Further exploration of this route (Mechanism C) should be performed.

With no fully satisfactory alternatives, and the expectation that phenyl must decompose to aliphatics at sufficiently elevated temperatures (when production of phenyl via Reaction 1 is fast), it is prudent to re-examine Mechanism A. One can separate Reaction 3 into the following sequence:

$$C_6H_5 \leftrightarrow 1\text{-}C_6H_5 \qquad 3a$$

$$1\text{-}C_6H_5 \rightarrow n\text{-}C_4H_3 + C_2H_2 \qquad 3b$$

This sequence is the reverse of the processes suggested for the formation of phenyl during acetylene pyrolysis (17) and has been shown to compare favorably with recent experimental data (2). If one assumes that the ring breaks at the single bond as shown

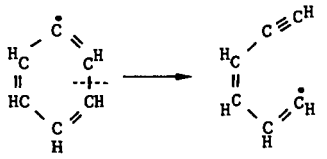

then this is a relatively straightforward process analogous to the decomposition of nC_4H_5; i.e. $CH{:}CH.CH{:}CH_2 \rightarrow C_2H_2+C_2H_3$. Breakage of either of the other two single-bonds would require a more complex process involving H-atom shifting or the formation of energetic intermediates. The resultant linear compound would be expected to decompose to acetylene and $n\text{-}C_4H_3$ or re-cyclize to phenyl. Detailed chemical modeling was performed using the reaction sequence in Table II coupled with an acetylenic mechanism similar to that reported (17, 18). A comparison of the model and single-pulse shock tube data is presented in Figure 1 for a series of shocks at an initial concentration of 130 ppm benzene in argon. In this figure, final concentrations produced after a dwell time of 700 microseconds followed by quenching are plotted as a function of initial post-shock temperature. Total pressure for these experiments is approximately seven atmospheres.

The comparison is quite reasonable. The higher fractional decomposition at low temperatures observed in the experiment may be due to impurities from the wall initiating the reaction at low temperature. The residual benzene observed experimentally at elevated temperatures may be caused by sampling a portion of the boundary-layer near the walls of the shock tube. The mechanism proposed in Table II is essentially consistent with Kiefer et al's except that Reaction 3 has been separated to 3a and b. An effective rate constant for Reaction 3 can be estimated by assuming a steady-state concentration for $1\text{-}C_6H_5$, i.e.

$$[\ell\text{-}\ C_6H_5]_{s.s.} = \frac{k_{3a}[C_6H_5]}{(k_{-3a}+k_{3b})}$$

$$\text{therefore } k_{3}^{\text{effective}} = \frac{k_{3a}\ k_{3b}}{k_{-3a}+k_{3b}}$$

This curved evalution is depicted as a solid line in Fig. 2 over the temperature regime where sensitivity to this rate was observed. The curve is extrapolated to both low and high temperatures to facilitate comparisons to other evaluations. The relatively high values obtained in this work for k_1 and $k_3^{\text{effective}}$ are not surprising since the rate constant determined in these experiments are expected to be close to the high pressure limiting value.

Conclusions

Previously proposed mechanisms for the pyrolysis of benzene at high temperatures have been reviewed using detailed chemical modeling and a brief thermochemical examination. The most widely accepted sequence, $C_6H_6 \rightarrow C_6H_5(+H) \rightarrow C_4H_3+C_2H_2$, is slightly modified to $C_6H_6 \rightarrow C_6H_5(+H) \rightarrow 1\text{-}C_6H_5 \rightarrow n\text{-}C_4H_3+C_2H_2$ and the structure of the linear C_6H_5 intermediate is proposed. Forward and reverse rates are consistent with thermochemistry and experimental data. A benzene decomposition route involving $c\text{-}C_6H_7$ and $1\text{-}C_6H_7$ was examined, yet sufficiently accurate thermochemistry was not available to reach final conclusions.

Acknowledgements

This work has been supported by the Air Force Office of Scientific Research (AFSC) under Contract No. F49620-85-C-0012. The United States Government is authorized to reproduce and distribute reprints for governmental purposes notwithstanding any copyright notation hereon.

References

1. Glick, H. S., Squire, W., and Hertzberg, A., Fifth Symnposium (International) on Combustion, p. 393, Reinhold Publishing Corp., New York, 1955.
2. Colket, M. B., To be published in Proceedings of the Fifteenth International Symposium on Shock Waves and Shock Tubes, 1986.
3. Kee, R. J., Miller, J. A., Jefferson, T. H., "CHEMKIN: A General Purpose, Problem-Independent, Transportable, Fortran Chemical Kinetics Code Package," Sandia Laboratories, SAND80-8003, March, 1980.
4. Hindmarsh, A. C., "LSODE and LSODI, Two New Initial Value Differential Equation Solvers," ACM SIGNUM Newsletter, 15, No. 4, December 1980.
5. Mitchell, R. E. and Kee, R. J., "A General-Purpose Computer Code for Predicting Chemical Kinetic Behavior Behind Incident and Reflected Shocks", Sandia National Laboratories, SAND82-8205, March 1982.
6. Kern, R. D., Wu, C. H., Skinner, G. B., Rao, V. S., Kiefer, J. H., Towers, J. A., and Mizerka, L. J., Twentieth Symposium (International) on Combustion, The Combustion Institute, p. 789, Pittsburgh, 1984.
7. Smith, R. D. and Johnson, A. L., Combustion and Flame 51, 1 (1983).
8. Rao, V. S. and Skinner, G. B., J.Phys.Chem. 88, 5990 (1984).
9. Kiefer, J. H., Mizerka, L. J., Patel, M. R., and Wei, H. C., J.Phys.Chem. 89, 2013 (1985).
10. Hsu, D. S. Y., Lin, C. Y. and Lin, M. C., Twentieth Symposium (International) on Combustion, The Combustion Institute, p. 623, Pittsburgh, 1985
11. Fujii, N. and Asaba, T., Fourteenth Symposium (International on Combustion, p. 433, The Combustion Institute, Pittsburgh, 1973.
12. Duff, R. E., and Bauer, S. H., J. Chem. Phys. 36, 1754 (1962).
13. Benson, S. W., Thermochemical Kinetics, 2nd Ed., John Wiley and Sons, New York, 1976.
14. Melius, C., personal communication.
15. Nicovich, J. M. and Ravishankara, A. R., J. Phys. Chem. 88, 2534 (1984).
16. Weissman, M. and Benson, S. W., Int'l. J. Chem. Kin. 16, 307 (1984).
17. Frenklach, M., Clary, D. W., Gardiner, W. C., Jr., and Stein, S., Twentieth Symposium (International) on Combustion, p. 887, The Combustion Institute, Pittsburgh, 1985.
18. Kiefer, J. H., Kapsalis, S. A. Al-Alami, M. Z., and Budach, K. A., Combust. Flame 51, 79 (1983).

TABLE I
Previous Mechanisms for
Benzene Pyrolysis

A	$C_6H_6 \rightarrow C_6H_5+H$	(1)
	$H+ C_6H_6 \rightarrow C_6H_5+H_2$	(2)
	$C_6H_5 \rightarrow C_4H_3+C_2H_2$	(3)
B	$C_6H_6 \rightarrow C_4H_4+C_2H_2$	(4)
C	$C_6H_5 \rightarrow C_6H_4+H$	(5)
	$H+ C_6H_5 \rightarrow C_6H_4+H_2$	(6)
	$C_6H_4 \rightarrow C_4H_2+C_2H_2$	(7)
D	$H+ C_6H_6 \rightarrow c\text{-}C_6H_7$	(8)
	$c\text{-}C_6H_7 \rightarrow 1\text{-}C_6H_7$	(9)
	$1\text{-}C_6H_7 \rightarrow n\text{-}C_4H_5+C_2H_2$	(10)

TABLE II
Proposed Reaction Sequence
for Benzene Pyrolysis

		Forward rate		Reverse Rate		
		$\log_{10}A$	E cal/mole	$\log_{10}A$	n	E cal/mole
1.	$C_6H_6 \rightleftarrows C_6H_5+ H$	16.18	107,900.	10.05	0.98	-5690.
2.	$H+C_6H_6 \rightleftarrows C_6H_5+ H_2$	14.40	16,000.	8.35	1.12	6420.
3a.	$C_6H_5 \rightleftarrows \ell\text{-}C_6H_5$	14.00	65,000.	13.11	-0.68	3300.
3b.	$\ell\text{-}C_6H_5 \rightleftarrows n\text{-}C_4H_3+C_2H_2$	15.34	38,000.	5.97	1.97	-3610.
11.	$n\text{-}C_4H_3 \rightleftarrows H+C_4H_2$	12.43	37,000.	11.29	0.44	-2790.
12.	$n\text{-}C_4H_3 \rightarrow C_2H+C_2H_2$	14.60	54,000.	7.89	1.66	-3120.
13.	$C_2H+C_6H_6 \rightarrow C_2H_2+C_6H_5$	13.30	0	12.00	0	12520.

FIGURE 1. 130PPM BENZENE PYROLYSIS
COMPARISON OF MODEL AND EXPERIMENT

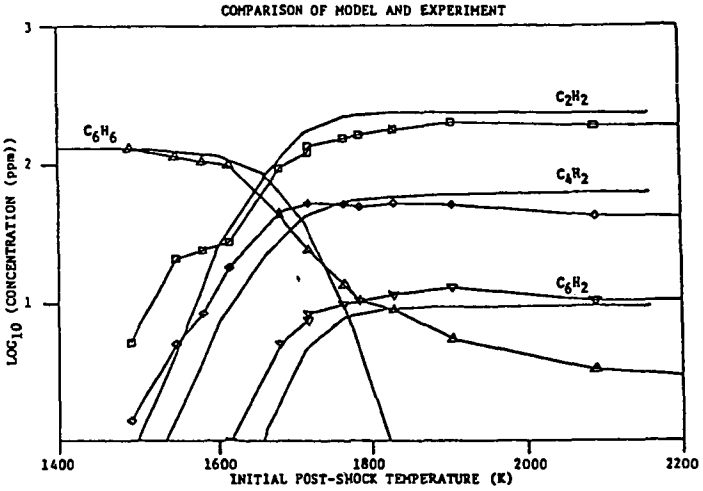

FIGURE 2. ARRHENIUS PLOT OF k_3

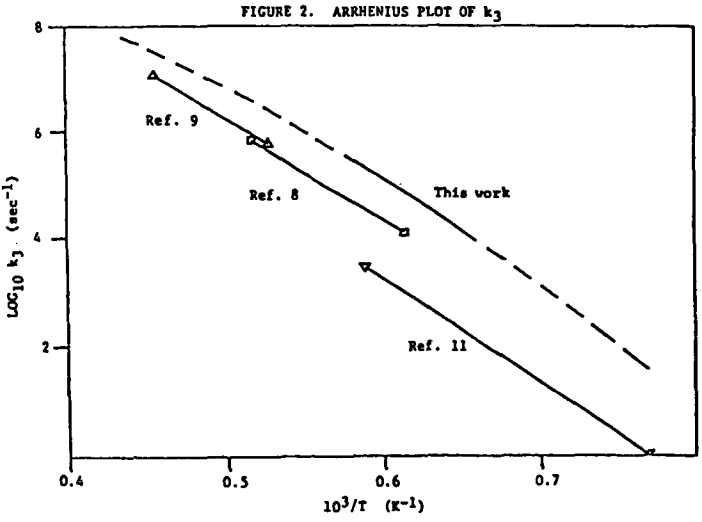

The Chemical Structure of Methane/Air Diffusion Flames: Concentrations and Production Rates of Intermediate Hydrocarbons.

J. Houston Miller

Department of Chemistry
George Washington University
Washington, DC 20052

and Kermit C. Smyth

Center for Fire Research
National Bureau of Standards
Gaithersburg, MD 20899

INTRODUCTION:

The production of intermediate and large hydrocarbon species is common to most combustion systems. These products range in size from acetylene, benzene and polynuclear aromatic hydrocarbons (PAH) to very large soot particles. Radiation from particles is the dominant mode of heat transfer in large fires. In addition, sampled particles often have PAH adsorbed onto them. Many of these molecules are known carcinogens and their presence on inhalable soot particles poses an obvious long-term health hazard. Despite the important role that such species play in flames and the danger they present as combustion byproducts, the mechanism for their formation is as yet unknown.

Extensive profile studies have led to a detailed understanding of the chemical structure of premixed flames [1]. This information has been combined with the time-temperature history in these one-dimensional systems to produce simple models for the condensation chemistry of premixed flames. Modelling efforts have also been undertaken in shock tubes, although the data set available as input has generally been less extensive [2,3]. Despite the significant progress towards an understanding of soot formation which has resulted from these studies, most practical combustion devices are diffusion flames, and chemical stucture data for these environments has only recently been available. Workers in this [4] and other [5] laboratories have recently reported concentration measurements for molecular species, including intermediate hydrocarbons, in laminar diffusion flames. Our work has shown that a knowledge of the local chemical composition alone is not sufficient to predict the concentrations of PAH and soot. We have therefore also collected profile data for temperature and convective velocity in our flame system. In this paper, results for the chemical structure of a methane/air diffusion flame are reviewed. Species concentrations are combined with profiles of velocity and temperature to calculate production rates for intermediate hydrocarbons. The relevance of these calculations to an understanding of soot formation chemistry is discussed.

EXPERIMENTAL APPROACH:

The experimental system has been described in detail elsewhere [4], and will be discussed only briefly below. Laminar methane/air diffusion flames were burned at atmospheric pressure on a Wolfhard-Parker slot burner. Fuel exits a central 8mm wide slot and air flows through two 16mm wide adjacent slots. Thus, two flame sheets are formed near the fuel/air interfaces, which are symmetric about the burner centerline. The flame is stabilized by wire screen "gulls" located 45mm above the burner surface. Concentration profiles of numerous stable flame species were collected via a direct-sampling mass spectrometer equipped with a quartz microprobe [6]. Calibrations were perfomed by measuring the signal for a particular molecule sampled from a mixture of known composition of the species with argon at room temperature. Calibration factors were then corrected for the variation of the mass flow through the sampling orifice as a function of temperature. For species which could not be calibrated directly, factors for similar species were adjusted by multiplying by the ratio of their respective ionization cross-sections.

Temperature profiles were measured with an uncoated fine wire Pt/Pt-10%Rh thermocouple. Corrections due to radiation effects are less than 7% at the highest temperatures in this flame [4], while catalytic effects are expected to be small [7] and in the opposite direction. Horizontal and vertical components of the convective velocity were determined using laser Doppler velocimetry. These measurements were made by seeding the flow with nominal 1 μm diameter aluminum oxide particles. The temperature and velocity profiles were obtained at heights ranging from near the burner surface to 20 mm above the burner. Mass spectrometric measurements were limited to a minimum height of 3 mm above the burner (due to the 6mm diameter of the microprobe) and a maximum height of 15 mm above the burner. Above 15 mm, clogging of the probe orifice by soot particles was observed and quantitative sampling was no longer possible. The gradients in concentration and temperature in this flame are steepest in the horizontal direction. Therefore, profile data points were collected every 0.2 mm in the lateral direction and every 2 mm in the vertical direction.

RESULTS:

Figure 1 illustrates the temperature and velocity fields for this flame. Shown in solid lines are isothermal contours determined from the thermocouple profles. Note the bowing out of the flame along the 1900 K contour away from the slot separators located at ±4 mm with respect to the burner centerline. Also shown are streamlines of convective velocity calculated from the two measured velocity components. The streamlines exhibit trajectories which begin in the lean region of the flame, cross the high temperature reaction zones, and continue into the fuel-rich regions.

Figure 2 shows mass-spectrometric profiles of the concentrations of a variety of stable flame species at a height of 9 mm above the burner. A number of points are noteworthy in comparing

Figures 1 and 2. First, the concentrations of oxygen and methane disappear near the high temperature reaction zone at ±6 mm from the burner centerline, where the concentration of water is at a maximum. Second, the high concentration of nitrogen near the burner centerline reveals that significant entrainment of air (as shown by the velocity measurements in Fig. 1) and diffusion of nitrogen toward the burner centerline occur. Also shown in Fig. 2 is a summation of mole fractions for all species present in the flame at a concentration of 1% or greater. The close agreement to an ideal mass balance of 1 throughout the flame is a measure of the success of our calibration scheme.

Figure 3 illustrates profiles collected at 9mm above the burner surface for a variety of intermediate hydrocarbons: acetylene, benzene, diacetylene, and butadiene. Peak concentrations at this height for these species are 6200, 800, 570, and 110 parts per million, respectively. Profiles for a large number of additional intermediate hydrocarbons were obtained, and all have concentration maxima in the same region of the flame.

DATA ANALYSIS

One of the primary goals of our work is the application of kinetic modelling to a methane/ air diffusion flame. The approach we have adopted is to compare the predictions of models which have been used successfully in premixed flames and shock tubes with our experimental results. A successful model must not only account for the steady state concentrations of species involved in the soot formation process, but also for the net rate of reactions for these species in the flame. Therefore, as a first step in the application of detailed kinetic modelling to our flame we have sought to derive the net chemical flux for profiled species from our concentration, temperature and velocity measurements. The procedure for this calculation is described below.

A laminar flame is a steady-state system: the value of any macroscopic variable (such as a species concentration) does not change with time at a particular spatial location [6]. Because there is a flux into and out of a given volume element due to mass transport, there must be a corresponding change in the species concentration due to chemical reactions:

$$R_i = \nabla[N_i\ (v + V_i)] \qquad 1)$$

Here, R_i is the net chemical rate, N_i is the species concentration, v is the mass average (convective) velocity, and V_i is the diffusion velocity of the species into the local mixture. This diffusion velocity can be calculated by first computing the effective diffusion coefficient, $D_{i,mix}$, where contributions from all species present in the flame with a concentration greater than 1 % are included:

$$V_i = - \frac{D_{i,mix}}{X_i} \cdot \nabla x_i \quad . \qquad 2)$$

Figure 4 illustrates this calculation for acetylene production rates at a height of 9mm above the burner. Contributions from the convective and diffusive velocities to the net chemical rates are shown. Note the strong diffusive velocity away from the burner centerline into the high temperature reaction zone, where acetylene is oxidized. Figure 5 indicates that the chemical role of acetylene changes with height above the burner. Low in the flame the destruction rate exhibits a maximum value (R_i =-1.0x10^{19} molecules/(cc·sec)) near the high temperature, primary reaction zone, and the production rate feature (R_i = 1.5x 10^{19} molecules/(cc·sec)) occurs slightly toward the fuel side. This peak in the production rate is located on the high temperature side of the observed maximum in the concentration profile (see Fig. 3). Higher in this flame it appears that the production rate peak is diminished by a new destruction feature (see arrow in Figure 5). An additional loss mechanism for acetylene higher in the flame is consistent with the proposed importance of this intermediate hydrocarbon in particle growth chemistry. The location of this new feature coincides with the peak concentrations of very small soot particles detected in our earlier work [4].

CONCLUSIONS AND FUTURE DIRECTIONS:

We have made quantitative species concentration measurements and analyzed these profile data to obtain chemical rates for production and destruction of intermediate hydrocarbons in a methane/air flame. In the near future detailed kinetic models will be evaluated at specific flame locations in an attempt to verify their application to diffusion flame systems. Specifically, can the models (given as inputs measured concentrations, temperature, and mass transport) predict net chemical fluxes which agree with our measured production rates? An analysis such as this will indicate possible shortcomings in both our knowledge of the chemical structure of these systems (i.e., radical concentrations are not well known) as well as deficiencies in proposed models for chemical growth.

REFERENCES:

1) J.D. Bittner, Ph. D. Dissertation, Massachusetts Institute of Technology, 1982.
2) M. Frenklach, D.W. Clary, W.C. Gardiner,Jr., and S.E. Stein, Twientieth Symp (Intnl) on Combustion. (The Combustion Institute, Pittsburgh, 1984). p. 887.
3) M. Frenklach, D.W. Clary, and M.K. Ramachandra, NASA Contractor Report 174880, May 1985.
4) K.C. Smyth, J.H. Miller, R.C. Dorfman, W.G. Mallard, and R.J. Santoro, Combust. Flame 62, 157 (1985).
5) K. Saito, A.S. Gordon, and F.A. Williams, ASME/AIChE National Heat Transfer Conference, 1985.
6) R.M. Fristrom and A.A. Westenberg, Flame Structure, (McGraw-Hill, New York, 1965).
7) S.M. Schoenung and R.K. Hanson, Comb. Sci. Tech. 24, 227 (1981).

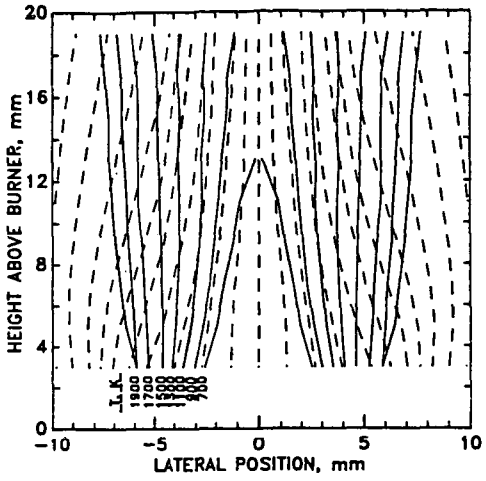

Figure 1: Isothermal contours (solid lines) calculated from uncorrected thermocouple measurements and streamlines (dashed lines) calculated from the velocity measurements for the methane/air flame.

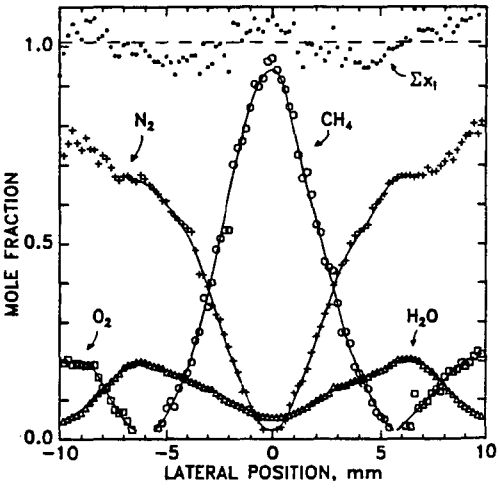

Figure 2: Mass spectrometric measurements of some of the major species. The N_2 profile has not been corrected for the small amount of CO detected at the same mass. At the top of the figure the sum of the mole fractions of all of the species present in the flame at a concentration of 1% or greater is shown. The dashed line represents the average value of 1.01 ± 0.04.

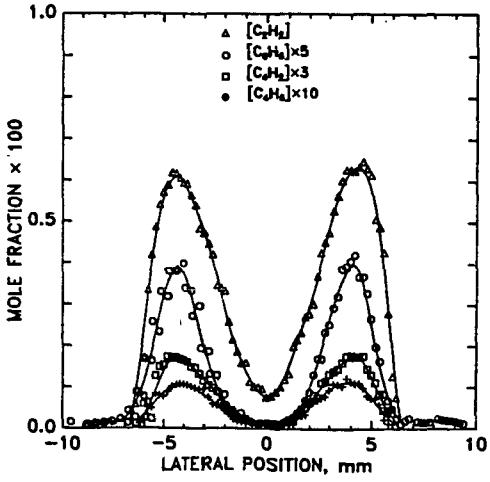

Figure 3: Mass spectrometric profile measurements of several minor species: acetylene, benzene, diacetylene, and butadiene at a height of 9mm above the burner.

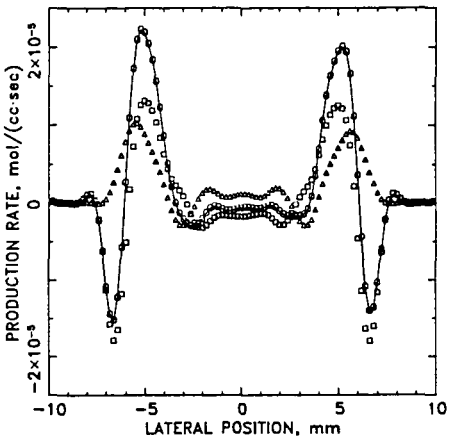

Figure 4: Contributions to the net chemical production rate (the connected circles) from diffusive (squares) and convective (triangles) terms in Eq. 1 at 9mm above the burner.

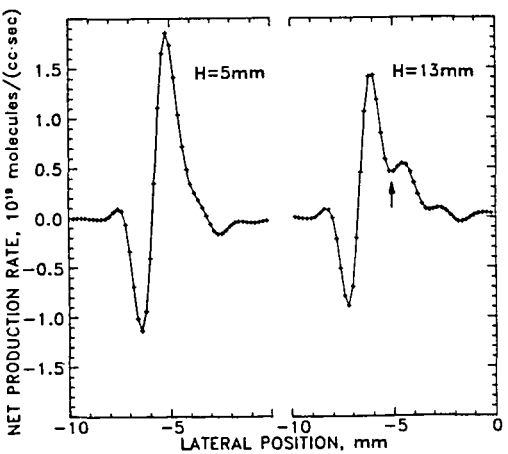

Figure 5: Profiles of the net chemical production rate for acetylene at two heights in the flame; only the left hand side of the flame is shown.

SULFUR TRIOXIDE FORMATION IN HIGH SULFUR RESIOUAL OIL FLAMES

Peter M. Walsh, Walter F. Farmayan,* Thomas Kolb,† Jånos M. Beér

Energy Laboratory and Oepartment of Chemical Engineering
Massachusetts Institute of Technology
Cambridge, MA 02139

INTRODUCTION

Heavy residual fuel oils usually contain between 1 and 4 wt% sulfur. Although SO_2 is the principal product of fuel sulfur oxidation, as much as 8 to 10 mol% of the sulfur oxides are present as SO_3 in the flue gas arriving at the cold end of the convective section in an electric utility boiler. Sulfur trioxide is quantitatively converted to sulfuric acid vapor in the presence of typical flue gas water vapor concentrations at temperatures below about 500 K (Halstead and Talbot, 1980). Condensation of sulfuric acid on surfaces at temperatures below the acid dewpoint is responsible for corrosion of cold end components, especially the air preheater. The accumulation of unburned carbon particles on the wet surfaces and reentrainment of their agglomerates is the source of acid smuts (Blum, Lees and Rendle, 1959; Conolly and Kelsell, 1982). The adsorption of sulfuric acid on ash and unburned carbon may make a significant contribution to the mass of stack gas particulates.

The most severe acid deposition and sulfate emissions problems are associated with catalytic oxidation of SO_2 to SO_3 over vanadium-containing deposits on tubes in the convective section. However, 1 to 2 mol% of the sulfur oxides are thought to be present as SO_3 in the furnace exit gas. Reidich and Reifenhäuser (1980) reported 2 mol% of the sulfur oxides as SO_3 (25 mol ppm of total gas) at the furnace exit in a 300 MW, tangentially fired boiler operated at 0.6 mol% excess O_2 with 2 wt% sulfur fuel. This is an amount sufficient to cause troublesome acid deposition and make a significant contribution to particulate loading, even in the absence of additional SO_3 formation in the convective section. Experience has shown that SO_3 formation can be controlled by reducing excess air, but this is accompanied by an increase in unburned carbon(coke cenospheres). Sulfur trioxide formation in the furnace is one component of a set of coupled processes making contributions to acid deposition and stack particulates (Cunningham and Jackson, 1978; Harada, Naito, Tsuchiya, and Nakajima, 1981).

Substantial progress has recently been made in the quantitative description of sulfur chemistry in flames(Muller, Schofield, Steinberg, and Broida, 1979; Kramlich, Malte, and Grosshandler, 1981; Smith, Wang, Tseregounis, and Westbrook, 1983; Wendt, Wootan, and Corley, 1983). Squires (1982) combined a detailed chemical kinetic description of reactions in the furnace with a global model for heterogeneous oxidation of SO_2 over tube deposits in the convective section. The predictions of this model were in good agreement with observed levels of SO_3 in the flue gases of 500 MW and 60 MW boilers. The present paper describes the initial steps of an investigation in which the results of fundamental kinetic studies are applied to the interpretation of direct measurements of SO_3 in boiler-type turbulent diffusion flames.

*Present address: Chemical Engineering Department, Shell Development Co., Westhollow Research Center, Houston, TX 77001

†Present address: Engler-Bunte-Institut, University of Karlsruhe, West Germany

Table 1. Experimental Conditions.

Run No.	Fuel Treatment	Atomizer Location w.r.t. Air Nozzle (mm)	Comb. Air Swirl No.	Mole Fraction O_2 in Flue Gas (%)	Excess Air (%)	Air Velocity at Nozzle (m/s)	Fuel Temperature (K)	Fuel Pressure (MPa)	Atomizing Air Pressure (MPa)
212	None	-25	0.9	1.5	7.3	49	389	1.48	1.48
213	Additive B	+25	0.9	1.5	7.3	49	389	1.51	1.51
214	None	+46	0.5	1.0	4.7	48	389	1.25	1.14
215	Additive D	+46	0.5	1.0	4.7	48	389	1.25	1.14
216	Additive E	+46	0.5	1.0	4.7	48	389	1.25	1.14
217	7.0% Water Emulsion	+46	0.5	1.0	4.7	48	391	1.25	1.14
218	Additive B	+46	0.5	1.0	4.7	48	389	1.25	1.14
219	Additive F	+46	0.5	1.0	4.7	48	389	1.25	1.14
220	Additive C	+46	0.5	1.0	4.7	48	389	1.25	1.14
		±0.5		±0.1			±3	±0.04	±0.04

EXPERIMENTAL

The measurements were made in the 1.2 x 1.2 m combustion tunnel in the MIT Combustion Research Facility (Beér, Jacques, Farmayan, and Taylor, 1981). The fuel was a mixture of residual oils produced by the Exxon refinery at Aruba. Its analysis was (wt%): carbon 85.80, hydrogen 10.86, nitrogen 0.47, sulfur 2.15, oxygen 0.57, and ash 0.10. Asphaltenes (IP 143/57) were 10.5 wt%, and the metal contents (wt ppm) were: vanadium 421, nickel 51, iron 15, sodium 9.8, calcium 20, and magnesium 4.8. The heating value was 42.5 MJ/kg and viscosity was 213 Saybolt Furol seconds at 50°C. The fuel was heated to 389 K, fired at 0.05 kg/s (2 MW thermal), and atomized by a 70° (full angle) six-hole "Y" jet nozzle with air as the atomizing medium. Combustion air was preheated to 560 K and supplied through a 0.176 m diameter duct to a 50° (full angle) divergent quarl mounted flush with one end wall of the combustion chamber. Several parameters were varied in order to examine their effects on carbon burnout and SO_3 formation: atomizer position, atomizing air/fuel ratio, combustion air swirl, and excess air. Five different commercial preparations designed to promote carbon burnout were added to the fuel; these contained compounds of the metals iron, zirconium, and cerium. One run was made with fuel emulsified with 7 wt% water. The experimental conditions are given in Table 1.

Gas temperature and composition (O_2, CO_2, CO, SO_2, NO) were determined using standard techniques. The axial component of the gas velocity was measured using a two-hole impact probe. A representative set of gas temperature, velocity, and composition profiles is shown in Fig. 1. Axial positions are measured from the exit of the 0.176 m diameter combustion air nozzle. For calculation purposes, the temperature, velocity, and carbon monoxide profiles in the region following the peak flame temperature at $z = z_o = 0.95$ m were fit by the following relations, shown as solid lines in Fig. 1:

$$T = T_o - \alpha(z-z_o) \qquad 1)$$

$$u = \beta/z \qquad 2)$$

$$X_{CO} = X_{CO,o} \exp[-\gamma(z-z_o)] \qquad 3)$$

Table 2. Data used in the calculations. The mole fractions of CO_2, O_2, and SO_2 are calculated flue gas values (wet) based on the fuel analysis and air/fuel ratio.

Run No.	T_o (K)	α (K/m)	β (m^2/s)	$X_{CO,o}$	γ (m^{-1})	X_{CO_2}	X_{O_2}	X_{SO_2} (ppm)
212	2005	175	16	.0133	1.517	.131	.0133	1220
213	2045	172	16	.0319	1.499	.131	.0133	1220
214	2000	138	15	.0435	1.992	.134	.00885	1250
215	2000	131	15	.0319	1.859	.134	.00885	1250
216	1975	130	15	.0291	1.829	.134	.00885	1250
217	1985	143	15	.0319	1.925	.133	.00878	1240
218	2005	133	15	.0368	1.906	.134	.00885	1250
219	2000	130	15	.0338	1.776	.134	.00885	1250
220	1990	133	15	.0338	1.776	.134	.00885	1250

Values of the parameters are given in Table 2. A mean gas residence time of 1 s, typical of a tightly designed oil-fired utility boiler, is reached at a distance of about 2.9 m from the combustion air nozzle.

SO_3 in the flame gases was determined using the Severn Science Ltd./Marchwood Engineering Laboratories(Central Electricity Generating Board, UK) continuously recording SO_3/H_2SO_4 monitor (Jackson, Hilton, and Buddery, 1981). This instrument is intended primarily as a flue or stack gas monitor. The 2 m long heated sampling probe supplied with the instrument was adapted for sampling in the flame by enclosing it in a water-cooled sheath. The glass sampling tube was replaced with one made of quartz. The indicated mole fractions of SO_3 along the flame axis are shown in Fig. 2.

After making a measurement, brown, orange, black, and yellow deposits were observed over 60 mm of the inside wall at the tip of the quartz sampling tube. Most of the deposit was soluble in 0.05 M H_2SO_4(aq). If this deposit contains vanadium it may catalyze the oxidation of SO_2 to SO_3. Even though the composition and physical properties of the probe deposit have not been determined, the available information can be used to place some approximate limits on the change in SO_3 content of the gas during sampling. Kinetic studies of related systems have been reviewed by Urbanek and Trela (1980), although most of this work has been conducted at relatively high SO_2 and O_2 (order of 10 mol%) and in the temperature range (650 to 850 K) over which conversion of SO_2 to SO_3 is greatest in flow reactors. The portion of the sampling tube coated with deposit was treated as a one-dimensional tubular reactor with catalytic wall. The wall temperature was assumed to decrease linearly from a value equal to the gas temperature at the probe tip to the melting point of V_2O_5 (943 K) at the end of the deposit. The sample enters the quartz tube at high temperature and with SO_3 at greater than equilibrium concentration. Conversion near the tube entrance was assumed to be controlled by boundary layer diffusion of SO_3 to and from the deposit surface, where SO_3 is in equilibrium with excess amounts of SO_2 and O_2. The composition of the bulk gas then shifts until it is equal to the equilibrium composition at the deposit. When the entering gas is at 1625 K and contains 10 mol ppm SO_3, 1250 mol ppm SO_2, and 1 mol% O_2, this occurs at a distance of 20 mm into the probe, at which point the mole fraction of SO_3 has decreased to 7 mol ppm. Production of SO_3 from this point onward is assumed to be kinetically controlled, with a rate proportional to the deposit geometric surface area. The mechanism of Mars and Maessen (1968) was used with activity per unit area estimated from the total areas and effectiveness factors reported by Livbjerg and Villadsen (1972). This calculation resulted in SO_3 equal to 27 mol ppm at a distance of 60 mm from the tube entrance. Therefore, in the event that the deposit has an activity comparable with that of an industrial alkali-promoted vanadium catalyst whose kinetic parameters are the same at 1400 K as at 800 K, SO_3 could be altered by the sampling procedure. Inspection of the SO_3 profiles shows that amounts of about 10 mol ppm were observed in 6 of the 9 runs under the conditions of the above calculation (z = 3 to 4 m). This indicates that the greatest errors would have occurred if SO_3 in the entering gas had actually been near equilibrium, with most of the observed SO_3 produced in the probe. Based on these observations the limits of error in the measurements are tentatively estimated to be plus 100% and minus 50% of the indicated values. Further study of this problem is warranted, not only by its importance to the sampling technique, but because the situation is analogous to that encountered in the convective section of a boiler, where vanadium and alkali metal tube deposits catalyze the oxidation of SO_2 as the flue gas is cooled.

CALCULATIONS

Notwithstanding the uncertainty in the accuracy of the SO_3 measurements, it is worthwhile to compare the observations with calculations based on a simple set of assumptions. The objective is to determine if SO_3 in the furnace exit gas of a

utility boiler might be correlated with flame characteristics which are known or can be estimated, such as fuel sulfur content, peak flame temperature, furnace exit gas temperature, excess air, and carbon monoxide.

A set of reactions which might account for the behavior of SO_3 in the present system is (Kramlich, Malte, and Grosshandler, 1981):

$$SO_2 + O + M \underset{k_{-1}}{\overset{k_1}{=}} SO_3 + M \qquad R1)$$

$$SO_3 + O \overset{k_2}{=} SO_2 + O_2 \qquad R2)$$

$$SO_3 + H = SO_2 + OH \qquad R3)$$

The rate coefficient for Reaction 1 is given by Troe (1978); that for Reaction 2 by Smith, Wang, Tseregounis, and Westbrook (1982). The reverse of Reaction 2 has a negligible rate under the conditions of interest here. Reaction 3 is neglected in the present calculation, although Kramlich et al. provide evidence that it is important in lean hydrocarbon combustion. The concentration of third bodies, M, is taken equal to the total gas concentration, C (but see Kramlich et al., 1981). The net rate of SO_3 production, apparently quite small over much of the region of the measurements, is then:

$$r_{SO_3} = k_1 C_{SO_2} C_O C - k_{-1} C_{SO_3} C - k_2 C_{SO_3} C_O \cong 0 \qquad 4)$$

$$\frac{C_{SO_3}}{C_{SO_2}} = \frac{X_{SO_3}}{X_{SO_2}} \cong \frac{k_1 C_O C}{k_{-1} C + k_2 C_O} \qquad 5)$$

Under the above assumptions the ratio of SO_3 to SO_2 is limited to the range

$$K_1 C_{O,eq} \leqslant \frac{X_{SO_3}}{X_{SO_2}} \leqslant \frac{k_1}{k_2} C \qquad 6)$$

as long as the system is not frozen. The total equilibrium mole fractions of SO_3, shown as dashed lines in Fig. 2, are everywhere less than the measured values, which are, in turn, much less than the right hand side of Equation 6, especially near the furnace exit. In order to apply Equation 5 we require an estimate of the oxygen atom concentration. In discussing this same problem Merryman and Levy (1979) suggested that an estimate of the oxygen atom concentration might be obtained by assuming equilibration of the principal reactions by which they are formed during CO oxidation:

$$\begin{aligned} CO + OH &= CO_2 + H \\ H + O_2 &= OH + O \\ \hline CO + O_2 &= CO_2 + O \end{aligned} \qquad R4)$$

$$C_O = \frac{K_4 C_{CO} C_{O_2}}{C_{CO_2}} \qquad 7)$$

The mole fractions of O_2, CO_2, and SO_2 were taken constant and equal to the outlet values, given in Table 2. Sulfur trioxide mole fractions calculated using Equations 1, 3, 5, and 7 are shown as solid lines in Fig. 2.

The calculated profiles satisfactorily reproduce the magnitude of the SO_3 measurements near a mean residence time of 1 s (z = 2.9 m) in most of the lower excess O_2 (1 mol%) cases. Large discrepancies are observed in two instances (Runs 212 and 213); these are distinguished by low temperature (212), high levels of CO (213), and high excess O_2 (both). The calculated values are especially sensitive to temperature. Most important is the fact that the calculation predicts SO_3 increasing with distance near the furnace outlet, while most of the measurements show a tendency of SO_3 to approach equilibrium. The assumption of equilibration of Reaction 4 was not originally intended by Merryman and Levy (1979) to be applied at points so far into the postflame region, but at shorter times. As the rate of CO oxidation slows, due to CO consumption and decreasing temperature, Equation 7 becomes a progressively poorer approximation. The CO mole fractions at z = 3.1 m are in the range 320 to 950 ppm, no longer sufficient to maintain significant super-equilibrium concentration of oxygen atoms against competition with recombination, for example, by Reactions 1 and 2 themselves. Because the calculation is least reliable near the furnace exit, it would be unwise to use this approximation to estimate SO_3 in furnace exit gas. The steady state approach (Equation 5) might still be useful however, if the decay of oxygen atoms at long times can be related to CO and stable species concentrations.

SUMMARY

Mole fractions of sulfur trioxide were measured along the axis of a confined turbulent diffusion flame, under conditions simulating those in electric utility boilers. The fuel was a No. 6 residual oil containing 2.2 wt% sulfur, fired at the rate of 0.05 kg/s or 2 MW(thermal). The sulfur trioxide mole fractions were in the range from 3 to 25 mol ppm; representing 0.2 to 2% of the total sulfur. An estimate was made of the contribution of catalytic SO_3 formation by ash constituents deposited in the probe. The uncertainty introduced from this source was estimated to be plus 100% and minus 50% of the indicated value. The observed mole fractions were approximately steady and everywhere greater than the local total equilibrium values. Sulfur trioxide mole fractions were calculated by assuming that the steady state is determined by atomic oxygen reactions, with atomic oxygen in partial equilibrium with carbon monoxide, carbon dioxide, and molecular oxygen. The results of this calculation approximately reproduced the experimental measurements under most, but not all, sets of conditions investigated. Because of its sensitivity to temperature, carbon monoxide, and oxygen this approximation is not recommended for the estimation of SO_3 in furnace exit gases.

ACKNOWLEDGEMENTS

We thank Bonnie Caputo of the MIT Energy Laboratory for the layout and typing of the drafts and final manuscript. This work is supported by Babcock and Wilcox Canada, Canadian Electrical Association, Electric Power Research Institute, Empire State Electric Energy Research Corp., Florida Power and Light Co., Northeast Utilities Service Co., and Shell Development Co.

NOMENCLATURE

C	total gas concentration, kmol/m^3
C_i	concentration of gaseous species i, kmol/m^3
k_j	rate coefficient of Reaction j in forward direction, various units
k_{-j}	rate coefficient of Reaction j in reverse direction, various units
K_j	equilibrium constant for reaction j, = k_j/k_{-j}
r_i	net rate of production of species i by chemical reaction, kmol/m^{3}s
Sw	combustion air Swirl Number
T	temperature, K
u	axial component of gas velocity, m/s
X_i	mole fraction of species i
z	axial distance from the combustion air nozzle, m
α	mean temperature gradient along the flame axis, Equation 1, K/m
β	gas velocity decay constant, Equation 2, m^2/s
γ	carbon monoxide decay constant, Equation 3, m^{-1}

Subscripts

o	evaluated at $z = z_o$ = 0.95 m from the combustion air nozzle
eq	total equilibrium concentration

REFERENCES

J.M. Beér, M.T. Jacques, W. Farmayan, and B.R. Taylor, Eighteenth Symposium (International) on Combustion, The Combustion Institute, Pittsburgh, PA, 1981, p. 101.

H.A. Blum, B. Lees, and L.K. Rendle, J. Inst. Fuel 32(1959)165.

R. Conolly and P.H. Kelsell, J. Inst. Energy 55(1982)47.

A.T.S. Cunningham and P.J. Jackson, J. Inst. Fuel 51(1978)20.

W.D. Halstead and J.R.W. Talbot, J. Inst. Energy 53(1980)142.

Y. Harada, S. Naito, T. Tsuchiya, and Y. Nakajima, Problems of Low Grade Oil Firing Boilers and their Solutions, Mitsubishi Technical Review 18(1981)85.

P.J. Jackson, O.A. Hilton, and J.H. Buddery, J. Inst. Energy 54(1981)124.

J.C. Kramlich, P.C. Malte, and W.L. Grosshandler, Eighteenth Symposium (International) on Combustion, The Combustion Institute, Pittsburgh, PA, 1981, p. 151.

H. Livbjerg and J. Villadsen, Chem. Eng. Sci. 27(1972)21.

E.L. Merryman and A. Levy, Seventeenth Symposium (International) on Combustion, The Combustion Institute, Pittsburgh PA, 1979, p. 727.

P. Mars and J.G.H. Maessen, J. Catal. 10(1968)1.

C.H. Muller III, K. Schofield, M. Steinberg, and H.P. Broida, Seventeenth Symposium (International) on Combustion, The Combustion Institute, Pittsburgh, PA, 1979, p. 867.

H. Reidick and R. Reifenhäuser, Combustion, Feb. 1980, p. 17.

O.I. Smith, S.-N. Wang, S. Tseregounis, and C.K. Westbrook, Combustion Science and Technology 30(1983)241.

R.T. Squires, J. Inst. Energy 55(1982)41.

J. Troe, Ann. Rev. Phys. Chem. 29(1978)223.

A. Urbanek and M. Trela, Catal. Rev. Sci. Eng. 21(1980)73.

J.O.L Wendt, E.C. Wootan, and T.L. Corley, Combustion and Flame 49(1983)261.

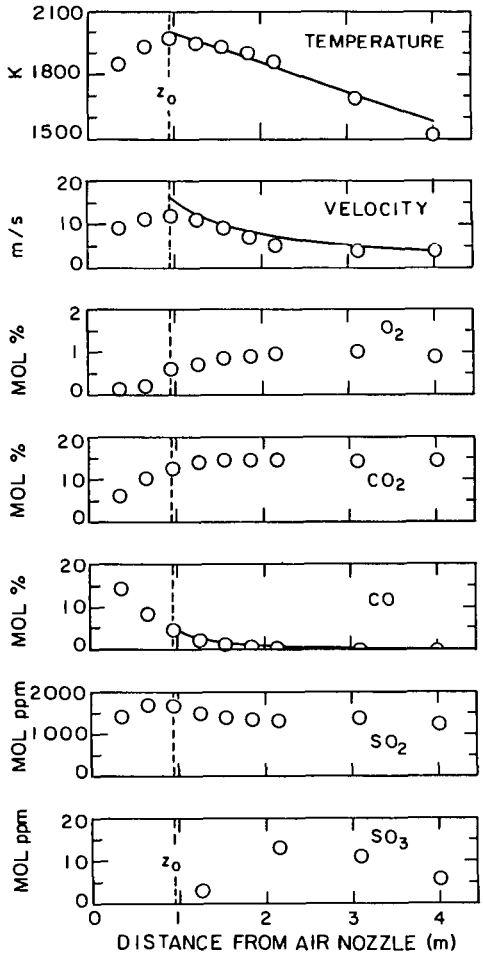

Figure 1. Measurements of gas temperature, axial component of gas velocity, and mole fractions (dry basis) of O_2, CO_2, CO, SO_2, and SO_3 along the axis of a 2 MW residual oil spray flame. Run No. 214, combustion air Swirl No. = 0.5. The location of the peak flame temperature, z_o = 0.95 m, is taken as the starting point for calculations. Solid lines are fits of Equations 1, 2, and 3 to the data points.

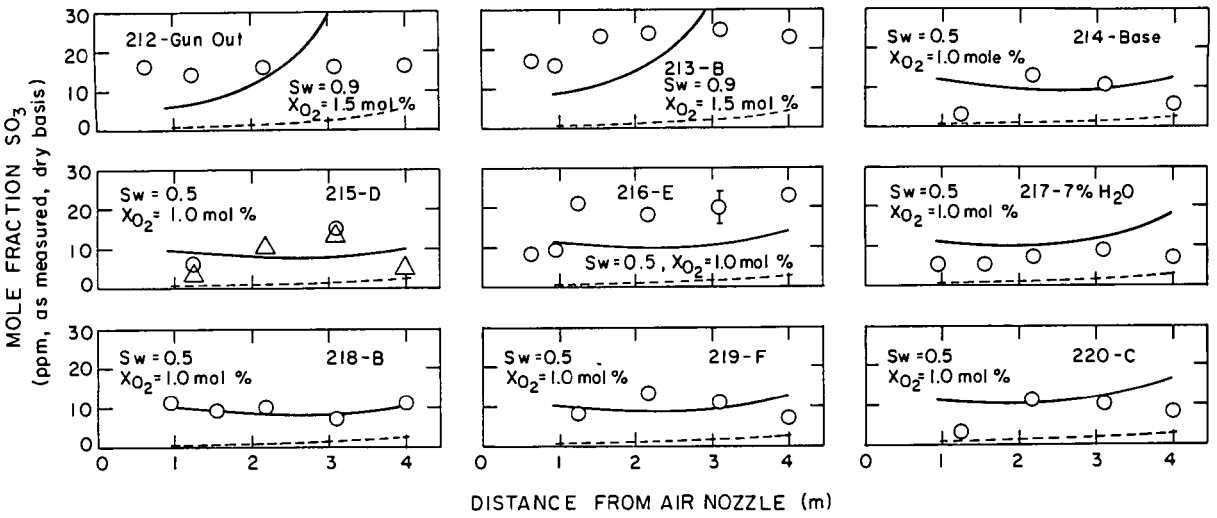

Figure 2. Mole fractions (dry basis) of SO_3 measured along the flame axis and comparison with calculations. The combustion air Swirl No. and flue gas O_2 mole fraction (dry) are indicated in each figure. A distinguishing feature of each run is indicated after the run number. The letters B to F correspond to various fuel additives designed to promote carbon burnout.

Circles: measured value
Triangles: duplicate measurements in separate trial
Dashed line: calculated, total equilibrium
Solid line: calculated, steady state, with oxygen atoms in partial equilibrium with CO, CO_2, and O_2.

RAMAN STUDIES OF HALON FIRE RETARDANTS.

J. H. May, F. S. Allen, M. R. Ondrias, R. E. Tapscott,
H. D. Beeson, and D. M. Zallen.

Chemistry Department, and New Mexico Engineering Research Institute,
University of New Mexico, Albuquerque, New Mexico 87131.

Raman spectroscopy can be used as a passive probe for the study of active systems. Various types of analytical determinations can be made with-out perturbing the system under study. Of interest is the elucidation of the extinction processes employed by Halon type extinguishing agents. Raman has in the past been used to study molecules such as H_2O, N_2, and CO_2 in flames (1). Halons and pyrolyzed products, having vibrations that are more polarization sensitive than the above molecules, should then be readily analyzed in flames. As an initial approach to this problem we are studying the pyrolysis of Halon 2402 (1,2 dibromotetrafluoroethane). The pyrolysis products are isolated using vacuum line techniques, and identified using GC/MS and Raman. A library of the Raman spectra from each component is being formed for subsequent use in flame analysis.

Experimentally, we use a tube furnace with a specially designed tube, having detachable nitrogen traps on each end, and also capable of holding a vacuum. To simulate the combustion process, Halon 2402 is frozen in one of the nitrogen traps, and the whole system is brought to high vacuum. The Halon is then allowed to vacuum transfer through the pyrolysis tube, which is at approximately 790°C, to the other nitrogen trap. This process is repeated several times. The products are then vacuum distilled, capturing fractions as they come over, in different, sealable cuvettes. Presently all fractions are studied in the gas phase at room temperature.

The Raman data are collected on an instument made up of:

1) An EG&G Princeton Applied Research model 1420 intensified silicon photodiode array tube coupled with its model 1218 solid state detector controller, and the model 1215 computer console.

2) A SPEX model 1877 triplemate monochromater.

3) A Coherent model CR-4 Argon ion laser, capable of producing over 3 watts of continuous wave power at the 488.0 nm. line.

Spectra, in the range of 100 cm(-1) to 1000 cm(-1) can be obtained at a single setting of the monochromater. Since Raman spectra of many of the thermal degradation products are not available, we have used a Finnigan, series 4900, GC/MS to identify the products that are obtained from the pyrolysis experiment. Raman spectra collected on these components will subsequently form a spectral library of the pyrolysis products.

Figures 1. and 2. are the Raman spectra of the first fraction collected from the vacuum distillation process on the pyrolyzed 2402. The complexity of the spectra suggests that more than one component is present. The GC/MS revealed that the gas contained only tetrafluoroethylene, and bromotrifluoromethane (Halon 1301) in significant concentrations. Figures 3. and 4. are the Raman spectra of pure 1301, and it is evident that its spectral bands match many of the bands in the distilled fraction.

Pure tetrafluoroethylene will be examined to identify its spectral contribution to pyrolysis products spectra. The vacuum distillation was done at 500 millitorr, later distillations using higher pressures should provide better separation of the fractions.

Each of these spectra took thirty minutes to collect, fifteen minutes for the signal spectra, and another fifteen for the background (Raman spectra normally require the subtraction of the background spectra, taken with the exitation source off, from the signal spectra. This is especially true for photodiode array detectors.). Accurate spectra, to within 2 cm(-1), of all but the weaker bands can be taken in a minute or less if desired (This includes background spectra.). Using pulsed, or higher intensity C.W. lasers, spectra could be taken in less time with even better signal to noise ratios.

As a result of these preliminary studies, we will build a library of Raman spectra for the stable products produced by the simulated combustion of the Halon 2402 in a vacuum, as well as in oxidizing and reducing environments. This library will then be used in subsequent studies to identify which of the products are present in flames near extinction due to the presence of Halon 2402.

REFERENCE.

1. Lapp, M. and Penny, C. M. . Laser Raman Gas Diagnostics. Plenum Press, New York and London. 1974.

ACKNOWLEDGMENTS: Partial support for this project provided by the Air Force Engineering Services Center, Tyndall A.F.B., Fl. We would like also to acknowledge Mr. Joseph L. Walker for fruitful discussions.

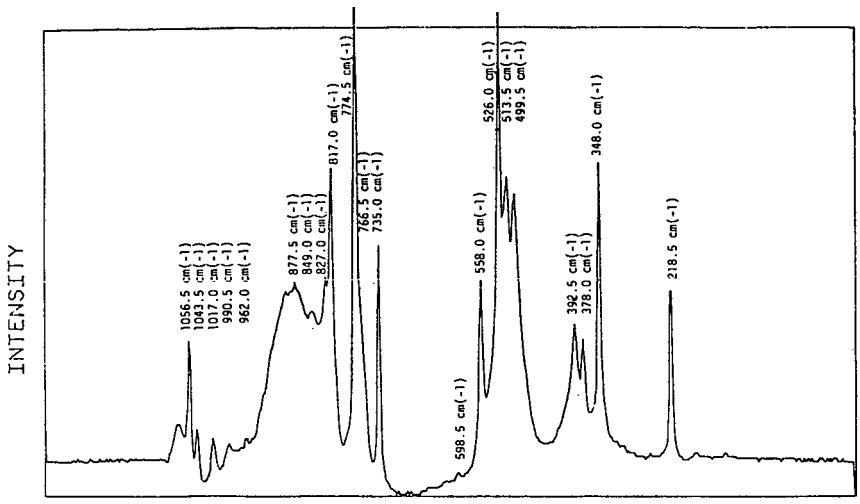

Figure 1. Raman spectrum of the first fraction collected from the vacuum distillation process, for the products of the pyrolyzed Halon 2402.

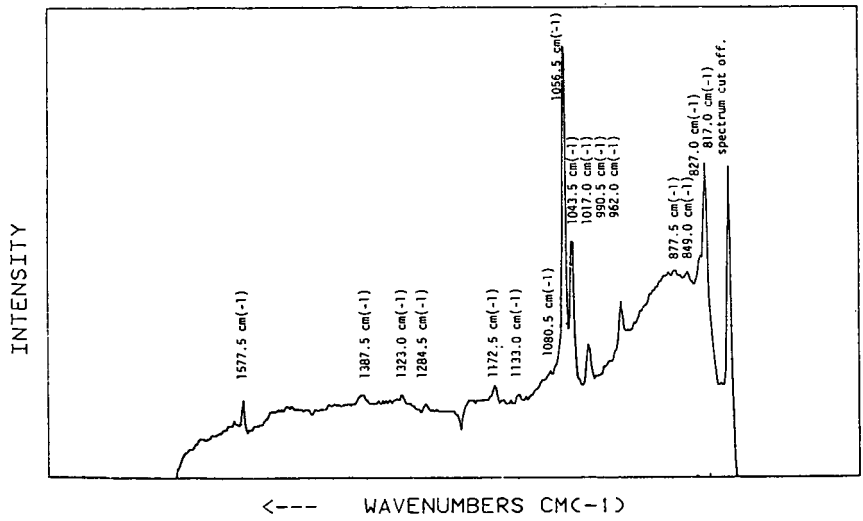

Figure 2. Raman spectum of the first fraction collected from the vacuum distillation process, for the products of the pyrolyzed Halon 2402. Y axis has been expanded.

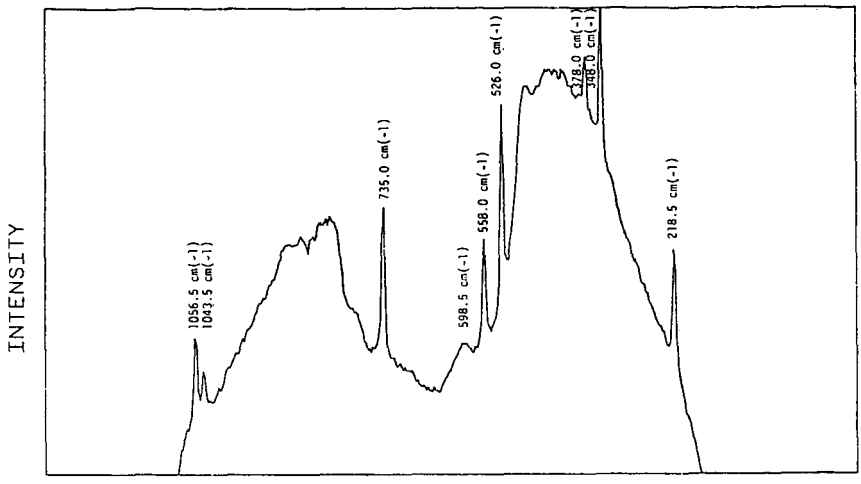

Figure 3. Raman spectrum of pure Halon 1301 (Bromotetrafluoromethane).

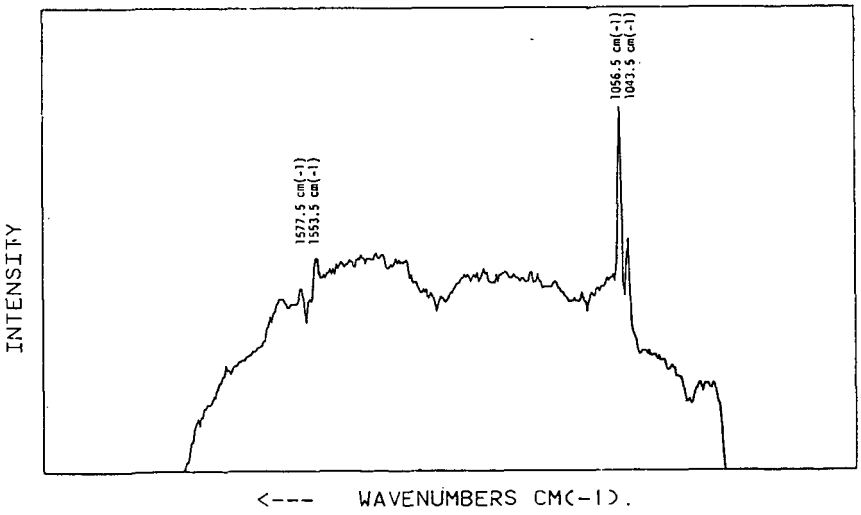

Figure 4. Raman spectrum of pure Halon 1301 (Bromotetrafluoromethane).
Y axis has been expanded.